Electronic Structure of Nitride-based Quantum Dots

vorgelegt von

Momme Winkelnkemper

aus Münster

Von der Fakultät II - Mathematik und Naturwissenschaften
der Technischen Universität Berlin
zur Erlangung des akademischen Grades
Doktor der Naturwissenschaften
- Dr. rer. nat. -

genehmigte Dissertation

Promotionsausschuss:

Vorsitzender:	Prof. Dr. A. Knorr
Berichter/Gutachter:	Prof. Dr. D. Bimberg
Berichter/Gutachter:	Priv.-Doz. Dr. A. Hoffmann

Tag der wissenschaftlichen Aussprache: 07.11.2008

Berlin 2008

D 83

Abstract

The group-III nitrides, InN, GaN, AlN, and their alloys have emerged to one of the most important material classes for opto-electronic devices. The incorporation of quantum dots (QDs) as active material improves the performance of conventional opto-electronic devices, such as light-emitting diodes and laser diodes. Moreover, entirely new devices, such as single-photon emitters and emitters of entangled photon pairs, have already been realized using single QDs as active medium.

In the present work the electronic and optical properties of $\mathrm{In_xGa_{1\text{-}x}N}$/GaN and GaN/AlN QDs are studied by means of eight-band $\mathbf{k}\cdot\mathbf{p}$ theory. Experimental results obtained by (time-resolved) photoluminescence and cathodoluminescence spectroscopy on $\mathrm{In_xGa_{1\text{-}x}N}$/GaN QDs are interpreted in detail using the theoretical results. The $\mathbf{k}\cdot\mathbf{p}$ model for the QD electronic-structure calculations accounts for strain, piezo- and pyroelectric effects, spin-orbit and crystal-field splitting, and is implemented for arbitrarily shaped QDs on a finite differences grid. Few-particle corrections are included using the self-consistent Hartree method. Band parameters for the wurtzite and zinc-blende phases of GaN, AlN, and InN are derived from first-principle G_0W_0 band-structure calculations. The parameters agree well with available experimental data. Reliable values are also provided for parameters that have not been determined experimentally yet.

The electronic properties of nitride QDs are dominated by the large built-in piezo- and pyroelectric fields, which lead to a pronounced red-shift of excitonic transition energies and extremely long radiative lifetimes in large GaN/AlN QDs. In $\mathrm{In_xGa_{1\text{-}x}N}$/GaN QDs these fields induce a pronounced dependence of the radiative excitonic lifetimes on the exact QD shape and composition. It is demonstrated that the resulting variations of the radiative lifetimes in an inhomogeneous QD ensemble are the origin of the multi-exponential luminescence decay frequently observed in time-resolved ensemble measurements on $\mathrm{In_xGa_{1\text{-}x}N}$/GaN QDs.

A polarization mechanism in nitride QDs based on strain-induced valence-band mixing effects is discovered, that can, in the future, be exploited for the fabrication of QD-based sources of single polarized photons. Due to the valence-band structure of wurtzite group-III nitrides and the specific strain situation in c-plane QDs, the confined hole states are formed predominantly by the two highest valence bands. In particular, the hole ground state ($h_0 \equiv h_A$) is formed by the A band, and the first excited hole state ($h_1 \equiv h_B$) by the B band. It is shown that the interband transitions involving h_A or h_B are affected differently by an anisotropic strain field in the basal plane: h_A transitions are linearly polarized parallel to the direction of weakest compression; transitions involving h_B perpendicular to it. Based on this effect, experimentally observed spectra of single $\mathrm{In_xGa_{1\text{-}x}N}$/GaN QDs are explained. These spectra contain up to five narrow lines, which are linearly polarized in orthogonal directions. For GaN/AlN QDs spectroscopic properties, such as excitonic transition energies, radiative lifetimes, and binding energies of few-particle complexes are correlated to structural properties of the QDs. It is demonstrated how the polarization mechanism discovered for $\mathrm{In_xGa_{1\text{-}x}N}$/GaN QDs can be exploited and manipulated to achieve a well-defined linear polarization in devices based on GaN/AlN QDs for, e.g., future quantum-key distribution and back lighting of liquid-crystal displays.

Zusammenfassung

Die Gruppe-III-Nitride InN, GaN, AlN und ihre Legierungen haben sich zu einem der wichtigsten Materialsysteme für opto-elektronische Bauelemente entwickelt. Die Verwendung von Quantenpunkten (QPen) als aktives Material verspricht zudem eine deutliche Verbesserung der Eigenschaften von konventionellen opto-elektronischen Bauelementen wie Leucht- und Laserdioden. Darüber hinaus wurden bereits völlig neuartige Bauelemente, wie Einzelphotonenemitter und Emitter von verschränkten Photonenpaaren, unter Verwendung von QPen als aktives Medium realisiert.

In der vorliegenden Arbeit werden die elektronischen und optischen Eigenschaften von $\mathrm{In_xGa_{1\text{-}x}N}$/GaN und GaN/AlN QPen mit Hilfe von acht-band $\mathbf{k}\cdot\mathbf{p}$-Theorie untersucht. Anhand der theoretischen Ergebnisse werden experimentelle Ergebnisse aus (zeitaufgelöster) Photolumineszenz- und Kathodolumineszenzspektroskopie an $\mathrm{In_xGa_{1\text{-}x}N}$/GaN QPen im Detail interpretiert. Das $\mathbf{K}\cdot\mathbf{p}$-Model für die Berechnung der elektronischen Struktur von Quantenpunkten (QPen) berücksichtigt die Effekte von Verspannung, piezo- und pyroelektrischer Polarisation, Spin-Bahn- und Kristallfeld-Aufspaltung und ist für Quantenpunkte mit beliebiger Form auf einem Finite-Differenzen-Gitter implementiert. Mehrteilchen-Korrekturen werden im Rahmen der selbst-konsistenten Hartree-Methode einbezogen. Bandstrukturparameter für die Wurtzit- und Zinkblendephasen von GaN, AlN und InN werden von ab-initio Bandstrukturrechnungen in der G_0W_0 Näherung abgeleitet. Die Parameter stimmen sehr gut mit allen verfügbaren experimentellen Werten überein. Verlässliche Werte werden auch für solche Parameter bereit gestellt, die bisher noch nicht experimentell bestimmt wurden.

Die elektronischen Eigenschaften von Nitrid-Quantenpunkten werden von den starken internen piezo- und pyroelektrischen Feldern dominiert, die in großen GaN/AlN QPen zu einer deutlichen Rotverschiebung der exzitonischen Übergangsenergien und extrem langen strahlenden Lebensdauern führen. In $\mathrm{In_xGa_{1\text{-}x}N}$/GaN QPen führen die Felder zu einer ausgeprägten Abhängigkeit der strahlenden exzitonischen Lebensdauern von der exakten Form und Komposition der QPe. Es wird gezeigt, dass die hieraus resultierende Variation der strahlenden Lebensdauern in einem inhomogenen QP-Ensemble die Ursache des multi-exponentiellen Lumineszenz-Abklingens ist, das häufig in zeitaufgelösten Ensemble-Messungen an $\mathrm{In_xGa_{1\text{-}x}N}$/GaN QPen beobachtet wird.

Ein Polarisationsmechanismus in Nitrid-QPen basierend auf verspannungsinduzierten Valenzband-Mischeffekten wurde entdeckt, der zukünftig für die Herstellung von QP-basierten Quellen von einzelnen polarisierten Photonen ausgenutzt werden kann. Verursacht durch die Valenzbandstruktur von Gruppe-III-Nitriden mit Wurtzitstruktur und das Verspannungsfeld in QPen auf der *c*-Oberfläche, werden die lokalisierten Lochzustände vornehmlich durch die zwei höchsten Valenzbänder gebildet. Insbesondere wird der Loch-Grundzustand ($h_0 \equiv h_A$) vom *A*-Band geformt und der erste angeregte Lochzustand ($h_1 \equiv h_B$) vom *B*-Band. Es wird gezeigt, dass die Interband-Übergänge unter Beteiligung von h_A oder h_B unterschiedlich von einem anisotropen Verspannungsfeld in der Basalebene beeinträchtigt werden: h_A-Übergänge zeigen lineare Polarisation parallel zur Achse der schwächsten Kompression; h_B-Übergänge senkrecht dazu. Anhand dieses Effektes werden experimentell beobachtete Spektren von einzelnen $\mathrm{In_xGa_{1\text{-}x}N}$/GaN QPen erklärt, welche bis zu fünf scharfe Linien zeigen, die linear in orthogonale Richtungen polarisiert sind. Die spektroskopischen Eigenschaften von GaN/AlN QPen, wie Exzitonen-Übergangsenergie, strahlende Lebensdauern und Mehrteilchen-Bindungsenergien, werden mit den strukturellen Eigenschaften der QPe korreliert. Es wird gezeigt wie der an $\mathrm{In_xGa_{1\text{-}x}N}$/GaN QPen entdeckte Polarisationsmechanismus ausgenutzt und manipuliert werden kann um eine wohldefinierte lineare Polarisation in GaN/AlN-QPen-basierten Bauelementen mit Anwendung in, z.B., zukünftiger Quantenkryptographie oder als Hintergrundbeleuchtung von Flüssigkristall-Displays.

Parts of this thesis have been published before in the following articles in scientific journals:

M. Winkelnkemper, M. Dworzak, T. Bartel, A. Strittmatter, A. Hoffmann, and D. Bimberg: “Origin of the Broad Lifetime Distribution of Localized Excitons in InGaN/GaN Quantum Dots”, *Physica Status Solidi (b)* 245, 2766 (2008)

M. Winkelnkemper, R. Seguin, S. Rodt, A. Hoffmann, and D. Bimberg: “GaN/AlN Quantum Dots for Single Qubit Emitters”, *IOP Journal of Physics: Condensed Matter* 20, 454211 (2008)

P. Rinke, M. Winkelnkemper, A. Qteish, D. Bimberg, J. Neugebauer, and M. Scheffler: “Consistent Set of Band Parameters for the Group-III Nitrides AlN, GaN, and InN”, *Physical Review B* 77, 075202 (2008)

M. Winkelnkemper, R. Seguin, S. Rodt, A. Schliwa, L. Reissmann, A. Strittmatter, A. Hoffmann, and D. Bimberg: “Polarized Emission Lines from Single InGaN/GaN Quantum Dots: Role of the Valence Band Structure of Wurtzite Group-III Nitrides”, *Physica E* 40, 2217 (2008)

M. Winkelnkemper, R. Seguin, S. Rodt, A. Schliwa, L. Reissmann, A. Strittmatter, A. Hoffmann, and D. Bimberg: “Polarized Emission Lines from A- and B-type Excitonic Complexes in Single InGaN/GaN Quantum Dots”, *Journal of Applied Physics* 101, 113708 (2007)

M. Winkelnkemper, A. Schliwa, and D. Bimberg: “Interrelation of Structural and Electronic Properties in $In_xGa_{1-x}N$/GaN Quantum Dots Using an Eight-band $\mathbf{k}\cdot\mathbf{p}$-model”, *Physical Review B* 74, 155322 (2006)

P. Rinke, M. Scheffler, A. Qteish, M. Winkelnkemper, D. Bimberg, and J. Neugebauer: “Band Gap and Band Parameters of InN and GaN from Quasiparticle Energy Calculations Based on Exact-exchange Density-functional Theory”, *Applied Physics Letters* 89, 161919 (2006)

Contents

1 Introduction **11**
1.1 About this Work . . . 12
1.2 Thesis Structure . . . 13

2 Fundamentals **15**
2.1 Three-dimensional Confinement in Self-assembled Quantum Dots . . . 15
2.2 Nitride-based Quantum Dots . . . 17
2.3 Polarization Fields in Group-III Nitride Heterostructures . . . 18

3 The $\mathbf{k}\cdot\mathbf{p}$ Method for Strained Semiconductor Nanostructures **23**
3.1 Strain Field . . . 24
3.2 Built-in Electric Fields: Piezo- and Pyroelectric Potentials . . . 25
3.3 The $\mathbf{K}\cdot\mathbf{p}$-Hamiltonian . . . 26
3.4 Excitonic Corrections: Self-consistent Hartree-method . . . 30
3.5 Transition Probabilities and Radiative Lifetimes . . . 31

4 Material Parameters for Group-III Nitrides **33**
4.1 Band Dispersion Parameters Derived from G_0W_0 Calculations . . . 34
  4.1.1 Comparison to Experimental Values . . . 36
  4.1.2 Comparison to the Parameters Recommended by Vurgaftman and Meyer 40
4.2 Summary . . . 41

5 Valence-band Structure of Strained Group-III Nitrides **43**
5.1 Group-III Nitrides under Biaxial Strain . . . 43
5.2 Anisotropic Strain in the Basal Plane . . . 45
5.3 Summary . . . 47

6 InGaN/GaN Quantum Dots **49**
6.1 Model Quantum Dots . . . 49
6.2 Electronic Structure of InGaN Quantum Dots . . . 53
  6.2.1 Built-in Electric Fields . . . 53
  6.2.2 Local Band-edge Profile . . . 54
  6.2.3 Bound Single-particle States . . . 56

6.3 Exciton Transition Energies 59
6.4 Radiative Lifetimes of Confined Excitons 61
  6.4.1 Experimental Results 61
  6.4.2 Distribution of Excitonic Lifetimes 63
  6.4.3 Quantum Dot Structure and Radiative Lifetimes 65
6.5 Polarized Emission Lines: *A*- and *B*-type transitions 69
  6.5.1 Experimental Results 70
  6.5.2 *A*- and *B*-band Hole States 71
  6.5.3 *A*- and *B*-type Transitions of Excitonic Complexes 75
6.6 Summary 77

7 GaN/AlN Quantum Dots 79
7.1 Model Structure 79
7.2 Exciton Transition Energies and Radiative Lifetimes 80
7.3 Binding Energies of Few-particle Complexes 81
7.4 Single-particle Energy Levels 84
  7.4.1 Optical Transitions 85
  7.4.2 Control of the Polarization by Uniaxial Stress 87
7.5 Summary 88

8 Conclusion 91
8.1 Outlook 93

Acknowledgement 95

Appendices

A Material Parameters for the K·p Calculations 97

B K·p Method for Zinc-blende Crystals 101

C Effective Masses and Luttinger(-like) Parameters 103

Abbreviations 105

Bibliography 107

1 Introduction

Semiconductor nanostructures are essential building blocks for modern opto-electronic devices, such as light-emitting diodes (LEDs) and laser diodes (LDs). Quantum wells or quantum dots (QDs) in the active regions of these devices convert electric current to light with high efficiency. Different material systems have to be used for the active regions in order to realize the target wavelengths of numerous applications in, e.g., entertainment technologies, telecommunication, and medical engineering.

The group-III nitrides AlN, GaN, and InN and their alloys have become an important and versatile class of semiconductor materials, in particular for opto-electronics. Nitride-based semiconductor nanostructures have been widely studied in the last decade and revolutionary devices have emerged from this effort. Current applications in solid state lighting (LEDs and LDs) range from the visible spectrum[1–4]—including white light emitters with the aid of phosphors[5–7]—to the deep ultra-violet.[8;9] Already at early stages of research the enormous quantum-efficiency of $\mathrm{In_xGa_{1\text{-}x}N}$-based opto-electronic devices has been attributed to QD properties of localization centers inside the $\mathrm{In_xGa_{1\text{-}x}N}$ layer(s).[10–13] In addition to well-established benefits of QDs, like high temperature stability and low threshold currents in LDs,[14–16] $\mathrm{In_xGa_{1\text{-}x}N}$ QDs have the advantage over $\mathrm{In_xGa_{1\text{-}x}N}$ quantum wells that the quantum-confined Stark effect and the corresponding blue shift of the emission at high charge-carrier densities is not observed.[17]

In recent years a new challenging field of application for semiconductor QDs, beyond LDs and LEDs, has emerged. The rapidly developing fields of quantum communication and quantum computing give rise to the demand for electrically triggered sources of single photons. Devices based on self-assembled QDs are promising candidates for reliable low-cost solutions in this matter. Quantum dots can be easily integrated into diode structures for electrical triggering and entire devices can be fabricated using well-established technologies. Moreover, the emission from single QDs is intrinsically single-photon emission in contrast to, e.g., the use of attenuated laser pulses, where single-photon pulses are achieved by exploiting statistical effects at very low intensities. Electrically triggered single-photon emitters with extraordinary spectral purity have been realized recently using InAs/GaAs QDs.[18;19] For application in quantum cryptography and computing emission with controlled linear polarization is favorable. This is achieved for InAs/GaAs QDs at low temperatures by exploiting the fine-structure splitting of the exciton, which splits the excitonic ground-state emission into an orthogonally polarized line pair. However, this splitting of up to 500 μeV for large QDs,[20] is smaller than the homogeneous line width of the emission lines at elevated temperatures, inhibiting a spectral separation of the cross-polarized line pair. Devices based on nitride QDs present important alternatives for single-photon emission, because they have the potential to be operable even at elevated temperatures.[21] In μ-photoluminescence (PL) and cathodoluminescence (CL) spectroscopy narrow emission lines from single $In_xGa_{1\text{-}x}N$/GaN[22–29] and GaN/AlN QDs grown on the *c*-plane[21;30–33] and *a*-plane[34] have been observed. Also zinc-blende GaN/AlN QDs are investigated presently.[35;36] Optically pumped single-photon emission from single GaN/AlN QDs at temperatures as high as 200 K has already been demonstrated.[21] In the future the spectral range of nitride QDs can be extended to the long-wavelength range for fibre-optical communication employing InN/GaN.[37]

1.1 About this Work

Despite the tremendous advances described above, the understanding of the opto-electronic properties of nitride QDs still needs to be fundamentally improved in order to further advance devices based on nitride QDs. This work contributes to this research field with theoretical investigations of $In_xGa_{1\text{-}x}N$/GaN and GaN/AlN QDs within the framework of eight-band $\mathbf{k}\cdot\mathbf{p}$ theory.

First, a consistent set of $\mathbf{k}\cdot\mathbf{p}$ parameters for the zinc-blende and wurtzite phases of InN, GaN, and AlN is derived from first-principle G_0W_0 band-structure calculations. It will be demonstrated that the parameter set is in very good agreement with available experimental data and, therefore, provides reliable predictions for parameters that have not been determined experimentally, yet.

Thereafter, the electronic and optical properties of $In_xGa_{1\text{-}x}N$/GaN and GaN/AlN QDs, such as excitonic transitions energies, radiative lifetimes, and binding energies of few-particle complexes, are calculated. Spectroscopic properties are related to structural properties, such as size, shape, and composition. It is shown that the electronic properties of nitride QDs are dominated by the large built-in piezo- and pyroelectric fields, which lead to a pronounced red-shift of excitonic transition energies and extremely long radiative lifetimes in large GaN/AlN QDs. In $In_xGa_{1\text{-}x}N$/GaN QDs these fields induce a pronounced dependence of the radiative excitonic lifetimes on the exact QD shape and composition. Based on these results it is demonstrated that the multi-exponential ensemble-PL decay of $In_xGa_{1-x}N$/GaN QDs frequently observed in experiments can be fully understood in terms of variations of the radiative lifetimes in an inhomogeneous QD ensemble and without dynamical screening effects.

Moreover, it is shown that nitride QDs exhibit a polarization mechanism based on valence-band mixing effects that leads to a separation of differently polarized emission lines more than one order of magnitude larger than the fine-structure splitting in InAs/GaAs QDs. Single-QD CL spectra with up to five narrow lines that are linearly polarized in orthogonal direction are explained based on this effect. Shortly after the mechanism was published for $In_xGa_{1-x}N$/GaN QDs,[29;38] similar polarization effects have been reported for *c*-plane GaN/AlN QDs.[32;39] It is also shown in this work that the same polarization mechanism applies to GaN/AlN QDs and that the optical polarization of the interband recombination channels in these QDs is controlled by anisotropic strain in the basal plane. Hence, the results of this work provide the opportunity to manipulate the optical polarization in opto-electronic devices based on nitride QDs.

1.2 Thesis Structure

This work is organized in eight chapters: After a brief introduction to the fundamentals of self-assembled QDs and, particularly, group-III nitride QDs in chapter 2, the $\mathbf{k}\cdot\mathbf{p}$ method used in the present work will be described in detail in chapter 3. In chapter 4 $\mathbf{k}\cdot\mathbf{p}$ parameters for the group-III nitrides are derived from first-principle band-structure calculations. Chapter 5 deals with the valence-band structure of strained wurtzite group-III nitrides. The results of the electronic structure calculations for QDs will be given thereafter: $In_xGa_{1-x}N$/GaN QDs are discussed in chapter 6, GaN/AlN QDs in chapter 7. Each of the chapters 4 through 7 will be concluded by a brief summary. A conclusion and outlook for the entire thesis will be given in chapter 8.

2 Fundamentals

In this chapter fundamental concepts helpful for the comprehension of this thesis will be explained. First a brief introduction to self-assembled quantum dots (QDs) in general will be given in Sec. 2.1. Then, the specific characteristics of group-III-nitride QDs (Sec. 2.2) and, particularly, the wurtzite-nitride typical polarization effects (Sec. 2.3) will be discussed.

2.1 Three-dimensional Confinement in Self-assembled Quantum Dots

Semiconductor QDs[40;41] are nanometer-scale objects (composed of a semiconducting material) that confine charge carriers in all three spatial directions. Self-assembled QDs are typically grown by epitaxial methods, such as molecular-beam epitaxy or metal-organic chemical vapor deposition,[42] by deposition of the QD material on a different semiconductor matrix. Quantum dots in most material systems are grown in the strain-induced (i.e. induced by the lattice mismatch between matrix and QD material) Stranski-Krastanow or Volmer-Weber growth modes,[43] as in the case of GaN/AlN QDs, which are the subject of Chap. 7. Depending on the material system and growth conditions the formation of three-dimensional islands (QDs) is energetically favorable over the formation of closed layers. The formation of islands may occur directly (Volmer-Weber growth mode) or after exceeding a critical layer thickness (Stranski-Krastanow growth mode) between 1 and 2 monolayers. But also other growth modes that leads to the formation of nanometer-scale localization centers are possible. For instance, the $In_xGa_{1-x}N$/GaN QDs discussed in Chap. 6 are formed by composition fluctuations in thin $In_xGa_{1-x}N$ layers.[24;44] Here, the driving forces for the QD formation are not fully understood, yet. The different growth mode results in significant differences of the QD shape compared to Stranski-Krastanow QDs (cf Sec. 6.1).

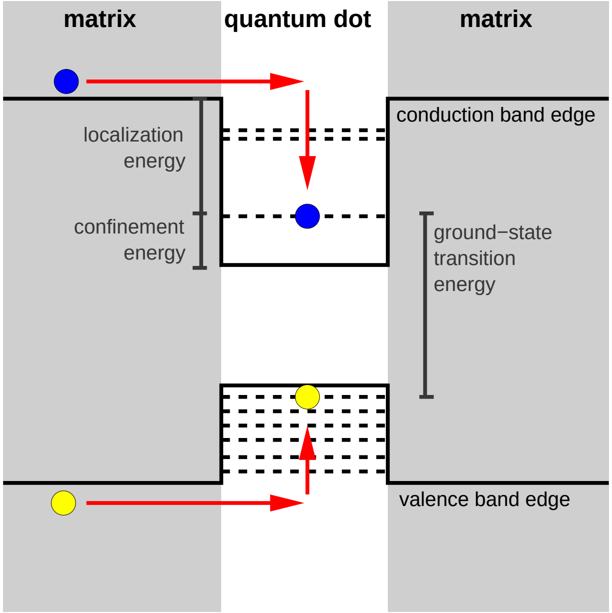

Figure 2.1: Schematic single-particle energy level diagram of a type-I QD. The hole spectrum is typically denser than the electron spectrum due to the larger effective masses of holes. In an experiment free carriers can be generated in the matrix and then captured into the QD where they recombine radiatively, emitting a photon with an energy that is characteristic for the QD.

Electronically, two different classes of QDs can be distinguished by the band offsets at the hetero-interfaces between QD and matrix material: If the conduction-band edge inside the QD lies below that of the matrix *and* the valence-band (VB) edge inside the QD above the VB edge of the matrix, the QD is named a type-I dot. If one of both alignments is the other way around, the dot is of type II. All QDs considered in this work are type-I. Thus, if the QDs are large enough and the band discontinuities are not to shallow, the QDs contain binding energy levels for electrons *and* holes. A schematic one-dimensional energy-level diagram is shown in Fig. 2.1. Inside the QD the density of states is discrete for electrons and holes, but the level spacing between different hole states is typically much smaller due to their larger effective masses. The mechanism of a typical experiment with non-resonant excitation is also sketched in Fig. 2.1: electron-hole pairs are generated in the matrix by, e.g., absorption of light (photoluminescence) or current injection (electroluminescence) and are then captured into the QDs. The confined charge carriers then recombine within the QD, emitting a photon with an energy that is characteristic for the QD.

An important subject of the present work is to calculate the wave-functions and energies of the confined electron and hole states for realistic QD structures. After including additional few-particle effects, the characteristic transition energies of the ground states and the excited states of the QDs are obtained from these calculations. The transition energies depend crucially on parameters like size, shape, and chemical composition of the QDs and, of course, on the magnitude of the built-in piezo- and pyroelectric fields (cf Sec. 2.3). These dependencies will be analyzed in detail for $In_xGa_{1-x}N/GaN$ and GaN/AlN QDs in Chap. 6 and 7.

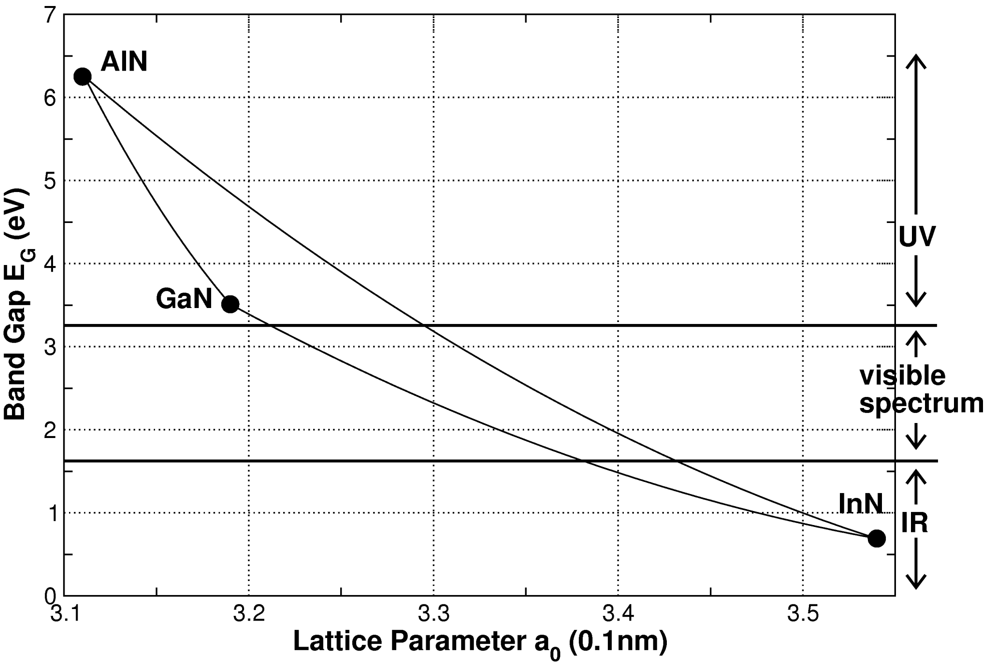

Figure 2.2: Band gap and in-plane lattice parameter a_0 of the group-III nitrides AlN, GaN, and InN and their ternary alloys. The vertical black lines indicate the border between visible and ultra-violet spectrum ($\approx$ 380 nm) and visible and infra-red spectrum ($\approx$ 750 nm), respectively.

2.2 Nitride-based Quantum Dots

So far, three different groups of nitride QDs[45] have been realized: $In_xGa_{1\text{-}x}N/GaN$,[22–24;26–28] GaN/Al(Ga)N,[30;31;33–36] and InN/GaN.[37] From an application-driven point of view, the different material systems can be classified by the spectral range they cover (Fig. 2.2). Neglecting red-shifts induced by the quantum-confined Stark effect (cf Sec. 2.3), QDs emit photons with an energy higher than the band gap of the QD material. The difference between the band gap of the QD material and the QD ground state energy is attributed to confinement effects and strain-induced band-shifts. Thus, GaN/AlN QDs emit in the ultra-violet spectral region, InGaN/GaN QDs can be used for the visible spectrum, and InN/GaN QDs will, in the future, extend the spectral range of nitride QDs to the infra red. The latter is of particular importance for fibre-optical communication technologies. However, this picture does not hold once the quantum-confined Stark effect (cf Sec. 2.3) is included in the consideration: The built-in piezo- and pyroelectric fields inside the QDs induce a red-shift of the transition energies. Indeed, GaN/AlN QDs have frequently been reported to emit light well below the band gap of GaN in the visible spectrum.[46–48] This effect can, however, hardly be exploited technologically. The long emission wave lengths is implementable attainable only in devices that operate at very low injection densities, such as single-photon emitters. (At higher excitation densities, in devices like light-emitting diodes or laser diodes the injected charge carriers screen the electric fields and the emission wave length shifts back to higher energies.) But, these devices would then suffer from very low repetition rates due to the (field-induced) extremely long radiative excitonic lifetimes, rendering them practically unusable.

Another property distinguishing the three different material systems are the effective electron and hole masses in the QD material. This shall be discussed here using the effective electron masses as an example. All three materials, AlN, GaN, and InN, show much larger effective masses [$m_{\mathrm{eff}}(\mathrm{InN}) \approx 0.07 m_0$, $m_{\mathrm{eff}}(\mathrm{GaN}) \approx 0.20 m_0$, $m_{\mathrm{eff}}(\mathrm{AlN}) \approx 0.33 m_0$] than, e.g., InAs [$m_{\mathrm{eff}}(\mathrm{InAs}) \approx 0.03 m_0$], which is a well-established QD material. Regarding confinement effects, this means that a GaN QD has to be about 6-7 times smaller than a comparable InAs QD in order to achieve comparable confinement/quantization effects (neglecting effects arising from the different band offsets to the matrix material). On the other hand, the lower limit for the QD size, at which the QD does not contain localized electron levels any more, is lowered by the same factor. A similar line of thought applies, of course, to the differences between the different nitride QDs, because the effective electron mass of InN is three times smaller than that of GaN, resulting in larger quantization energies in $\mathrm{In_xGa_{1\text{-}x}N}$/GaN QDs than in GaN/AlN QDs.

Nevertheless, all nitride QDs have a number of common characteristics, such as the huge built-in polarization fields (Sec. 2.3) and a rich-featured spectrum of confined hole states that results from the complex VB structure of strained group-III-nitrides (Chap. 5).

2.3 Polarization Fields in Group-III Nitride Heterostructures

A prominent feature of nitride-based nanostructures are the large built-in electrostatic fields, which occur due to piezo- and pyroelectric polarization effects. Piezoelectric polarizations are induced by non-hydrostatic strain along polar axes[49] of the crystal (here the [0001] axis). Thus, it only occurs in strained structures, such as the non-lattice-matched nanostructures considered in this work. Pyroelectric, or spontaneous, polarization occurs without any external stress applied. Due to the deviation of the bonds from the ideal tetrahedral structure in wurtzite, the dipoles of the polar bonds in each unit cell do not completely cancel, resulting in a residual dipole moment of the hole unit cell. The effect increases if the crystal structure deviates from ideal wurtzite, i.e. if the a_0/c_0 ratio and/or the internal lattice parameter u deviate from their ideal values.[50]

In this section, these fields shall be discussed using two examples: A GaN/AlN quantum well (QW) and an $\mathrm{In_{0.2}Ga_{0.8}N}$/GaN QW, both grown along the [0001] direction and with a thickness

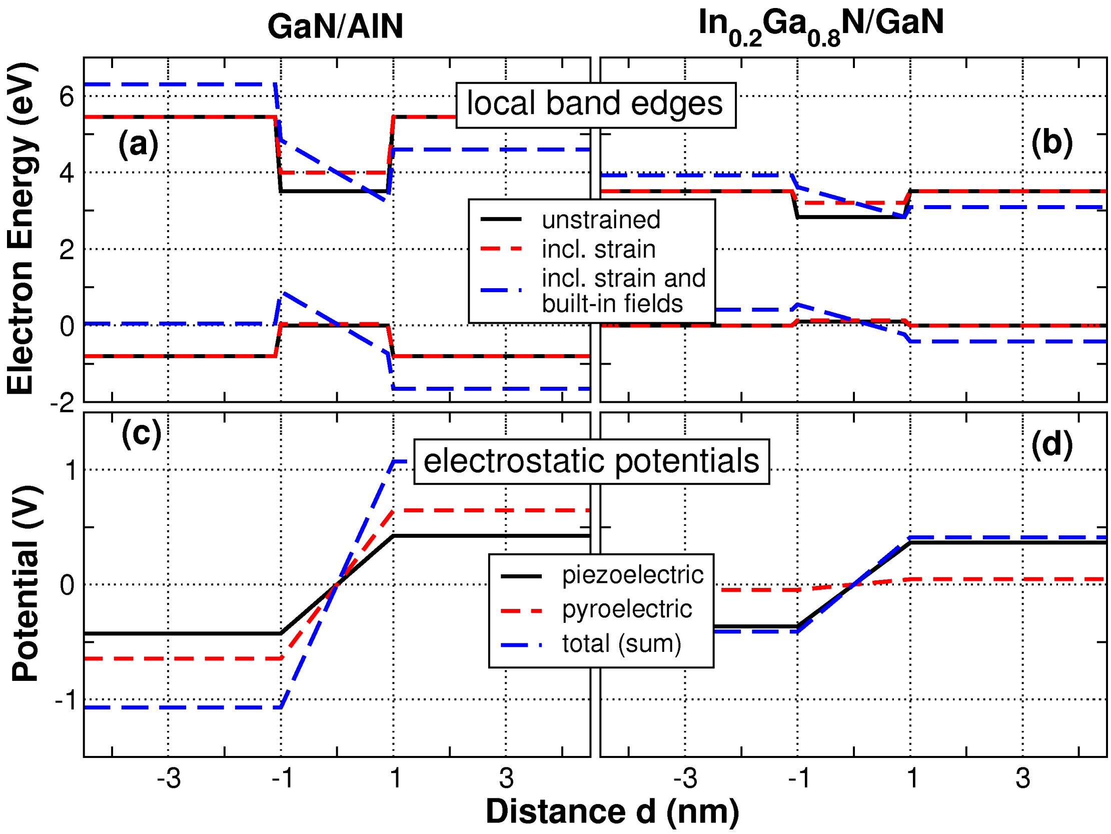

Figure 2.3: Local band-edge profiles in a GaN/AlN (a) and an $In_{0.2}Ga_{0.8}N$/GaN (b) QW along [0001]. The built-in electrostatic potentials (c,d) consist of a piezoelectric and a pyroelectric part.

of 2 nm. Both examples can be solved analytically. Only the mathematical detail needed for the discussion in this section will be given here. Complete details on how the calculations are performed for QDs can be found in Chap. 3.

Both QWs are compressively strained in the growth plane (here, *x*-*y*-plane), resulting in a relaxation (an extension) along the growth direction (here, *z* direction). The strain in the *x*-*y* plane induced by the lattice mismatch is $\varepsilon_{xx} = \varepsilon_{yy} = -0.022$ (-0.024) for the $In_{0.2}Ga_{0.8}N$/GaN (GaN/AlN) QW, resulting in a tensile lattice distortion along *z* of

$$\varepsilon_{zz} = -\frac{2C_{13}}{C_{33}}\varepsilon_{xx/yy} = 0.012 \quad (0.013). \tag{2.1}$$

The strain shifts the band edges inside the QWs; unstrained and strained local band-edge profiles are shown in Fig. 2.3(a,b) (black solid and red dashed lines, respectively).

The pyroelectric polarization depends only on the material and has a finite component only along [0001], which is denoted P_{sp}. The values of P_{sp} used in this work are $-0.034\,\frac{\mathrm{C}}{\mathrm{m}^2}$, $-0.090\,\frac{\mathrm{C}}{\mathrm{m}^2}$, and $-0.030\,\frac{\mathrm{C}}{\mathrm{m}^2}$ for GaN, AlN, and $\mathrm{In}_{0.2}\mathrm{Ga}_{0.8}\mathrm{N}$, respectively (cf appendix A). The piezoelectric polarization, in contrast, is strain-induced. For the systems considered in this chapter its only non-vanishing component is also along [0001]. The compressive biaxial strain and the Ga-faced orientation (growth along [0001]) induce a polarization field in growth direction. The piezoelectric polarization inside the QWs is

$$P_{\mathrm{pz,z}} = 2e_{31}\varepsilon_{\mathrm{xx/yy}} + e_{33}\varepsilon_{\mathrm{zz}} = 0.034\,\frac{\mathrm{C}}{\mathrm{m}^2} \tag{2.2}$$

for $\mathrm{In}_{0.2}\mathrm{Ga}_{0.8}\mathrm{N}$/GaN and $0.037\,\frac{\mathrm{C}}{\mathrm{m}^2}$ for GaN/AlN. The piezoelectric polarization outside the QW is zero, because the matrix material is unstrained for ideal QWs (infinitely extended in the growth plane and no thickness fluctuations).

The piezo- and pyroelectric polarizations are rather abstract quantities. More tangible are the piezo- and pyroelectric charges that occur at discontinuities of the polarizations. The surface charges ρ at the hetero interfaces of the QW can be calculated by $\rho = \frac{\partial P_i}{\partial z}$. The electric field and potential inside the QW is obtained from these charges analogous to the field in a plane-parallel capacitor.[51] The field outside the QW (i.e. in the matrix) cannot be calculated without further information about how the structure continues in larger distance from the QW.

The local band edges including the electrostatic potentials are also shown Fig. 2.3(a,b) (blue long-dashed lines). Figures 2.3(c,d) show the decomposition of the total electrostatic potentials into the piezo- and pyroelectric parts. In both systems the electrostatic potentials are of the same order of magnitude as the band offsets at the hetero junctions. Also, in both systems the electron energy inside the QW decreases along [0001] (i.e., the electrostatic potential increases). Therefore, an electron in the QW is expected to be located close to the upper hetero interface and a hole at the lower one.

In the GaN/AlN QW the potential arising from the pyroelectric part [red dashed line in Fig. 2.3(c)] is larger than the piezoelectric one (black solid line). In sum the potential drop inside the QW exceeds 2 eV. In the $\mathrm{In}_{0.2}\mathrm{Ga}_{0.8}\mathrm{N}$/GaN QW pyroelectric effects are almost negligible; the potential drop inside the QW of almost 1 eV can be attributed almost solely to its piezoelectric component.

Regardless of the origin of the built-in fields, in both cases they have a large impact on the electronic and optical properties of the nanostructures. The aforementioned field-induced band bending and resulting spatial separation of electrons and holes result in a significant red-shift of excitonic transition energies and increase of the radiative lifetimes due to the reduced overlap

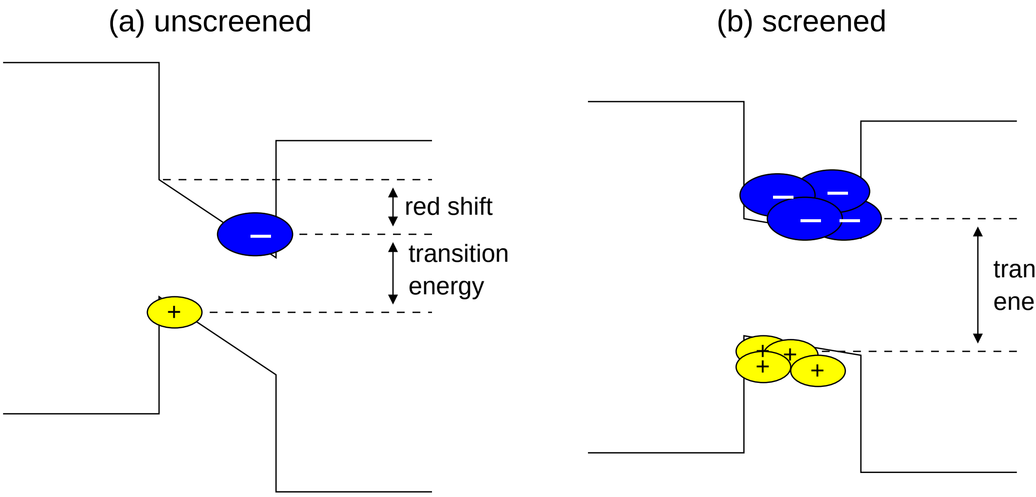

Figure 2.4: Schematics of the quantum-confined Stark effect (QCSE). (a) The built-in electrostatic fields cause a band bending inside the QD, which in turn leads to a spatial separation of the charge carriers and a red shift of the transition energy. (b) A large number of charge carriers inside the QD can screen the electric fields compensating the effects of the QCS

of electron and hole wave function [Fig. 2.4(a)]. An upper limit for the red-shift ΔE_X is given by the potential drop inside the nanostructure, i.e. $\Delta E_X < 2.1\,\mathrm{eV}$ for the GaN/AlN QW and $\Delta E_X < 0.8\,\mathrm{eV}$ for the $\mathrm{In_{0.2}Ga_{0.8}N}$/GaN QW. The whole effects (charge separation and red-shift of the transition) is known as the *quantum confined Stark effect (QCSE)*.[52] It is important to note that a large number of electron-hole pairs in the QW leads to a screening of the built-in fields by the electron and hole charges themselves, which in turn leads to a compensation of the effects of the QCSE, i.e. to a blue shift of the emission [Fig. 2.4(b)]. When interpreting spectroscopic results on (*c*-plane) group-III nitride nanostructures it is important to note whether the screened or unscreened luminescence is observed. The difference between the screened and unscreened emission energy for, e.g., GaN/AlN QDs exceeds 1 eV for large QDs.[48;53]

3 The k·p Method for Strained Semiconductor Nanostructures

For the electronic structure calculations presented in this thesis a three-dimensional strain-dependent eight-band **k·p** model has been used. The model is implemented on a finite differences grid within the envelope function scheme.[54] It includes piezoelectric and pyroelectric effects as well as crystal-field splitting and spin-orbit interaction. Few-particle states are calculated using a self-consistent Hartree (mean field) approach. The **k·p** model is based on the one originally developed by Stier *et al.*,[55] which has been successfully applied to various types of zinc-blende material quantum dots (QDs).[55–57] The model has been extended to QDs in materials with wurtzite crystal structure.

K·p models for wurtzite nitride QDs have been presented before, most prominent by Andreev and O'Reilly[58] and Fonoberov and Balandin.[59] The differences between these two models and the model used in the present work have been discussed in Ref. 60 and shall be summarized briefly here:

(i) The method introduced by Andreev and O'Reilly[58] includes all important effects except spin-orbit splitting, which has been neglected in order to reduce the dimensions of the Hamiltonian from 8 x 8 to 4 x 4. This simplification can be justified, given that the spin-orbit splitting is small in GaN (17 meV) and AlN (19 meV) and modifies the absolute value of the exciton transition energies roughly by the same amount. InN shows an even smaller spin-orbit splitting of 5 meV.[61] However, neglecting spin-orbit splitting leads to an artificial degeneracies in the hole spectra, in particular of the hole ground states.[60]

(ii) Fonoberov and Balandin[59] use a 6 x 6 Hamiltonian for the valence bands (VBs), and the effective mass approximation for the conduction band (CB). This method neglects the coupling between VBs and CB, which is justified for large band-gap materials such as GaN and AlN. InN, in contrast, has a much smaller band gap of ≈ 0.7 meV (cf Chap. 4) and therefore requires the inclusion of VB/CB-coupling.

Meanwhile, also a full-fledged eight-band $\mathbf{k}\cdot\mathbf{p}$ implementation for for wurtzite and zinc-blende QDs is (freely) available within the next**nano**^{3} project.[62] Calculations for group-III-nitride QDs using the atomistic tight-binding model[63] have been presented for InGaN/GaN-QDs,[64] GaN/AlN-QDs,[65] and recently for pure InN/GaN-QDs.[66;67] An in-depth comparative discussion is beyond the scope of the work.

In the following sections the method used in the present work is described in detail, starting with the calculation of the strain field (Sec. 3.1) and the built-in electrostatic potential (Sec. 3.2), followed by the description of the $\mathbf{k}\cdot\mathbf{p}$ Hamiltonian (Sec. 3.3), the calculation of exciton energies (Sec. 3.4), recombination probabilities, and radiative lifetimes (Sec. 3.5). All equations are given for wurtzite crystals.

3.1 Strain Field

The correct description of the strain field inside the QDs and in their direct vicinity is crucial to a proper description of the QD's electronic properties. The inhomogeneous strain field modifies the electronic properties of the QDs in two separate ways: directly by strain-induced band shifts and indirectly by strain-induced piezoelectric polarizations.

In the present work the strain field has been calculated using the continuum mechanical model,[68] by solving the fundamental equations:

$$\frac{\partial\sigma_{\mathrm{i1}}}{\partial x}+\frac{\partial\sigma_{\mathrm{i2}}}{\partial y}+\frac{\partial\sigma_{\mathrm{i3}}}{\partial z}=0 \qquad (i=1,2,3) \quad . \tag{3.1}$$

Here, x,y,z are cartesian coordinates, and σ_{ij} are the components of the stress tensor. In linear approximation (Hooke's Law) they are related to those of the strain tensor $\varepsilon_{\mathrm{ij}}$ by

$$\begin{pmatrix} \sigma_{11} \\ \sigma_{22} \\ \sigma_{33} \\ \sigma_{23} \\ \sigma_{13} \\ \sigma_{12} \end{pmatrix} = \hat{\mathbf{C}} \begin{pmatrix} \varepsilon_{11} \\ \varepsilon_{22} \\ \varepsilon_{33} \\ 2\varepsilon_{23} \\ 2\varepsilon_{13} \\ 2\varepsilon_{12} \end{pmatrix} \quad , \tag{3.2}$$

where—for wurtzite-type crystals and the z-axis along the [0001]-direction—the tensor of compliances $\hat{\mathbf{C}}$ is given by[69]

$$\hat{\mathbf{C}} = \begin{pmatrix} C_{11} & C_{12} & C_{13} & 0 & 0 & 0 \\ C_{12} & C_{11} & C_{13} & 0 & 0 & 0 \\ C_{13} & C_{13} & C_{33} & 0 & 0 & 0 \\ 0 & 0 & 0 & C_{44} & 0 & 0 \\ 0 & 0 & 0 & 0 & C_{44} & 0 \\ 0 & 0 & 0 & 0 & 0 & \frac{C_{11}-C_{12}}{2} \end{pmatrix} \quad . \tag{3.3}$$

3.2 Built-in Electric Fields: Piezo- and Pyroelectric Potentials

In contrast to QDs in most other material systems, such as the well-known InAs/GaAs system, polarization effects play a dominant role in wurtzite group-III-nitride QDs for two reasons. First, in wurtzite semiconductors biaxial strain in the basal plane [(0001)-plane] causes a piezoelectric field parallel to the *C*-axis ([0001]-axis). Since most heterostructures are grown on the (0001)-plane, the corresponding biaxial strain is usually large. Second, due to the high ionicity of the bonds, the piezoelectric constants of group-III-nitrides are significantly larger than those of most other semiconductor materials.[70]

In additon to the piezoelectric fields, spontaneous (pyroelectric) polarization occurs in wurtzite crystals. For GaN/AlN QDs, the built-in potentials resulting from the spontaneous polarization are of the same order of magnitude as those resulting from piezoelectric effects.[58;59] For $\mathrm{In_xGa_{1\text{-}x}N}$/GaN QDs, however, the spontaneous-polarization potential is much weaker than the piezoelectric one, because the difference between the spontaneous polarization constants of InN and GaN is much smaller (cf Sec. 2.3).

The total polarization $\mathbf{P}$ in wurtzite-type semiconductors is given by

$$\mathbf{P} = \mathbf{P}_{\mathrm{PZ}} + \mathbf{P}_{\mathrm{SP}} \quad , \tag{3.4}$$

where $\mathbf{P}_{\mathrm{PZ}}$ is the strain-induced piezoelectric polarization and $\mathbf{P}_{\mathrm{SP}}$ the spontaneous polarization.

The piezoelectric polarization $\mathbf{P}_{\mathrm{PZ}}$ can be calculated from the strain tensor components by

$$\mathbf{P}_{\mathrm{PZ}} = \hat{\mathbf{e}} \begin{pmatrix} \varepsilon_{11} \\ \varepsilon_{22} \\ \varepsilon_{33} \\ 2\varepsilon_{23} \\ 2\varepsilon_{13} \\ 2\varepsilon_{12} \end{pmatrix} \quad . \tag{3.5}$$

Here, $\hat{\mathbf{e}}$ is the electro-mechanical tensor for wurtzite crystals. With the positive z-axis along the [0001]-direction, it takes the form:

$$\hat{\mathbf{e}} = \begin{pmatrix} 0 & 0 & 0 & 0 & e_{15} & 0 \\ 0 & 0 & 0 & e_{15} & 0 & 0 \\ e_{31} & e_{31} & e_{33} & 0 & 0 & 0 \end{pmatrix} \quad . \tag{3.6}$$

The spontaneous polarization $\mathbf{P}_{\mathrm{SP}}$ is given by

$$\mathbf{P}_{\mathrm{SP}} = \begin{pmatrix} 0 \\ 0 \\ P_{\mathrm{SP}} \end{pmatrix} \quad . \tag{3.7}$$

The corresponding electrostatic potential $\phi(\mathbf{r})$ is obtained by first calculating the polarization charge density $\rho(\mathbf{r})$, using

$$\rho(\mathbf{r}) = -\nabla \cdot \mathbf{P}(\mathbf{r}), \tag{3.8}$$

and subsequently solving Poisson's Equation:

$$\varepsilon_0 \nabla \cdot [\varepsilon_{\mathrm{r}}(\mathbf{r}) \nabla \phi(\mathbf{r})] = \rho(\mathbf{r}) \quad . \tag{3.9}$$

3.3 The K·p-Hamiltonian

The **k·p**-Hamiltonian used in the present work is based on the one introduced by Gershoni *et al.*[71] for zinc-blende crystals and its extension to wurtzite crystals structures on Refs. 72–74.

Following Gershoni *et al.*[71] the Hamiltonian is expanded into the basis

$$\left(|S\uparrow\rangle, |P_{\mathrm{x}}\uparrow\rangle, |P_{\mathrm{y}}\uparrow\rangle, |P_{\mathrm{z}}\uparrow\rangle, |S\downarrow\rangle, |P_{\mathrm{x}}\downarrow\rangle, |P_{\mathrm{y}}\downarrow\rangle, |P_{\mathrm{z}}\downarrow\rangle\right)^T \quad , \tag{3.10}$$

and takes the block matrix form

$$\hat{H} = \begin{pmatrix} G(\mathbf{k}) & \Gamma \\ -\overline{\Gamma} & \overline{G}(\mathbf{k}) \end{pmatrix} \quad . \tag{3.11}$$

$G(\mathbf{k})$ and Γ are both 4 x 4 matrices and the overline denotes the complex conjugate. G decomposes into a sum of 4 x 4 matrices:

$$G = G_1 + G_2 + G_{\mathrm{SO}} + G_{\mathrm{ST}} \quad . \tag{3.12}$$

The matrix G_1 represents the pure 4 x 4-$\mathbf{k}\cdot\mathbf{p}$ description of the conduction and valence band neglecting all remote band contributions. For wurtzite crystals it is given by

$$G_1 = \begin{pmatrix} \tilde{E}_{\mathrm{C}} + \Delta_{\mathrm{CR}} + \frac{\hbar^2 k^2}{2m_0} & iP_2 k_{\mathrm{x}} & iP_2 k_{\mathrm{y}} & iP_1 k_{\mathrm{z}} \\ -iP_2 k_{\mathrm{x}} & E'_{\mathrm{V}} + \Delta_{\mathrm{CR}} + \frac{\hbar^2 k^2}{2m_0} & 0 & 0 \\ -iP_2 k_{\mathrm{y}} & 0 & E'_{\mathrm{V}} + \Delta_{\mathrm{CR}} + \frac{\hbar^2 k^2}{2m_0} & 0 \\ -iP_1 k_{\mathrm{z}} & 0 & 0 & E'_{\mathrm{V}} + \frac{\hbar^2 k^2}{2m_0} \end{pmatrix} \quad . \tag{3.13}$$

Here, m_0 is the free electron mass. E_{C} and E'_{V} are the conduction and valence band edges, given by

$$E'_{\mathrm{C}} = E_{\mathrm{V}} + E_{\mathrm{G}} + \Delta_{\mathrm{CR}} + \frac{\Delta_{\mathrm{SO}}}{3} + V_{\mathrm{ext}} \quad , \tag{3.14}$$

$$E'_{\mathrm{V}} = E_{\mathrm{V}} + V_{\mathrm{ext}} \quad . \tag{3.15}$$

E_{V} is the average VB edge on an absolute scale [the VB edge of the unstrained matrix material (GaN or AlN) is arbitrarily set to 0 meV throughout this work]. Δ_{SO} and Δ_{CR} are the spin-orbit and crystal-field splitting energies of the given material. V_{ext} can be any additional scalar potential. In our case it is the built-in piezoelectric and pyroelectric potential. $\tilde{E}_{\mathrm{G}}$ is identical to the fundamental band gap E_{G} for all materials with a positive crystal-field splitting Δ_{CR}, i.e. GaN and InN, and $E_{\mathrm{G}} + |\Delta_{\mathrm{CR}}|$ for materials with negative Δ_{CR}, i.e. AlN. The parameters $P_{1/2}$ are proportional to the absolute value of the CB/VB dipole matrix elements at Γ. They are customarily expressed in terms of the Kane parameters $E_{\mathrm{P1/2}}$:

$$P_{1/2} = \sqrt{\frac{\hbar^2}{2m_0} E_{\mathrm{P1/2}}} \quad . \tag{3.16}$$

The matrix G_2 describes the influences of all bands not considered explicitly by the 4 x 4-matrix. For wurtzite crystals it is given by

$$G_2 = \begin{pmatrix} A'_2\left(k_\mathrm{x}^2+k_\mathrm{y}^2\right)+A'_1k_\mathrm{z}^2 & B_2k_\mathrm{y}k_\mathrm{z} & B_2k_\mathrm{x}k_\mathrm{z} & B_1k_\mathrm{x}k_\mathrm{z} \\ B_2k_\mathrm{y}k_\mathrm{z} & L'_1k_\mathrm{x}^2+M_1k_\mathrm{y}^2+M_2k_\mathrm{z}^2 & N'_1k_\mathrm{x}k_\mathrm{y} & N'_2k_\mathrm{x}k_\mathrm{z}-N'_3k_\mathrm{x} \\ B_2k_\mathrm{x}k_\mathrm{z} & N'_1k_\mathrm{y}k_\mathrm{x} & M_1k_\mathrm{x}^2+L'_1k_\mathrm{y}^2+M_2k_\mathrm{z}^2 & N'_2k_\mathrm{y}k_\mathrm{z}-N'_3k_\mathrm{y} \\ B_1k_\mathrm{x}k_\mathrm{z} & N'_2k_\mathrm{z}k_\mathrm{x}+N'_3k_\mathrm{x} & N'_2k_\mathrm{z}k_\mathrm{x}+N'_3k_\mathrm{y} & M_3\left(k_\mathrm{x}^2+k_\mathrm{y}^2\right)+L'_2k_\mathrm{z}^2 \end{pmatrix} . \tag{3.17}$$

The parameters in G_2 are defined in terms of optical matrix elements in, e.g., Ref. 73. The parameters are related to the more commonly used effective electron masses, $m_\mathrm{e}^{\|}$ and $m_\mathrm{e}^{\perp}$, and Luttinger-like parameters, A_i, by

$$\begin{aligned}
A'_1 &= \frac{\hbar^2}{2}\left(\frac{1}{m_\mathrm{e}^{\|}}-\frac{1}{m_0}\right)-\frac{P_1^2}{E_\mathrm{g}} \quad , \\
A'_2 &= \frac{\hbar^2}{2}\left(\frac{1}{m_\mathrm{e}^{\perp}}-\frac{1}{m_0}\right)-\frac{P_2^2}{E_\mathrm{g}} \quad , \\
L'_1 &= \frac{\hbar^2}{2m_0}\left(A_2+A_4+A_5-1\right)+\frac{P_1^2}{E_\mathrm{g}} \quad , \\
L'_2 &= \frac{\hbar^2}{2m_0}\left(A_1-1\right)+\frac{P_2^2}{E_\mathrm{g}} \quad , \\
M_1 &= \frac{\hbar^2}{2m_0}\left(A_2+A_4-A_5-1\right) \quad , \\
M_2 &= \frac{\hbar^2}{2m_0}\left(A_1+A_3-1\right) \quad , \\
M_3 &= \frac{\hbar^2}{2m_0}\left(A_2-1\right) \quad , \\
N'_1 &= \frac{\hbar^2}{2m_0}2A_5+\frac{P_1^2}{E_\mathrm{g}} \quad , \\
N'_2 &= \frac{\hbar^2}{2m_0}\sqrt{2}A_6+\frac{P_1P_2}{E_\mathrm{g}} \quad , \\
N'_3 &= i\sqrt{2}A_7 \quad .
\end{aligned} \tag{3.18}$$

The parameters $B_{1/2}$ occur due to the lack of inversion symmetry in wurtzite crystals. Since no reliable values are available for these parameters, they have been set to zero throughout this work.

The matrices G_{SO} and Γ describe the spin-orbit splitting. They are given by

$$G_{\mathrm{SO}} = \frac{\Delta_{\mathrm{SO}}}{3} \begin{pmatrix} 0 & 0 & 0 & 0 \\ 0 & 0 & -i & 0 \\ 0 & i & 0 & 0 \\ 0 & 0 & 0 & 0 \end{pmatrix} \tag{3.19}$$

and

$$\Gamma = \frac{\Delta_{\mathrm{SO}}}{3} \begin{pmatrix} 0 & 0 & 0 & 0 \\ 0 & 0 & 0 & 1 \\ 0 & 0 & 0 & -i \\ 0 & -1 & i & 0 \end{pmatrix} \quad . \tag{3.20}$$

G_{ST} describes the strain-dependent part of the Hamiltonian:

$$G_{ST} = \begin{pmatrix} a_2\left(\varepsilon_{\mathrm{xx}}+\varepsilon_{\mathrm{yy}}\right) + a_1\varepsilon_{\mathrm{zz}} & 0 & 0 & 0 \\ 0 & l_1\varepsilon_{\mathrm{xx}}+m_1\varepsilon_{\mathrm{yy}} + m_2\varepsilon_{\mathrm{zz}} & n_1\varepsilon_{\mathrm{xy}} & n_2\varepsilon_{\mathrm{xz}} \\ 0 & n_1\varepsilon_{\mathrm{xy}} & m_1\varepsilon_{\mathrm{xx}}+l_1\varepsilon_{\mathrm{yy}} + m_2\varepsilon_{\mathrm{zz}} & n_2\varepsilon_{\mathrm{yz}} \\ 0 & n_2\varepsilon_{\mathrm{xz}} & n_2\varepsilon_{\mathrm{yz}} & m_3\left(\varepsilon_{\mathrm{xx}}+\varepsilon_{\mathrm{yy}}\right) + l_2\varepsilon_{\mathrm{zz}} \end{pmatrix} \quad . \tag{3.21}$$

Here, a_1 and a_2 are the CB deformation potentials. The parameters l_{i}, n_{i}, and m_{i} are related to the VB deformation potentials D_{i} by

$$\begin{aligned} l_1 &= (D_2+D_4+D_5) \quad , \\ l_2 &= D_1 \quad , \\ m_1 &= (D_2+D_4-D_5) \quad , \\ m_2 &= (D_1+D_3) \quad , \\ m_3 &= D_2 \quad , \\ n_1 &= 2D_5 \quad , \\ n_2 &= \sqrt{2}D_6 \quad . \end{aligned} \tag{3.22}$$

3.4 Excitonic Corrections: Self-consistent Hartree-method

In order to predict the energies and properties of excitons and excitonic complexes correctly additional few-particle effects have to be taken into account. These are the direct (mean-field) Coulomb interaction between all charge carriers confined in the QD, exchange effects, and the quantum-mechanical Coulomb correlation. A method to account for all three effects is the configuration interaction (CI) scheme,[75] where the few-particle Hamiltonian is expanded into a basis of anti-symmetrized products of the bound single-particle states. This method has been applied successfully to QDs in other material systems, such as InAs/GaAs.[76–78] However, due to the large computational effort involved in solving the Poisson integrals in three dimensions and, in many cases, the lack of a sufficiently large number of bound single-particle states, the CI basis for three-dimensional QD calculations has to remain incomplete. Whether or not the expansion into the incomplete basis yields acceptable results depends, of course, on the basis size, but also crucially on the size and chemical composition of the QDs. In a simplified picture, in which the individual wave-functions of the particles in a few-particle complex are separable, e.g. Hartree (mean-field) ansatz, the wave-function of each particle changes its shape, size, and position in response to the Coulomb interaction with the other particles. Hence, the wave functions of the particles in the complex differ from the corresponding single-particle wave functions; this effect will be denoted *wave-function renormalization* in the following. The question with respect to the CI expansion is whether or not the (incomplete) CI basis is able to reproduce the renormalized wave functions. Due to the small effective masses of InAs, confinement effects are strong in InAs/GaAs QDs. Thus, renormalization effects are small and the resulting few-particle wave-function is well-approximated by Slater determinants of the bound single-particle wave functions; a small CI basis yields satisfying results. This has been demonstrated by convergence tests and comparison to quantum monte-carlo simulations.[79;80] The effective masses of GaN and $\mathrm{In_xGa_{1\text{-}x}N}$, however, are much larger. Therefore, renormalization effects are stronger. Moreover, the charge carriers are spatially separated by the large built-in electrostatic fields. In a few-particle complex the separation is reduced by the attractive Coulomb interaction between electrons and holes; consequently a (small) CI basis formed from the single-particle states cannot reproduce the few-particle wave functions accurately. $\mathrm{In_xGa_{1\text{-}x}N}$/GaN QDs additionally do not contain enough bound electron levels to form an appropriate CI basis.

For the reason detailed above a simpler model will be applied in this work, the self-consistent Hartree method.[81] Although this approach does not account for exchange and correlation effects, it has the advantage that it can be performed self-consistently. Thus, at least the direct (mean-field) Coulomb interaction is accounted for correctly.

In the Hartree approximation the ansatz for the few-particle wave function $\Psi(\mathbf{r}_1,\ldots,\mathbf{r}_\mathrm{n})$ is given as a product of single-particle wave functions $\varphi_\mathrm{i}(\mathbf{r}_\mathrm{i})$:

$$\Psi = \prod_\mathrm{i} \varphi_\mathrm{i} \quad . \tag{3.23}$$

The particles interact solely through the direct Coulomb interaction; thus, the total energy of the few-particle state *i* is given by

$$\begin{aligned} E &= \sum_\mathrm{i}^{n} d \int \varphi_\mathrm{i}^*(\mathbf{r}) H \varphi_\mathrm{i}(\mathbf{r}) \mathrm{d}^3\mathbf{r} \\ &+ \frac{1}{2} \sum_{\substack{\mathrm{i,j} \\ \mathrm{i} \neq \mathrm{j}}}^{\mathrm{n,n}} \frac{q_\mathrm{i} q_\mathrm{j}}{4\pi\varepsilon_0} \int\int \frac{|\varphi_\mathrm{i}(\mathbf{r})|^2 |\varphi_\mathrm{i}(\mathbf{r}')|^2}{\varepsilon_\mathrm{r}(\mathbf{r}')|\mathbf{r}-\mathbf{r}'|^2} \mathrm{d}^3\mathbf{r}\mathrm{d}^3\mathbf{r}' \quad . \end{aligned} \tag{3.24}$$

Here, n is the number of participating particles and q_i is the charge of the i-th particle, i.e., $-|e|$ for electrons and $|e|$ for holes; H is the single-particle Hamiltonian. Equation (3.24) is minimized self-consistently in order to obtain the few-particle corrections.

3.5 Transition Probabilities and Radiative Lifetimes

An important property of a confined exciton is its recombination probability, i.e., its radiative lifetime. The radiative lifetimes τ_rad of the confined excitons can be calculated by[82]

$$\tau_\mathrm{rad} = \frac{2\pi\varepsilon_0 m_0 c_0^3 \hbar^2}{n e^2 E_\mathrm{ex}^2 f_\mathrm{eff}} \quad . \tag{3.25}$$

Here, ε_0 is the permittivity of free space, m_0 the free-electron mass, c_0 the vacuum speed of light, $\hbar$ the reduced Planck constant, and E_ex the transition energy of the exciton. n is the refractive index of the matrix material (GaN or AlN in this work), which can be described as a function of the emission wavelength by a Sellmeier-type law (cf appendix A). The effective oscillator strength f_eff has been calculated by integrating the (anisotropic) oscillator strength $f_\mathbf{e}$ over the unit sphere:

$$f_\mathrm{eff} = \frac{1}{4\pi} \int_{\partial O} f_\mathbf{e} \mathrm{d}\mathbf{e} \quad ; \quad f_\mathbf{e} = \frac{2\hbar^2}{m_0 E_\mathrm{ex}} |\langle \Psi_\mathrm{e} | \mathbf{e} \cdot \hat{\mathbf{p}} | \Psi_\mathrm{h} \rangle|^2 \quad . \tag{3.26}$$

Here, $|\Psi_\mathrm{j}\rangle$ are the $\mathbf{k}\cdot\mathbf{p}$ electron and hole wave functions, which consists of a sum over all $\mathbf{k}\cdot\mathbf{p}$ basis states $|i\rangle$ (Bloch functions) multiplied with the respective envelope functions φ_i: $|\Psi_\mathrm{j}\rangle =$

$\sum_{\mathrm{i}=1}^{8} \varphi_{\mathrm{i}} |i\rangle$. When calculating the matrix elements contribution arising from the Bloch parts and the envelope-function parts of the wave functions have been accounted for. **e** is a unit vector indicating the polarization of the light.

4 Material Parameters for Group-III Nitrides

The correct choice of material parameters is crucial for the quality of simulations of nanostructures and/or (opto-)electronic devices. This is true not only for the $\mathbf{k}\cdot\mathbf{p}$ simulations, but also for all other methods that can be used to simulate large-scale heterostructures at reasonable computational expense, such as the empirical tight-binding method[63–65;83] or the empirical pseudo-potential method.[84]

All these methods are typically parameterized for bulk structures and are applied to heterostructures with finite size (e.g. micro- and nanostructures). Ideally, the parameters are determined entirely from consistent experimental input. For the group-III-nitrides, however, many of the key band parameters have not been conclusively determined until now despite extensive research effort in this field.[85;86] In a comprehensive review Vurgaftman and Meyer summarized the field of III-V semiconductors in 2001 and recommended up-to-date band parameters for all common compounds and their alloys including the nitrides.[87] But only two years later they realized that most nitride parameters had already been superseded. Therefore, they published a revised and updated description of the band parameters for nitride-containing semiconductors in 2003.[61] While this update includes evidence supporting a revision of the band gap of InN from its former value of 1.9 eV to a significantly lower value around 0.7 eV,[88–92] they had to concede that in many cases experimental information on certain parameters was simply not available.[61] This was mostly due to growth-related difficulties in producing high-quality samples for unambiguous characterization. In the meantime the quality of, e.g., wurtzite InN samples has greatly improved[85] and even the growth of the zinc-blende phase has advanced.[93] Nevertheless, many of the basic material properties of the group-III nitrides are still undetermined or, at least, controversial. On the theoretical side, certain limitations of density-functional theory (DFT) in the local-density approximation (LDA) or generalized gradient approximation—currently the most wide-spread *ab-initio* electronic-structure method for poly-atomic systems—have hindered an unambiguous completion of the missing data.

Here, a consistent set of $\mathbf{k}\cdot\mathbf{p}$ parameters for the zinc-blende and wurtzite phases of GaN, AlN, and InN is derived from first-principle band-structure calculations (Sec. 4.1). To overcome the deficiencies of DFT the parameters are derived from G_0W_0 calculations based on DFT calculations in the exact-exchange optimized effective potential approach (OEPx). It has been previously shown that the OEPx+G_0W_0 approach provides an accurate description of the quasiparticle band structure for GaN, InN and II-VI compounds.[94;95]

However, due to the lack of G_0W_0 calculations for strained states of these materials it was not possible to determine the strain-dependent $\mathbf{k}\cdot\mathbf{p}$ parameters in the same way. Also other parameters needed for the quantum dot simulations, such as elastic constants or piezo- and pyroelectric constants have to be taken from the literature. The complete set of material parameters used for the simulations is given in appendix A.

4.1 Band Dispersion Parameters Derived from G_0W_0 Calculations

In this section a consistent set of $\mathbf{k}\cdot\mathbf{p}$ band parameters [effective masses, Luttinger(-like) and E_P parameters] for AlN, GaN, and InN in the zinc-blende and wurtzite phases will be derived from first-principle calculations in the G_0W_0 approximation. The G_0W_0 method has been combined with DFT calculations in the OEPx approach. A detailed description of the method can be found elsewhere.[94;96] Here, only the derived $\mathbf{k}\cdot\mathbf{p}$ parameters will be discussed and compared to available experimental data (Sec. 4.1.1).

Key energy differences at critical points serve as first indicators of the quality of band-structure calculations. Particularly, the fundamental band gap E_G, which can be accessed easily in experiments, is known with great accuracy for most materials. The G_0W_0 band gaps for the three materials and both phases are reported in Tab. 4.1 together the experimental values. The G_0W_0 value of 0.69 eV for wurtzite InN supports recent observations of a band gap at the lower end of the experimentally reported range. For zinc-blende InN, which has been explored far less experimentally, the calculated band gap of 0.53 eV also agrees well with the recently measured (and Burstein-Moss corrected) 0.6 eV.[112] For GaN the band gaps of both phases are well established experimentally and the G_0W_0 values of 3.24 eV and 3.07 eV agree to within 0.3 eV. For AlN experimental results for the band gap of the wurtzite phase scatter appreciable, whereas for zinc blende only one value has—to the best of the author's knowledge—been reported so far.

	param.	G_0W_0	Exp.	LDA	OEPx
			wurtzite		
wz-AlN	E_g	6.47	6.0-6.3[97–103]	4.29	5.73
	Δ_{CR}	-0.295	-0.230[98]	-0.225	-0.334
wz-GaN	E_g	3.24	3.5[86]	1.78	3.15
	Δ_{CR}	0.034	0.009-0.038[86]	0.049	0.002
wz-InN	E_g	0.69	0.65-0.8[88–90;104–107]		1.00
	Δ_{CR}	0.066	0.019-0.024[107]		0.079
			zinc blende		
zb-AlN	$E_g^{\Gamma-\Gamma}$	6.53		4.29	5.77
	$E_g^{\Gamma-X}$	5.63	5.34[108]	3.28	5.09
zb-GaN	E_g	3.07	3.3[109–111]	1.64	2.88
zb-InN	E_g	0.53	0.6[112]		0.81

Table 4.1: Band gaps (E_g) and crystal-field splittings (Δ_{CR})[113] for the wurtzite and zinc-blende phases of AlN, GaN, and InN. All values are given in eV.

Contrary to GaN, the G_0W_0 band gaps for AlN are larger than the reported experimental ones. It has to be emphasized that the agreement of the G_0W_0 values is significantly better than for DFT calculations. For comparison, also the band gaps and crystal-field splitting energies from LDA and OEPx calculations are given in Tab. 4.1. (For a more detailed comparison of different methods see Ref. 96.) It will be shown in the following section that similarly good agreement with available experimental data is found for the $\mathbf{k}\cdot\mathbf{p}$ parameters derived from the G_0W_0 band structures.

The G_0W_0 band structures of InN, GaN, and AlN in the zinc-blende and wurtzite phases in the vicinity of the Γ-point have been used to directly parameterize a 4 x 4 $\mathbf{k}\cdot\mathbf{p}$ Hamiltonian. To determine the $\mathbf{k}\cdot\mathbf{p}$ Hamiltonian for a given band structure with band gap E_g and crystal-field splitting Δ_{CR} the parameters m_e^i, A_i, γ_i, and E_P^i are fitted. This is achieved by least-square-root fitting of the $\mathbf{k}\cdot\mathbf{p}$ band structure to the G_0W_0 band structure in the vicinity of Γ. For the wurtzite phases the directions Σ, Λ, T, and Δ have been included in the fit, each represented by 22 equidistant **k**-points from Γ to $\frac{M}{8}$ ($\frac{L}{8}$, $\frac{K}{8}$) and 22 equidistant points from Γ to $\frac{A}{4}$. For the zinc-blende phases the directions Σ, Δ, and Λ have been included, each with 22 **k**-points from Γ to $\frac{K}{8}$ ($\frac{X}{8}$, $\frac{L}{8}$).

The parameters obtained by fitting to the G_0W_0 band structures are listed in Tab. 4.2. The resulting $\mathbf{k}\cdot\mathbf{p}$ band structures are plotted in Figs. 4.1 and 4.2 (black solid lines) together with the respective G_0W_0 data (black circles). The excellent agreement of the $\mathbf{k}\cdot\mathbf{p}$ and G_0W_0 band structures illustrates that the band structures of the wurtzite and zinc-blende phases of all three

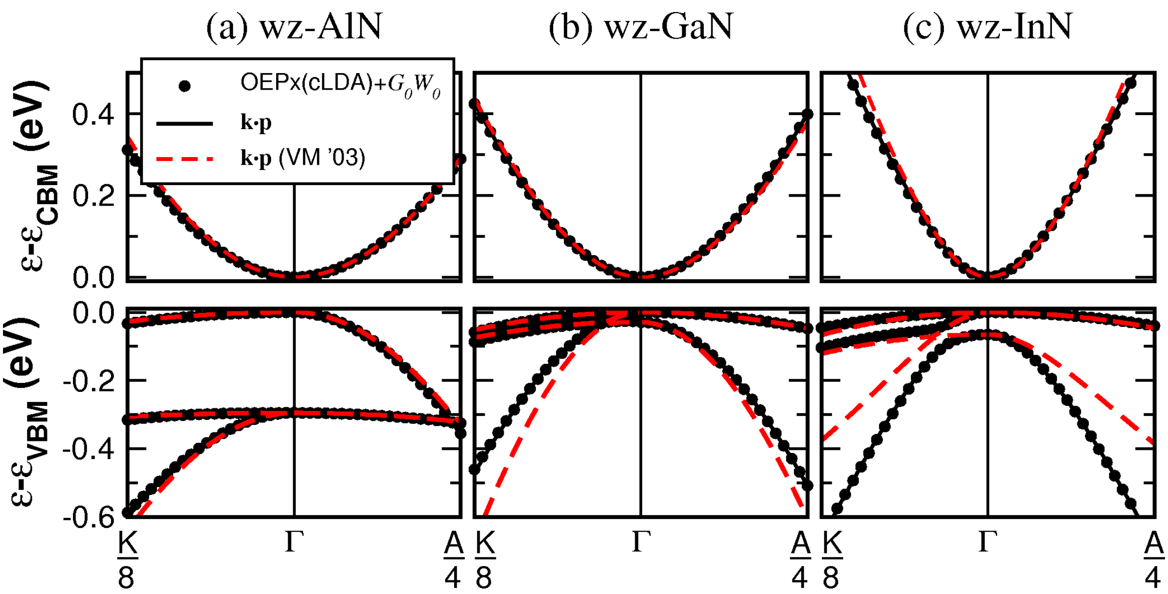

Figure 4.1: Band structure of wz-AlN (a), wz-GaN (b), and wz-InN (c) in the vicinity of Γ. The graphs show the G_0W_0 band structure (black circles), the corresponding $\mathbf{k}\cdot\mathbf{p}$ band structure (black solid lines), and the $\mathbf{k}\cdot\mathbf{p}$ band structure using the parameters recommended by Vurgaftman and Meyer[61;114] (VM '03) (red dashed lines).

materials are accurately described by the $\mathbf{k}\cdot\mathbf{p}$-method within the chosen $\mathbf{k}$-ranges. Additionally, the $\mathbf{k}\cdot\mathbf{p}$ band structures based on the parameters recommended by Vurgaftman and Meyer[61;114] (VM '03) are shown (red dashed lines). As alluded to before, their recommendations are based on available experimental data and selected theoretical values, representing the state-of-the-art parameters up until the year of compilation (2003). The parameters will also be compared to more recent experimentally derived parameters (see Tab. 4.3).

4.1.1 Comparison to Experimental Values

For the comparison of the theoretical and experimental effective hole masses two points regarding the relation between the valence-band (VB) parameters A_i and the effective hole masses in wurtzite crystals have to be emphasized: (i) Two different sets of equations connecting the effective hole masses to the A_i parameters are used in the literature. Reference 73 lists both; one is labeled "Near the band edge ($k \rightarrow 0$)" and the other "Far away from the band edge (k is large)". The latter is widely used to calculate the effective hole masses.[124–127] However, the experimentally relevant effective masses are those close to Γ. Thus, throughout this thesis the "Near the band edge" equations are used (see Appendix C). Quoted values differ from the original publications in cases where the original work uses the "Far away from the band edge" equations. (ii)

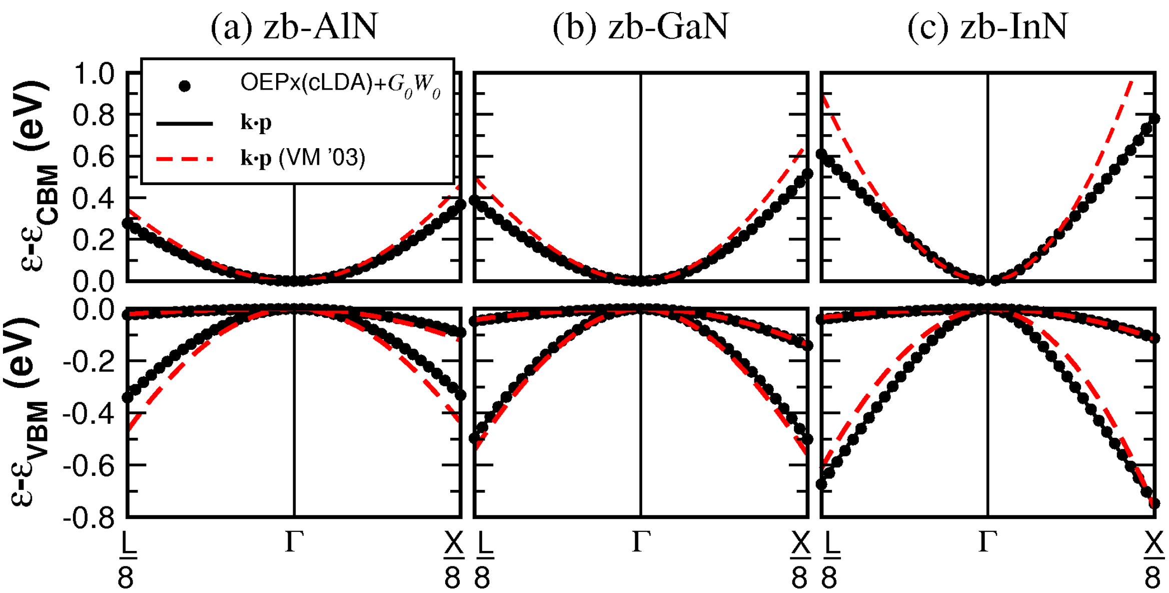

Figure 4.2: Band structure of zb-AlN (a), zb-GaN (b), and zb-InN (c) in the vicinity of Γ. The graphs show the G_0W_0 band structure (black circles), the corresponding $\mathbf{k}\cdot\mathbf{p}$ band structure (black solid lines), and the $\mathbf{k}\cdot\mathbf{p}$ band structure using the parameters recommended by Vurgaftman and Meyer[61;114] (VM '03) (red dashed lines).

The Luttinger-like parameters, A_i, are independent of the spin-orbit and crystal-field interaction parameters Δ_{SO} and Δ_{CR}; the effective hole masses, in contrast, differ for different Δ_{SO} and Δ_{CR} parameters. Only the A-band (C-band in AlN) hole masses can be calculated from the Luttinger-like parameters alone. All other hole masses additionally depend on the choice of the spin-orbit and crystal-field splitting energies.[73] Thus, effective B- and C-band (A- and B-band in AlN) hole masses derived from different sets of Luttinger-like parameters are comparable only if the same Δ_{SO} and Δ_{CR} values are assumed.

The available experimental values for the wurtzite phases are listed in Tab. 4.3. For the thermodynamically metastable zinc-blende phases of GaN, AlN, and InN hardly any experimental reports on their band dispersion parameters are available so far. Therefore, the discussion will be restricted to the wurtzite phases, for which experimental data on, at least, the effective electron masses are available. For wz-InN also E_P has been determined, by fitting a simplified $\mathbf{k}\cdot\mathbf{p}$-Hamiltonian to the experimental data.[120;121] For wz-GaN, values for E_P[116;117] and the effective hole masses are available (see Tab. 4.3).

Wurtzite GaN. The G_0W_0 effective electron masses in wz-GaN ($m_e^{\parallel} = 0.19\,m_0$, $m_e^{\perp} = 0.21\,m_0$) are in very good agreement with experimental values, which scatter around $m_e = 0.20\,m_0$.[86]

	wurtzite phases				zinc-blende phases		
param.	AlN	GaN	InN	param.	AlN	GaN	InN
$m_e^{\parallel}$	0.322	0.186	0.065	$m_e(\Gamma)$	0.316	0.193	0.054
$m_e^{\perp}$	0.329	0.209	0.068	γ_1	1.450	2.506	6.817
A_1	-3.991	-5.947	-15.803	γ_2	0.349	0.636	2.810
A_2	-0.311	-0.528	-0.497	γ_3	0.597	0.977	3.121
A_3	3.671	5.414	15.251	$m_{hh}^{[001]}$	1.330	0.810	0.835
A_4	-1.147	-2.512	-7.151	$m_{hh}^{[110]}$	2.634	1.384	1.368
A_5	-1.329	-2.510	-7.060	$m_{hh}^{[111]}$	3.912	1.812	1.738
A_6	-1.952	-3.202	-10.078	$m_{lh}^{[001]}$	0.466	0.265	0.080
A_7 (eVÅ)	0.026	0.046	0.175	$m_{lh}^{[110]}$	0.397	0.233	0.078
$E_P^{\parallel}$ (eV)	16.972	17.292	8.742	$m_{lh}^{[111]}$	0.378	0.224	0.077
$E_P^{\perp}$ (eV)	18.165	16.265	8.809	E_P (eV)	23.844	16.861	11.373

Table 4.2: Band parameters for the wurtzite (*left*) and zinc-blende (*right*) phases of GaN, InN, and AlN derived from the G_0W_0 band structures. The effective hole masses for the *HH* and *LH* band of the zinc-blende phases have been calculated from the Luttinger parameters. (see appendix C)

However, the present calculations predict an anisotropy of the electron masses of about 10 %, which is larger than values found experimentally ($< 1\,\%$ - $6\,\%$[128–130]). The E_P values of 17.3 eV and 16.3 eV support those obtained by Rodina and Meyer[116] (≈ 18.3 eV and ≈ 17.3 eV), rather than a larger value of $E_P \approx 19.8$ eV reported recently by Shokhovets *et al.*[117]

A detailed analysis of the effective hole masses has been presented by Rodina *et al.*[118] Note, that only the *A*-band masses in their work have been extracted directly from experimental data. All other effective hole masses have been calculated from the *A*-band effective masses and the spin-orbit and crystal-field splitting energies within the quasi-cubic approximation. The effective *A*-band masses derived here ($m_A^{\parallel} = 1.88\,m_0$ and $m_A^{\perp} = 0.33\,m_0$) agree very well with the experimental values derived by Rodina *et al.* ($m_A^{\parallel} = 1.76\,m_0$ and $m_A^{\perp} = 0.35\,m_0$). Adopting their values for the spin-orbit and crystal-field splitting parameters ($\Delta_{SO} = 0.019$ eV, $\Delta_{CR} = 0.010$ eV), also good agreement for the *B*- and *C*-band masses is found (see Tab. 4.3).

Wurtzite AlN. The available experimental data on the band dispersion of wz-AlN are limited to the effective electron mass, which has been determined to be in the range of 0.29 to $0.45\,m_0$.[115] The G_0W_0 values of $m_e^{\parallel} = 0.32\,m_0$ and $m_e^{\perp} = 0.33\,m_0$ fall within this range.

	param.	G_0W_0 (recommended)	exp.	VM '03[61]
AlN	$m_\mathrm{e}^\parallel$	0.32	0.29-0.45[115]	0.32
	$m_\mathrm{e}^\perp$	0.33	0.29-0.45[115]	0.30
	$E_\mathrm{P}^\parallel$ (eV)	16.97	-	-
	$E_\mathrm{P}^\perp$ (eV)	18.17	-	-
	$m_C^\parallel$	3.13	-	3.57
	$m_C^\perp$	0.69	-	0.59
GaN	$m_\mathrm{e}^\parallel$	0.19	0.20[86]	0.20
	$m_\mathrm{e}^\perp$	0.21	0.20[86]	0.20
	$E_\mathrm{P}^\parallel$ (eV)	17.29	17.8-18.7[116], 19.8[117]	-
	$E_\mathrm{P}^\perp$ (eV)	16.27	16.9-17.8[116], 19.8[117]	-
	$m_A^\parallel$	1.88	1.76[118]	1.89
	$m_A^\perp$	0.33	0.35[118]	0.26
	$m_B^\parallel$	0.37[119]	0.42[118]	-
	$m_B^\perp$	0.49[119]	0.51[118]	-
	$m_C^\parallel$	0.26[119]	0.30[118]	-
	$m_C^\perp$	0.65[119]	0.68[118]	-
InN	$m_\mathrm{e}^\parallel$	0.065	0.07[120], 0.05[121], 0.04[122], 0.085[123]	0.07
	$m_\mathrm{e}^\perp$	0.068	0.07[120], 0.05[121], 0.05[122], 0.085[123]	0.07
	$E_\mathrm{P}^\parallel$ (eV)	8.74	10[120], 9.7[121]	-
	$E_\mathrm{P}^\perp$ (eV)	8.81	10[120], 9.7[121]	-
	$m_A^\parallel$	1.81	-	1.56
	$m_A^\perp$	0.13	-	0.17

Table 4.3: Band parameters of wurtzite group-III nitrides: Comparison to parameters from the literature. Listed are experimental values and the parameters recommended by Vurgaftman and Meyer[61] (VM '03).

Wurtzite InN. Experimentally derived effective electron masses of wz-InN scatter over a wide range (see Tab. 4.3). The most reliable seem to be the ones reported by Wu *et al.*[120] and Fu *et al.*,[121] since they explicitly account for the high carrier concentration of their samples and the non-parabolicity of the conduction band in their analysis. Their effective electron masses of $0.05\,m_0$[121] and $0.07\,m_0$[120] in conjunction with values for E_P of 9.7 eV and 10 eV, respectively, are in good agreement with those derived from the G_0W_0 calculations ($m_\mathrm{e}^{\|} = 0.065\,m_0$, $m_\mathrm{e}^{\perp} = 0.068\,m_0$ and $E_\mathrm{P}^{\|} = 8.7\,\mathrm{eV}$, $E_\mathrm{P}^{\perp} = 8.8\,\mathrm{eV}$), which also predict an anisotropy of the electron masses of about 5 %. A similar anisotropy has been reported by Hofmann *et al.*[122] (see Tab.4.3).

The parameters derived from the G_0W_0 calculations match all available experimental data to good accuracy and, therefore, provide reliable predictions for all parameters which have not been determined experimentally so far.

4.1.2 Comparison to the Parameters Recommended by Vurgaftman and Meyer

For none of the group-III nitrides a complete set of band parameters has so far been derived from experimental values alone. Therefore, Vurgaftman and Meyer[61] (VM ’03) have compiled parameter sets comprising experimental and the most reliable theoretical values in the year 2003.

For wz-GaN, VM’03 recommend the experimental value of the effective electron masses of $m_\mathrm{e}^{\|} = m_\mathrm{e}^{\perp} = 0.20\,m_0$ and Luttinger-like parameters derived from calculation using the empirical-pseudopotential method (EPM) by Ren *et al.*[126], which yield effective hole masses in good agreement with experimental and the G_0W_0 data (see Tab. 4.3). The parameter set yields a band structure that agrees well with the G_0W_0 band structure for the conduction band and the two top VBs (see Fig. 4.1). It deviates, however, for the C VB (the third valence band counted from the valence band maximum), where the curvatures in the EPM band structure are too large.

Of all the compounds and phases discussed here wz-GaN is the best characterized experimentally. The good agreement between our quasiparticle band structures and those based on the parameter set recommended by VM’03 proves the quality of our G_0W_0 band structures.

For wz-AlN the effective electron masses recommended by VM’03 are the averages over several theoretical values; the recommended VB parameters are theoretical values by Kim *et al.*[131] derived from LDA calculations. These parameters yield a band structure which is in good overall agreement with the G_0W_0 band structure (see Fig. 4.1a). The anisotropy of the effective electron masses, however, has the opposite sign, similar to other LDA calculations.[96]

For wz-InN, VM’03 recommend the experimental effective electron masses by Wu *et al.*[120]

($m_\mathrm{e}^{\|} = m_\mathrm{e}^{\perp} = 0.07\,m_0$) and the EPM values from Pugh *et al.*[127] for the VB. The pseudo potentials used by Pugh *et al.* were designed to reproduce their LDA calculations, which had been "scissor corrected" to the incorrect band gap of 2.0 eV. These parameters are therefore to no avail from today's perspective.

The compilation by Vurgaftman and Meyer is a thorough revision of band parameters for the group-III nitrides available in the year 2003. However, parts of the parameters have by now been superseded, for instance by the $\mathbf{k}\cdot\mathbf{p}$ parameters derived in the present work. However, Vurgaftman and Meyer also provide recommendations for a number of parameters not addressed in this chapter. For the quantum dot electronic structure simulations in the following chapters, therefore, the parameters by Vurgaftman and Meyer will be complemented with the $\mathbf{k}\cdot\mathbf{p}$ parameters derived here.

4.2 Summary

In this chapter a consistent set of $\mathbf{k}\cdot\mathbf{p}$ band parameters for the wurtzite and zinc-blende phases of GaN, AlN, and InN has been derived from first-principle band-structure calculations within the G_0W_0 approximation. It has been demonstrated that the band parameters are in very good agreement with available experimental data, proving the reliability of the method. Thus, it was possible to derive reliable values for parameters which have not yet been determined experimentally, such as, e.g., the band parameters of the zinc-blende phases of GaN, AlN, and InN and the E_p and VB parameters of wurtzite phases. These parameters are essential for understanding the physics of these materials and accurate modelling of nitride-based devices and nanostructures.

The parameters derived here (complemented with additional material parameter from the literature as described in appendix A) present the basis for the quantum-dot electronic structure calculations presented in Chaps. 6 and 7.

5 Valence-band Structure of Strained Group-III Nitrides

To understand the electronic properties of nitride-based QDs it is important to have a detailed understanding of the valence-band (VB) structure of the involved materials. In this work QDs with wurtzite crystal structure are considered. Therefore, the VB structure of the wurtzite phases of the group-III nitrides under different forms of strain shall be analyzed here in detail. GaN will serve as an example where quantitative results are presented, but the considerations can be fully transfered to wurtzite InN or InGaN. AlN is an exception, because the crystal-field splitting (see below) is negative in this material. First, the VB structure under symmetric biaxial strain in the basal plane, typical for quantum dots (QDs) or quantum wells (QWs) grown on the *c*-plane, will be discussed in Sec. 5.1. Thereafter, an additional strain anisotropy in the basal plane will be considered in Sec. 5.2. The later analysis is of particular importance for the electronic structure of QDs with low symmetry of the confinement potential in the basal plane due to, e.g., an elongated shape, an inhomogeneous composition profile, or externally induced strain anisotropy. The results of this analysis will be used in Secs. 6.5 and 7.4 to interpret the results of the QD electronic structure calculations.

5.1 Group-III Nitrides under Biaxial Strain

Similar to the “heavy hole, light hole, and split-off” bands in zinc-blende III-V semiconductors, wurtzite III-V or II-VI semiconductors also have three different VBs energetically close to the fundamental band gap. These bands are labeled *A*, *B*, and *C* in wurtzite crystals, where *A* denotes the highest VB. The energy separation between the bands is, in unstrained crystals, determined by the spin-orbit and crystal-field splitting energies Δ_{SO} and Δ_{CR}. The energies (with an arbitrary

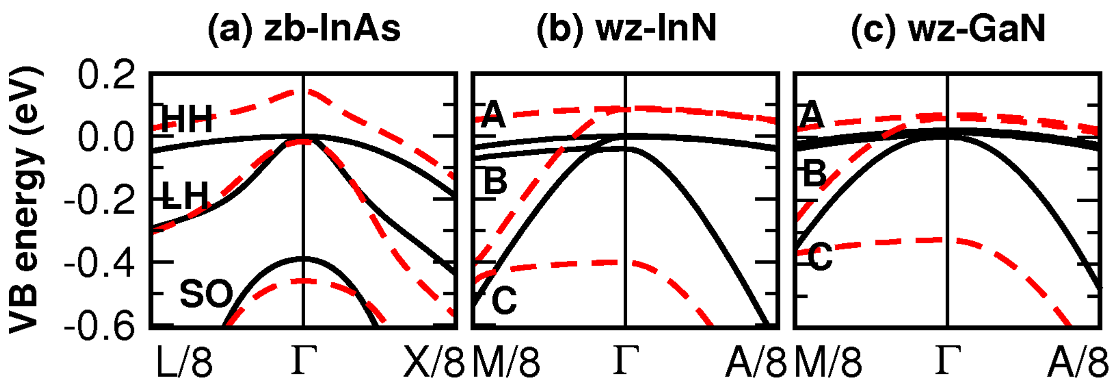

Figure 5.1: Calculated bulk $\mathbf{k}\cdot\mathbf{p}$ VB structure of (a) zb-InAs, (b) wz-InN, and (c) wz-GaN; unstrained (black solid lines) and under compressive biaxial strain (-3 %) in the basal plane with elastic relaxation along [0001] ([001] in the case of InAs) direction (red dashed lines). The splitting between the *A* and *B* VB at Γ is ≈ 3 meV in strained and unstrained InN and 11 meV (5 meV) in strained (unstrained) GaN. (In hexagonal crystals the $\mathbf{k}$ points A and M correspond to $\mathbf{k} = \sqrt{2}\pi/(\sqrt{3}a_0)\cdot(01\bar{1}0)$ and $\mathbf{k} = \pi/c_0\cdot(0001)$, respectively.)

offset) of the *A*, *B*, and *C* VBs at Γ are given by[73]

$$
\begin{aligned}
E_A(\mathbf{k}=0) &= \Delta_{CR} + \frac{\Delta_{SO}}{3} \quad , \\
E_B(\mathbf{k}=0) &= \frac{\Delta_{CR} + \frac{\Delta_{SO}}{3}}{2} + \sqrt{\left(\frac{\Delta_{CR} - \frac{\Delta_{SO}}{3}}{2}\right)^2 + 2\left(\frac{\Delta_{SO}}{3}\right)^2} \quad , \\
E_C(\mathbf{k}=0) &= \frac{\Delta_{CR} + \frac{\Delta_{SO}}{3}}{2} - \sqrt{\left(\frac{\Delta_{CR} - \frac{\Delta_{SO}}{3}}{2}\right)^2 + 2\left(\frac{\Delta_{SO}}{3}\right)^2} \quad .
\end{aligned}
\tag{5.1}
$$

Note that Δ_{CR} is negative in wz-AlN. Therefore, the band labeled "*C*" in Eqs. 5.1 is the uppermost VB and, consequently, would have to be labeled "*A*" in this material. However, to preserve consistency with the other materials, I will stick to the labeling scheme of Eqs. 5.1 throughout this work. The splittings between the different VBs are affected by (non-hydrostatic) strain. The shifts of the band edges for specific strain situations can be generally derived from equations given in Chap. 3 or in Ref. 73. Here, only a qualitative discussion of strain effects relevant in the considered systems will be given.

In quantum dots or wells with larger lattice constants than the surrounding matrix, such as GaN/AlN, In$_x$Ga$_{1\text{-}x}$N/GaN, or InAs/GaAs the dominant strain components are compressive hydrostatic strain and compressive biaxial strain in the growth plane. The compressive hydrostatic strain simply widens the band gap. The biaxial strain modifies the VB structure: In zinc-blende

InAs QDs it leads to a splitting of the two top VBs—the heavy hole (*HH*) and the light hole (*LH*) band—resulting in a clear separation of all three VBs (*HH*, *LH*, and split-off band) [Fig. 5.1(a)]. In wurtzite InN and wurtzite GaN, by contrast, the already existing splitting between the two top VBs—the *A* and the *B* band—does not significantly increase if similar strain is applied [Fig. 5.1(b,c)]. Note, that this is true only for *compressive* biaxial strain in the basal plane. Moreover, the *A* and the *B* bands show a similar dispersion along the *z*-axis, which is the direction of the strongest confinement in [0001]-grown heterostructures. Therefore, in contrast to InAs/GaAs QDs, the energetically highest confined hole states in the QDs considered in this work are formed by two different bands, the *A* and the *B* band. This strain field is realistic for QWs or QDs grown on the *c*-plane.

5.2 Anisotropic Strain in the Basal Plane

In order to gain further insight in the character of the hole states it is useful to expand the three VB states at Γ, $|A\rangle$, $|B\rangle$, $|C\rangle$, into another set of basis states: $|P_\mathrm{x}\rangle$, $|P_\mathrm{y}\rangle$, and $|P_\mathrm{z}\rangle$. This basis set is widely used for $\mathbf{k}\cdot\mathbf{p}$ calculations (also in the present work), because the optical matrix elements of the states $|P_\mathrm{i}\rangle$ with the conduction-band state at Γ, $|S\rangle$, are simply

$$\langle S|\hat{\mathbf{p}}_\mathrm{i}|P_\mathrm{j}\rangle = \delta_\mathrm{ij}P_\mathrm{i} \quad , \tag{5.2}$$

where P_i are material constants. This is favourable for the implementation of a $\mathbf{k}\cdot\mathbf{p}$ method in rectangular coordinates, but can also be helpful for the analysis of the band edges and, later on, confined hole states in QDs. The $|A\rangle$, $|B\rangle$, and $|C\rangle$ states expressed in this basis are given by:[118]

$$\begin{aligned}
|A\uparrow\rangle &= \frac{1}{\sqrt{2}}|(P_\mathrm{x}+iP_\mathrm{y})\uparrow\rangle \quad ,\\
|A\downarrow\rangle &= \frac{1}{\sqrt{2}}|(P_\mathrm{x}-iP_\mathrm{y})\downarrow\rangle \quad ,\\
|B\uparrow\rangle &= \frac{ia}{\sqrt{2}}|(P_\mathrm{x}+iP_\mathrm{y})\downarrow\rangle - ib|P_\mathrm{z}\uparrow\rangle \quad ,\\
|B\downarrow\rangle &= \frac{a}{\sqrt{2}}|(P_\mathrm{x}-iP_\mathrm{y})\uparrow\rangle + b|P_\mathrm{z}\downarrow\rangle \quad ,\\
|C\uparrow\rangle &= \frac{ib}{\sqrt{2}}|(P_\mathrm{x}+iP_\mathrm{y})\downarrow\rangle + ia|P_\mathrm{z}\uparrow\rangle \quad ,\\
|C\downarrow\rangle &= \frac{b}{\sqrt{2}}|(P_\mathrm{x}-iP_\mathrm{y})\uparrow\rangle - a|P_\mathrm{z}\downarrow\rangle \quad ,
\end{aligned} \tag{5.3}$$

where a and b are defined by

$$\begin{aligned} a &= \frac{1}{\sqrt{x^2+1}} \\ b &= \frac{x}{\sqrt{x^2+1}} \\ x &= \frac{-(3\Delta_{\text{CR}}-\Delta_{\text{SO}})+\sqrt{(3\Delta_{\text{CR}}-\Delta_{\text{SO}})^2+8\Delta_{\text{SO}}^2}}{2\sqrt{2}\Delta_{\text{SO}}} \quad . \end{aligned} \tag{5.4}$$

The nanostructures considered in the present work, GaN/AlN and $\text{In}_\text{x}\text{Ga}_{\text{1-x}}\text{N}$/GaN QDs (and QWs in the present example), are compressively biaxially strained in the basal plane, because they are grown along the [0001]-axis on substrate material with a larger lattice constant a_0. In this case Eqs. 5.3 simplify in the following way:[73;118]

$$\begin{aligned} |A\uparrow\rangle &= \frac{1}{\sqrt{2}}|(P_\text{x}+iP_\text{y})\uparrow\rangle \quad , \\ |A\downarrow\rangle &= \frac{1}{\sqrt{2}}|(P_\text{x}-iP_\text{y})\downarrow\rangle \quad , \\ |\tilde{B}\uparrow\rangle &= \frac{i}{\sqrt{2}}|(P_\text{x}+iP_\text{y})\downarrow\rangle \quad , \\ |\tilde{B}\downarrow\rangle &= \frac{1}{\sqrt{2}}|(P_\text{x}-iP_\text{y})\uparrow\rangle \quad , \\ |\tilde{C}\uparrow\rangle &= i|P_\text{z}\uparrow\rangle \quad , \\ |\tilde{C}\downarrow\rangle &= -|P_\text{z}\downarrow\rangle \quad . \end{aligned} \tag{5.5}$$

The characters of these states determine the polarization of light emitted or absorbed by excitons that are formed including these hole states (the involved electron state is always of $|S\rangle$ character). The optical matrix element $\langle S|\hat{p}|P_\text{x}\rangle$ is polarized in x-direction (the $[11\bar{2}0]$-direction), while the matrix elements $\langle S|\hat{p}|P_\text{y}\rangle$ and $\langle S|\hat{p}|P_\text{z}\rangle$ are polarized in y- ($[1\bar{1}00]$) and z- ([0001]) direction, respectively.

In QDs that are asymmetric in the basal plane the strain-field will also be asymmetric in the basal plane. The effects of such a strain field on the band structure is shown in Fig. 5.2: Figure 5.2 (upper panel) shows, once again, the VB structure of wurtzite GaN, but this time along the x and y directions. The dispersions along both directions are similar. This does not change under symmetric biaxial strain in the basal plane [Fig. 5.2 (center panel)], but the bands split and their characters change in the ways described in the previous section. If now, in addition, the biaxial strain is unsymmetrical in the basal plane [Fig. 5.2 (lower panel)], the splitting between

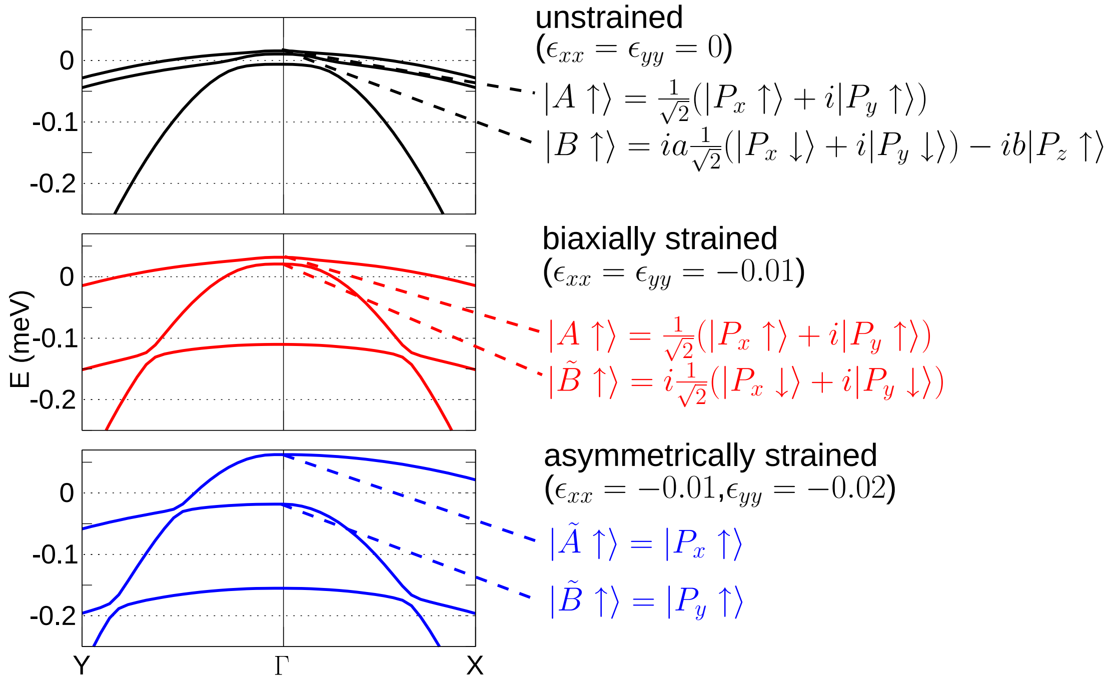

Figure 5.2: Valence band structure of bulk GaN in the vicinity of Γ. *Upper panel*: unstrained. *Center*: under symmetric biaxial strain in the basal plane, typical for *c*-plane QDs. *Lower*: With an additional strain anisotropy in the basal plane, e.g., in asymmetric QDs. The splitting between the two top bands increases and their characters change from *A*- and *B*-like to P_x- and P_y-like.

the *A* and the *B* band increases and their dispersions are unsymmetrical. Even more important, the band-edge states change their character again: the uppermost band (the *A*-band) turns to P_x character, the direction of least compressive strain, and the next band (the *B* band) to P_y character. This strain field, therefore, leads to a linear polarization of light emitted (or absorbed) by *A* and *B* excitons in orthogonal directions. This effect can potentially be exploited for applications where polarized light emission is desired. Examples are single-photon emitter for quantum key distribution or back lights for liquid-crystal displays.

5.3 Summary

In this chapter the VB structure of wurtzite group-III nitrides under different forms of strain has been analyzed. It has been shown, that the energy separation between *A*- and *B* VB does not increase under biaxial strain in the basal plane, in contrast to other QD materials like In(Ga)As. It will be shown in the following chapters (6 and 7) that this results in confined *A- and B*-band hole states in nitride QDs grown on the *c*-plane. An additional anisotropy of the strain in the basal plane leads to a linear polarization of the interband transitions between conduction and valence band. *A*- and *B*-band transitions are polarized in orthogonal directions. This analysis will be used in Secs. 6.5 and 7.4 to interpret linear polarization phenomena in the spectra of single QDs.

6 InGaN/GaN Quantum Dots

The $In_xGa_{1\text{-}x}N/GaN$ system has evolved into one of the most important material systems for solid-state light emitters. Applications include green and blue light emitting diodes,[1;2] laser diodes,[3;4] and white light emitters.[5–7] As already alluded to in Chap. 1, $In_xGa_{1\text{-}x}N/GaN$ quantum dots (QDs) and QD-like localization centers have always played an important role in this research field. The electronic structure of $In_xGa_{1\text{-}x}N/GaN$ QDs, however, is yet poorly understood. In this chapter the electronic and optical properties of $In_xGa_{1\text{-}x}N/GaN$ QDs will be investigated theoretically. The calculations will be used to interpret a number of experimental results, which will also be detailed in the following sections.

In Sec. 6.1 the model structures used in the calculation will be described and motivated based on experimental observations. Thereafter, a number of important general features of the electronic structure of InGaN QDs will be discussed in Sec. 6.2. In the subsequent sections calculations will be presented that were performed with the aim to understand certain experimental findings: In Sec. 6.3 the dependence of the excitonic transitions energies on structural properties of the QDs will be compared to experimental luminescence data of the $In_xGa_{1\text{-}x}N/GaN$ QDs. The radiative lifetimes of excitons confined in the QDs will be investigated in Sec. 6.4. The theoretical results will be compared to an analysis of the multi-exponential decay of the ensemble photoluminescence (PL) signal of the $In_xGa_{1\text{-}x}N/GaN$ QDs. Another experimentally observed phenomenon will be addressed in Sec. 6.5: The linear polarization of single-QD emission lines observed in single-QD cathodoluminescence (CL) will be traced back to recombinations of excitonic complexes either via *A* or *B* valence band (VB) states.

6.1 Model Quantum Dots

Despite the fact that many of the results presented in the following sections are of general character and are therefore, at least qualitatively, applicable to all $In_xGa_{1\text{-}x}N$ QDs, the model structures

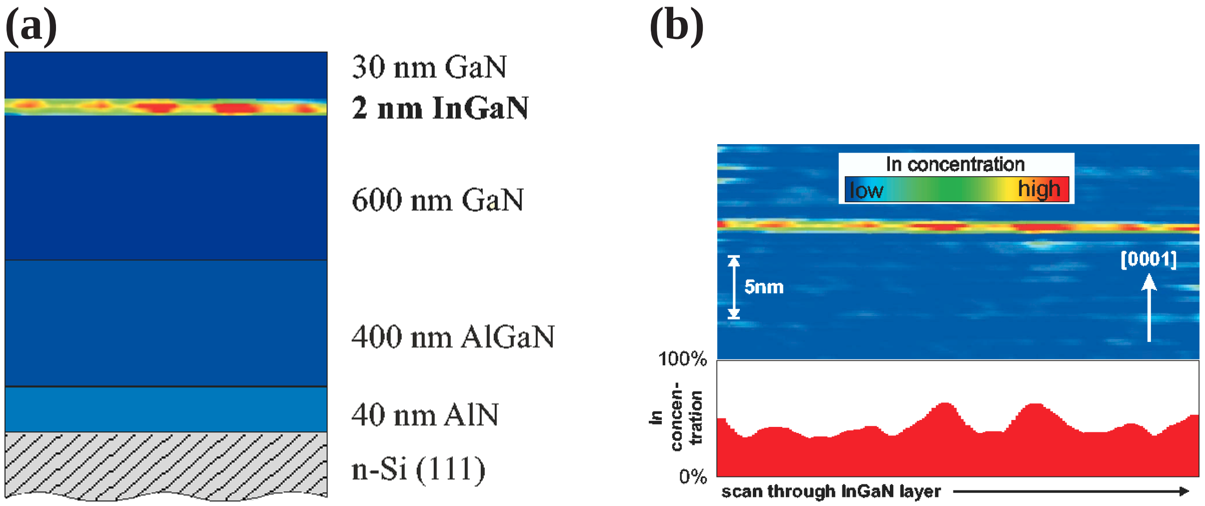

Figure 6.1: *(a)* Schematic drawing of the structure of the $In_xGa_{1-x}N$/GaN-QD sample investigated in the experiments. *(b)* X-TEM/DALI-image of the active layer. The theoretical model QDs have been design to resemble the localization centers in the active layer of this sample.

used in the present work are designed to reproduced a specific series of samples that has been grown at Technische Universität Berlin. These samples were grown on Si(111) substrate by low-pressure metal-organic chemical vapor deposition (MOCVD) using a horizontal AIX200 RF reactor. An AlAs layer was grown and subsequently converted to AlN as a nucleation surface.[132] In the following step an $Al_{0.05}Ga_{0.95}N$/GaN buffer layer was grown at T=1150 °C up to a total thickness of 1 μm. The $In_xGa_{1-x}N$ layer was grown at 800 °C with a nominal thickness of 2 nm using trimethylgallium, trimethylindium, and ammonia as precursors. The QDs are formed by alloy fluctuations in the $In_xGa_{1-x}N$-layer.[24] The growth was finished with a 20 nm GaN cap layer grown during the heat-up phase to 1100 °C. The sample structure is schematically shown in Fig. 6.1(a). Figure 6.1(b) shows the results of the investigation by cross-sectional transition electron microscopy (X-TEM) in conjunction with the digital-analysis-of-lattice-images (DALI)[133] technique, where the inter-atomic distances observed in X-TEM are mapped to an indium concentration profile. Unfortunately, a quantitative determination of indium concentrations or the exact shape of the QDs from these images is not possible. Still, the composition fluctuations are clearly visible. The model structures used in this work are derived not only from these structure images and related growth information,[24;134;135] but also from more general knowledge about composition fluctuations in thin $In_xGa_{1-x}N$-layers (see, e.g., Ref. 44). A broad distribution of QD sizes, shapes, and indium concentrations can be generally expected. Due to the QDs' growth mode, based on phase separation mechanisms in thin layers, their shapes differ significantly from the shape of, e.g., InAs/GaAs QDs. Moreover, no wetting layer is present, but the QDs are

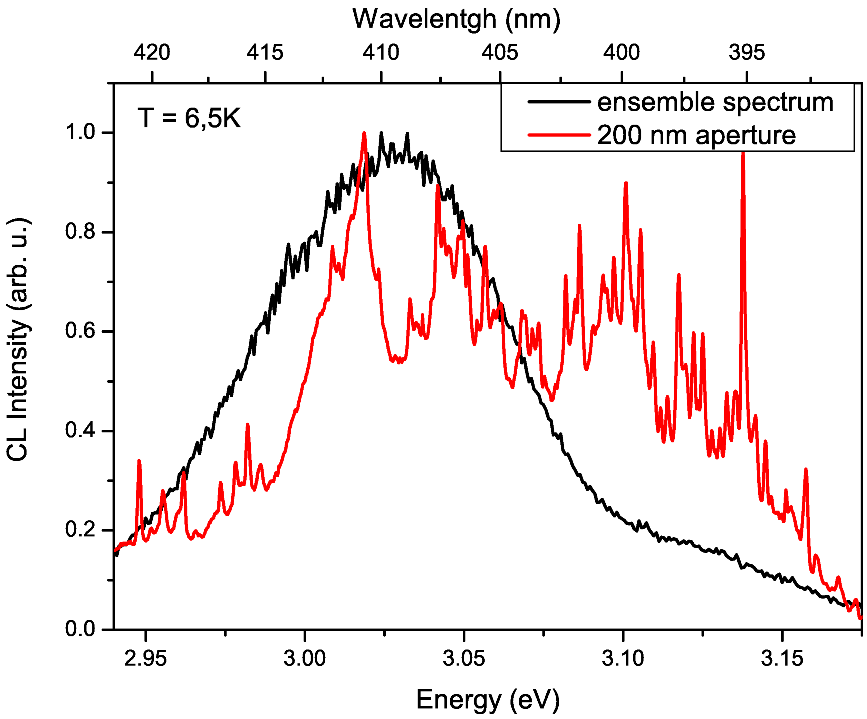

Figure 6.2: The CL spectrum of the entire $In_xGa_{1-x}N$/Gan QD ensemble (back line) has its maximum slightly above 3 eV and a FWHM of ≈ 80 meV. Sharp emission lines of discrete QD states were observed in spatially resolved measurements (red line) from 2.8 to 3.2 eV indicating QD origin of the entire emission.

embedded in a quantum well (QW).

The sample luminescence has been investigated by CL[24;29] and PL[25] spectroscopy. In both cases measurements on the ensemble and on single QDs have been performed. An example CL spectrum is shown in Fig. 6.2. The emission peak of the entire $In_xGa_{1-x}N$-layer has its maximum slightly above 3 eV and a full width at half maximum (FWHM) of about 80 meV. Sharp emission lines of discrete QD states were observed in spatially resolved measurements from 2.8 to 3.2 eV indicating QD origin of the entire emission (red line in Fig. 6.2).[24;25;29]

Due to their particular growth mode, the shape of the $In_xGa_{1-x}N$/GaN QDs differs significantly from the shape of QDs grown in Stranski-Krastanow or Volmer-Weber growth mode, e.g., GaN/AlN QDs (cf Chap. 7). In this work an ellipsoid has been chosen as the shape of the model $In_xGa_{1-x}N$/GaN QDs, which agrees with the experimental findings and does not lower the confinement symmetry more than justified by the structure images. The model QDs are shown schematically in Fig. 6.3. The ellipsoids have a height h and lateral diameter d and are embedded in a 2 nm thick $In_xGa_{1-x}N$ QW with indium concentration x_W. The indium concentration inside

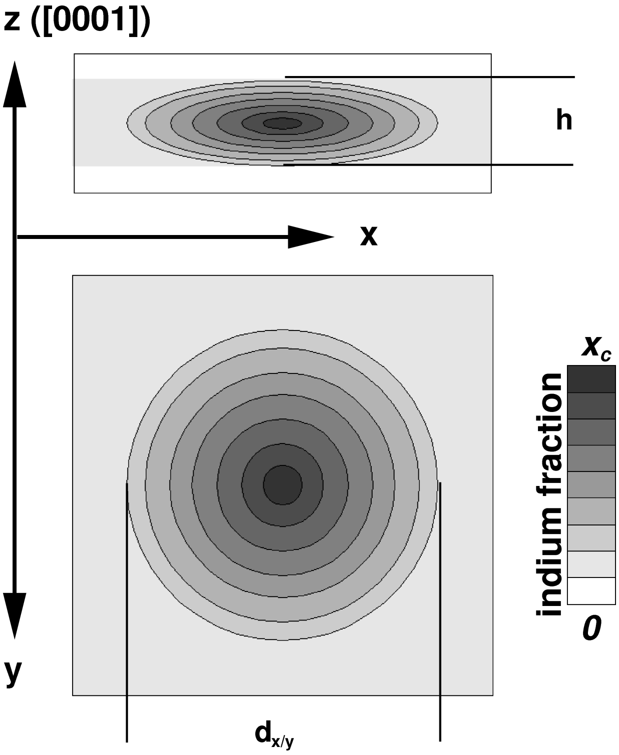

Figure 6.3: Schematic drawing of the model $In_xGa_{1-x}N$ QDs used for the calculations. Ellipsoids with a height of h and lateral diameter of $d_x = d_y$. The indium concentration inside the QDs is modeled with a linear gradient from the maximum indium fraction x_c at the center of the QDs to x_w at their border. The QDs are embedded in an $In_{x_w}Ga_{1-x_w}N$ layer with a height of 2 nm. The layer itself is embedded in a matrix of pure GaN.

the QDs increases linearly from the indium fraction of the surrounding QW (x_w) to the maximum indium concentration x_c at the QD center. Starting with a QD with a height of $h = 2$ nm, a lateral diameter of $d = 5.2$ nm, and indium concentration of $x_c = 0.5$, the influences of three different structural parameters have been investigated: The QD height (with h varying between 1.2 and 2.8 nm), the lateral diameter (with d varying between 2.8 and 7.6 nm), and the indium concentration inside the QD (x_c between 0.3 and 0.6). All three series have been calculated with the QDs embedded in an $In_{0.1}Ga_{0.9}N$ QW, in an $In_{0.05}Ga_{0.95}N$ QW, and directly in the GaN matrix, without a QW. In the last case QDs with slightly higher In concentration ($x_c = 0.7$) or slightly larger diameter ($d = 8.8$ nm), respectively, have been included in order to cover the experimentally observed energy range. Note that due to the concentration gradient inside the QDs, the average indium concentration inside the QDs x_{avg} is much lower than the maximum indium concentration of $x_c = 0.3$-0.6 (0.7) at the QD center. A maximum indium concentration of $x_c = 0.3$ corresponds to an average concentration of $x_{avg} \approx 0.08$-0.15 depending on the indium concentration in the QW ($x_w = 0.0$-0.1). An x_c of 0.6 (0.7) corresponds to $x_{avg} \approx 0.15$-0.23 (0.18-0.25). The magnitude of the deviation $\Delta x = x_{avg} - x_w \approx 0.08$-$0.15$ is in good agreement with typical values for alloy fluctuations in $In_xGa_{1-x}N$ QWs.[44]

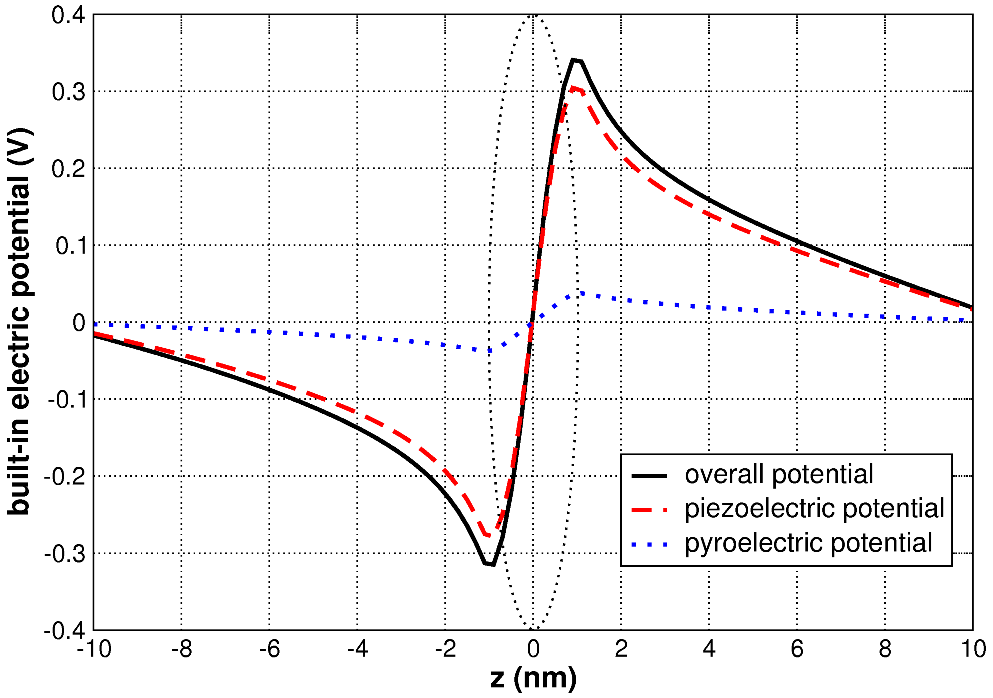

Figure 6.4: Line-scan of the built-in electric potential along the [0001] direction through the center of an $In_xGa_{1\text{-}x}N$/GaN QD. The black solid line shows the overall potential. The red dashed line and the blue dotted line show the contributions of the piezoelectric polarization and the pyroelectric polarization. The dotted ellipse indicates the position of the QD.

6.2 Electronic Structure of InGaN Quantum Dots

In this section the general features of the electronic structure of $In_xGa_{1\text{-}x}N$/GaN QDs will be discussed. One specific model QD will be used as an example for this discussion. The QD has a shape as described in Sec. 6.1, a height of $h = 2\,\mathrm{nm}$, a diameter of $d_{x/y} = 6.4\,\mathrm{nm}$, a center indium concentration of $x_c = 50\,\%$, and is embedded in an InGaN QW with $x_w = 10\,\%$. The chosen structural properties do not restrain the generality of the results.

6.2.1 Built-in Electric Fields

Figure 6.4 shows a line-scan of the built-in electric potential along the [0001] direction through the center of the QD. A large potential drop of $\approx$ 650 meV inside the QD is observed along the [0001]-direction. The potential is attractive for electrons at the upper side of the QD (i.e. positive z values in Fig. 6.4) and attractive for holes at the lower side (i.e. negative z values in Fig. 6.4).

The decomposition of the total electrostatic potential into a piezoelectric and a pyroelectric part (also shown in Fig. 6.4) shows that the large built-in electric potential is mainly caused by

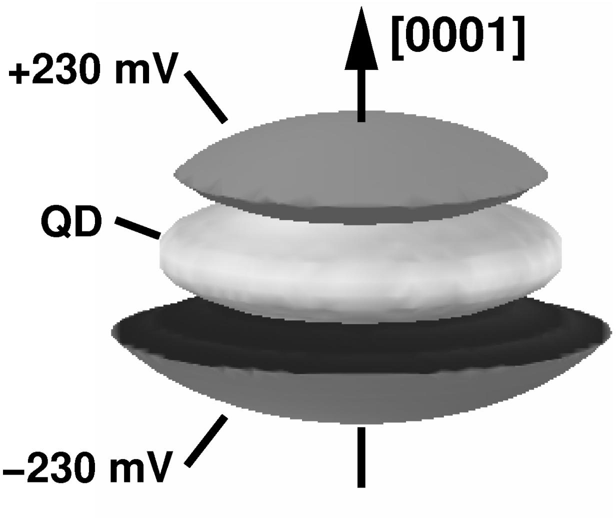

Figure 6.5: ±230 mV isosurfaces of the overall built-in electric potential. The surface of the $In_xGa_{1-x}N$/GaN QD is shown in the middle in light gray. The positive isosurface is located atop the QD, making this area attractive for electrons. The negative one is found beneath it; this area is attractive for holes.

piezoelectric effects; the contribution of the pyroelectricity is small for $In_xGa_{1-x}N$/GaN QDs. For this specific QD the piezoelectric potential is about eight times larger than the pyroelectric potential.

Figure 6.5 shows the ±230 mV iso-surfaces of the potential, illustrating its spatial distribution in all three dimensions: The symmetry of the built-in electric potential in the basal plane reproduces the symmetry of the structure. As a result of the electromechanical properties of wurtzite materials, the polarization effects do not lead to any additional symmetry lowering in the basal plane. This is an important difference to QDs in zinc-blende materials (assuming growth along [001]), where the piezoelectricity lowers the confinement symmetry in the growth plane, typically from C_{4v} (neglecting atomistic interface and strain effects here), imposed by a (truncated-)pyramidal structure, to C_{2v}.

The modifications to the confinement potential by piezoelectric and pyroelectric effects are of the same order of magnitude as the band offsets between the different materials. The built-in electric potentials in the QDs considered here cannot be regarded as (small) distortions to the confinement potential, but have to be seen as a constituting part of it.

6.2.2 Local Band-edge Profile

Figure 6.6 shows a line-scan of the local band edge profile along the z-axis through the QD center, neglecting [6.6(a)] and including [6.6(b)] the piezoelectric and pyroelectric potentials.

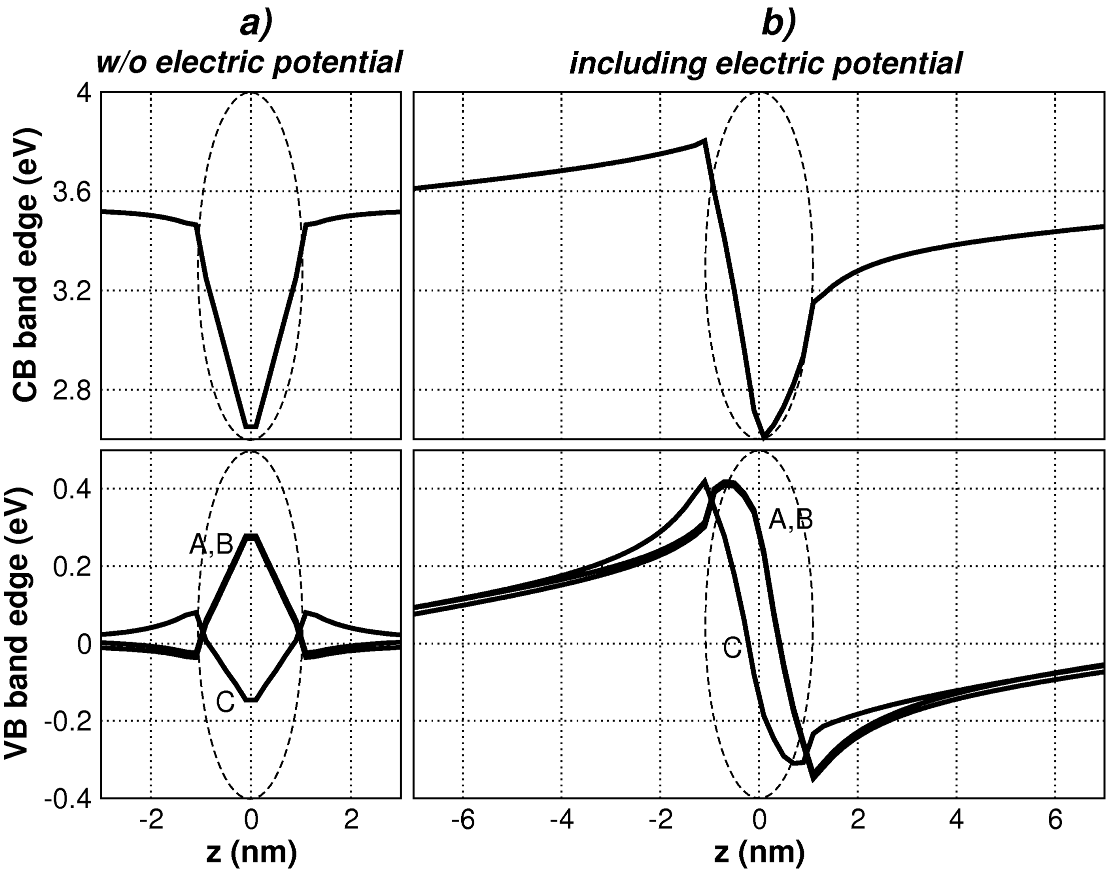

Figure 6.6: Line-scan of the local band-edge profile along the [0001] direction through the center of the $In_xGa_{1-x}N$/GaN QD. (a) without electric potentials. (b) including electric potentials. The dashed ellipses indicate the position of the QD.

Neglecting the built-in electric potentials

Due to the symmetry of the model structure the field-free local band edges are symmetric with respect to the center of the QD and the resulting confinement potential minima are in the QD center for both charge-carrier types [Fig. 6.6(a)].

The VBs show pronounced shifts, caused by the strain in the QD and its vicinity. Biaxial strain in the basal plane—always present in lattice mismatched heterostructures grown on [0001]—, does not split the $|A\rangle$ and $|B\rangle$ VBs. Both are energetically shifted in the same way: upwards by the negative biaxial strain inside the QD and downwards by the positive biaxial strain in the QD vicinity. For the $|C\rangle$ VB the biaxial strain has the opposite effect: the band energy is reduced by the negative biaxial strain inside the QD, and increased in the area surrounding the QD. Thus, the hole ground states and the first few excited hole states are expected to be mainly of $|A\rangle$- and $|B\rangle$-character.

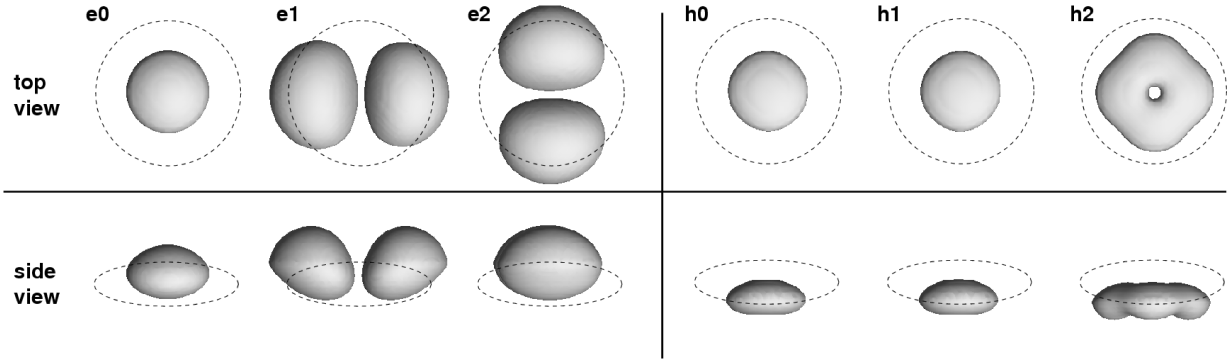

Figure 6.7: Bound single-particle states in an $\mathrm{In_xGa_{1\text{-}x}N}$/GaN QD: electron ground state (e_0), hole ground state (h_0), and the first two excited electron and hole states (e_1/e_2 and h_1/h_2). The picture shows the 65% isosurfaces of the probability density distribution $|\Psi|^2$ in top and side view. Each state is twofold spin-degenerate. The energies of the single-particle states are listed in Tab. 6.1.

Including the built-in electric potentials

The built-in electric fields cause dramatic modifications of the local band edges [Fig. 6.6(b)]. The symmetry along the [0001]-direction is broken, as the conduction band (CB) and the VBs are lifted up beneath the QD's center and lowered above it. The confinement potential is more attractive for electrons (holes) in the upper (lower) part of the QD. The band-edge profile implies a spatial separation of electron and hole states together with a redshift of the corresponding exciton transition energies compared to the field-free QD. This effect is known as the *quantum confined Stark effect (QCSE)* (cf Sec. 2.3).

Additionally, the electric fields change the projections of the hole wave functions on the different VBs. In the area beneath the QD, the $|C\rangle$ band is more attractive for the holes than the $|A\rangle$ and $|B\rangle$ band. The absolute energetic maximum of the $|C\rangle$ band (1.1 nm below the QD's center) is as high as the maximum of the $|A\rangle$ band (0.7 nm below the QD's center). This suggests an increase of the $|C\rangle$-band part of the bound hole states, caused by the electric fields.

6.2.3 Bound Single-particle States

Figure 6.7 shows the probability density distribution $|\Psi(\mathbf{r})|^2$ of the ground state and the first two excited states for electrons and holes. The corresponding single-particle energies are given in

Table 6.1: Single particle energy levels in an $In_xGa_{1-x}N$/GaN QD and projections of the corresponding states on bulk bands. The energies are given with respect to the VB edge of unstrained GaN. The corresponding quantities for a calculation omitting the built-in electric fields are also listed.

	E (meV)	$\|\langle S\|\Psi\rangle\|^2$	$\|\langle A\|\Psi\rangle\|^2$	$\|\langle B\|\Psi\rangle\|^2$	$\|\langle C\|\Psi\rangle\|^2$
incl. electric fields					
e_0	3208	0.95	0.01	0.01	0.03
e_1	3379	0.94	0.02	0.02	0.02
e_2	3379	0.94	0.02	0.02	0.02
h_0	292	0.0	0.82	0.13	0.05
h_1	286	0.0	0.16	0.79	0.05
h_2	254	0.0	0.70	0.23	0.07
without electric fields					
e_0	3261	0.95	0.01	0.01	0.03
e_1	3343	0.94	0.02	0.02	0.02
e_2	3343	0.94	0.02	0.02	0.02
h_0	138	0.0	0.84	0.14	0.02
h_1	132	0.0	0.18	0.81	0.01
h_2	102	0.0	0.72	0.26	0.02

Tab. 6.1. The table also lists the projections of the single-particle states on the different bulk bands and the corresponding quantities for a calculation omitting the built-in potential.

Impact of the built-in electric fields

The electronic states are governed by the QCSE. First, the electron and hole orbitals are vertically (along [0001]) separated according to the positions of the electronic-band minima resulting from the built-in electric potentials (Fig. 6.7). For this specific QD, the separation of the centers of mass of the electron and hole ground-state orbital is 1.3 nm. Second, compared to the field-free case, the energies of the electron and hole ground states are strongly modified in the field-dependent calculation: the electron ground-state energy is lowered by about 50 meV and the hole ground-state energy is increased by about 150 meV. Omitting excitonic effects, the resulting ground-state transition energy is red-shifted by about 200 meV.

Symmetry properties and band-mixing effects

The projections of the single-particle states on the bulk bands (Tab. 6.1) show that the electron states all have a clear (95 %) CB ($|S\rangle$) character. The shape of the electron ground-state envelope function reproduces the symmetry of the confinement potential, i.e., it is comparable to the *s* state in an atom. The envelope functions of the excited electron levels have the shape of a *p*-like state. Thus, they preserve orthogonality to the ground level.

The situation is different for the hole states. The probability density distributions of the hole ground and first excited state are almost identical; both resemble the symmetry of the confinement potential. The orthogonality of the two states is preserved by the orthogonality of the different VBs. Accordingly, the projection of the hole ground state on the bulk bands yields about 80 % $|A\rangle$-band character, whereas the first excited hole state is of $|B\rangle$-type also with about 80 %. The energy separation between both states is mainly determined by the spin-orbit and crystal-field splitting. The splitting of the ground and first excited state (7 meV) is of the same order of magnitude as the splitting of the $|A\rangle$ and the $|B\rangle$ band in bulk $\mathrm{In_xGa_{1\text{-}x}N}$ [3.2-5.2 meV at $\Gamma^{61;73}$].

The splitting between the first and second excited state is larger (32 meV). The probability density distribution of the second excited state differs significantly from those of the two lower states. The orthogonality to the lower states is attained by the shape of the envelope function, i.e., the probability density distribution shows a knot in its center. The state has an $|A\rangle$-band character (70 %), but less pronounced than the ground state.

Comparison to the field-free QD shows that the built-in fields increase the intermixing with the $|C\rangle$ band as expected from the band-edge profiles (cf Sec. 6.2.2). Its contribution to the hole ground state rises slightly from 2% in the field free case to 5% when the fields are included (see table 6.1).

Despite the large intermixing of all three VBs, a clear $|A\rangle$-type hole ground state and clear $|B\rangle$-type first excited state was found for all QDs investigated in this work. Higher excited hole states are formed by different portions of all three VBs.

Number of Bound States

Bound excited electron levels have only been found for parts of the QDs. Many QDs contain only one localized electron level. The maximum number of bound electron levels for the investigated QDs is three: the *s* ground state and two degenerate excited *p* states. The splitting between the electron ground level and the two excited levels is large compared to the holes states with ($\approx$ 100 meV - 250 meV).

The number of confined hole states, in contrast, is much larger. For all considered QDs, several bound hole levels have been found. As discussed above, the splitting between the ground and first excited state is caused by the spin-orbit and crystal-field splitting. It is always $6-7$ meV and shows almost no dependence on the QD morphology. The splitting between the first and second excited state depends on the QD structure ($\approx 10\,\text{meV}-40\,\text{meV}$). The total number of bound hole levels could not be determined within the present calculations. The large number of confined hole-states exceeds the capabilities of the numerical method. Test calculations for a number of QDs have revealed that they contain at least twelve bound hole levels. The local band-edge profile shown in Fig. 6.6 does not show a stronger confinement for holes than for electrons. The significantly larger number of bound hole states is caused by, first, the larger effective hole masses, and second, the presence of bound $|A\rangle$- and $|B\rangle$-type (and also C-type, in the case of higher excited states) hole states, which significantly increases the density of the hole spectrum.

6.3 Exciton Transition Energies

When a QD sample is excited either optically (e.g., in PL experiments) or electrically (e.g., in electroluminescence or CL), free charge carriers (electrons and holes) are generated in the sample. The electrons and holes can be trapped inside the QDs, where they form confined excitons or excitonic complexes. When these confined excitons (more complex excitonic complexes shall be neglected throughout this section) recombine, they emit light with a specific photon energy (the exciton transition energy) that depends on the exact shape and composition of the QDs. Since not all QDs within the ensemble are identical, the luminescence spectrum of the entire ensemble is the superposition of a large number of different single-QD spectra (inhomogeneous broadening). This ensemble luminescence spectrum is obviously one of the most important optical characteristics of the QD sample.

The PL spectrum of the $\text{In}_\text{x}\text{Ga}_\text{1-x}\text{N}$/GaN QD sample is shown in Fig. 6.8(a). Experimental details of the PL measurements will be given in Sec. 6.4. As alluded to in Sec. 6.1, sharp emission lines from QDs could be observed over the whole spectral range of the ensemble-PL peak from 2.8 eV up to 3.2 eV. This broad distribution of excitonic transition energies is the result of structural variations of the QDs. In order to clarify how certain structural parameters affect the transition energies, calculations were performed for a large number of QDs with varying structural parameters. These model structures have been described in detail in Sec. 6.1. The obtained excitonic transitions energies are shown in Fig. 6.8(b-d). The investigated structural QD properties, height, diameter, and chemical composition, have all a drastic effect on the excitonic

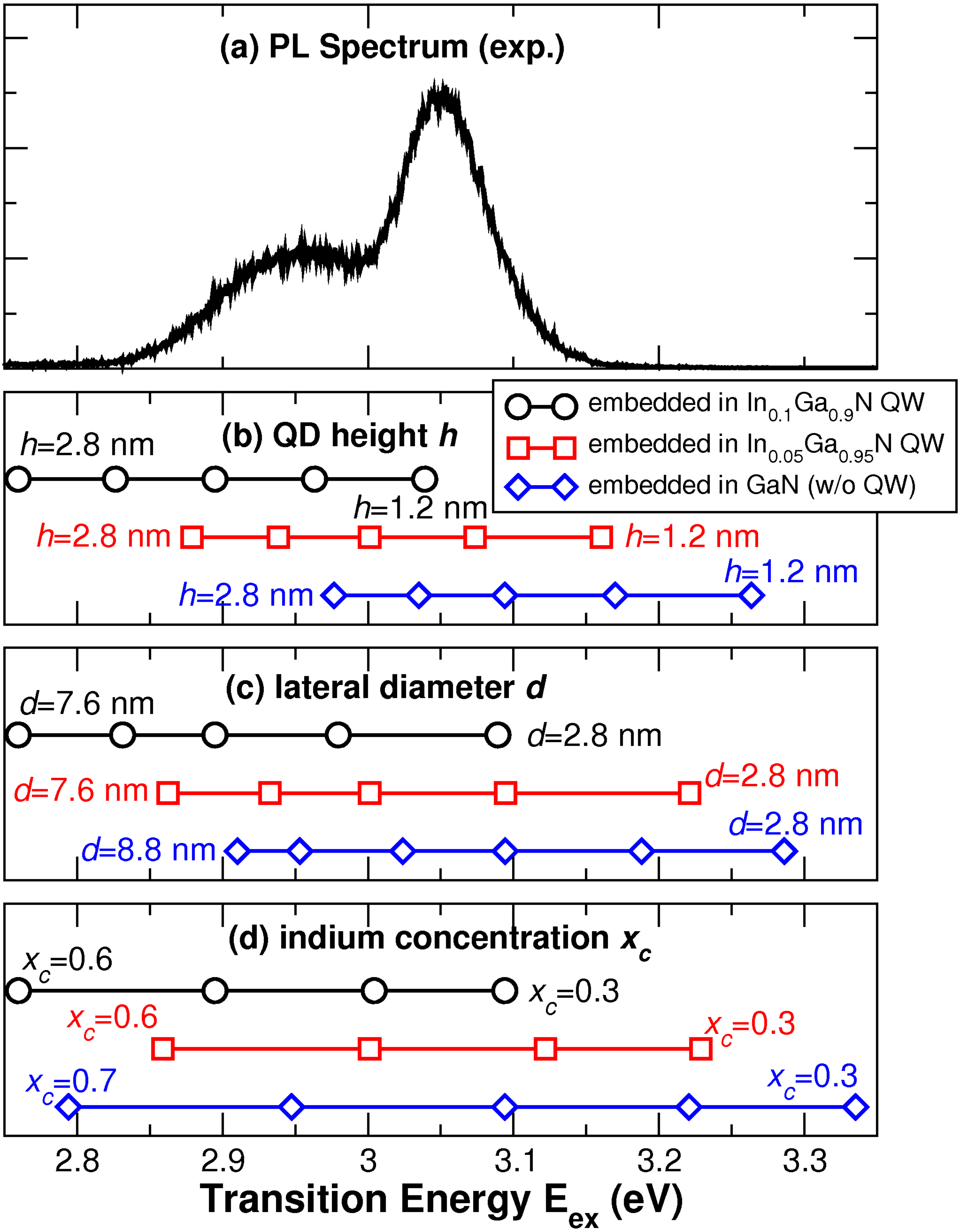

Figure 6.8: (a) PL Spectrum of the $In_xGa_{1-x}N/GaN$ QD ensemble. (b-d) Calculated exciton transition energies for varying QD structures.

transition energies.

These calculations show that slight variations of the QD morphology have a strong impact on the transition energy. Therefore, the presumably large inhomogeneity of QD ensembles results in broad ensemble peaks as measured in luminescence experiments.[24–26;136] The obtained transition energies agree with the experimentally observed energy range. However, to determine which structural parameter is the reason for the broad distribution of transition energies, further experimental input is needed.

6.4 Radiative Lifetimes of Confined Excitons

Time-resolved PL (TRPL) measurements are an excellent tool to investigate the effects of the built-in piezo- and pyroelectric fields, which strongly affect the carrier dynamics in the QDs. Both, the charge carrier separation by the QCSE (and the corresponding increase of the radiative lifetimes) and its dynamical screening are visible in TRPL. In this section a detailed analysis of photon-energy dependent TRPL measurements of the ensemble luminescence of $In_xGa_{1-x}N/GaN$ QDs will be presented. The decay of the ensemble luminescence is strongly multi-exponential for all detection energies. Excitation-density dependent measurements yield no indication for dynamical screening effects (Sec. 6.4.1). Using an inverse Laplace transformation of the transients, a photon-energy-dependent decay-time distribution function is derived that agrees well with recently published single-QD TRPL measurements[25] (Sec. 6.4.2).

The dependence of the radiative lifetimes on the structural properties of the QDs has been calculated and it will be shown that a broad distribution of radiative lifetimes and, in turn, a multi-exponential decay of the ensemble luminescence can be generally expected in this material system (Sec. 6.4.3): The broad distribution of excitonic lifetimes is caused by the built-in electric fields inside the QDs. An ensemble of field-free QDs yields a very narrow lifetime distribution; the individual lifetimes are almost independent from variations of the QD size and structure. If the piezo- and pyroelectric fields are included in the calculations, even slight variations of the QDs' structure lead to pronounced changes of the radiative excitonic lifetimes. Variations of the material composition in the direct vicinity of the QDs also induce drastic changes of the radiative lifetimes .

6.4.1 Experimental Results

For the TRPL measurements the QD luminescence was excited at 353 nm by the second harmonic of a mode-locked Ti:sapphire laser. The temporal width of the laser pulses was 2 ps at a repetition

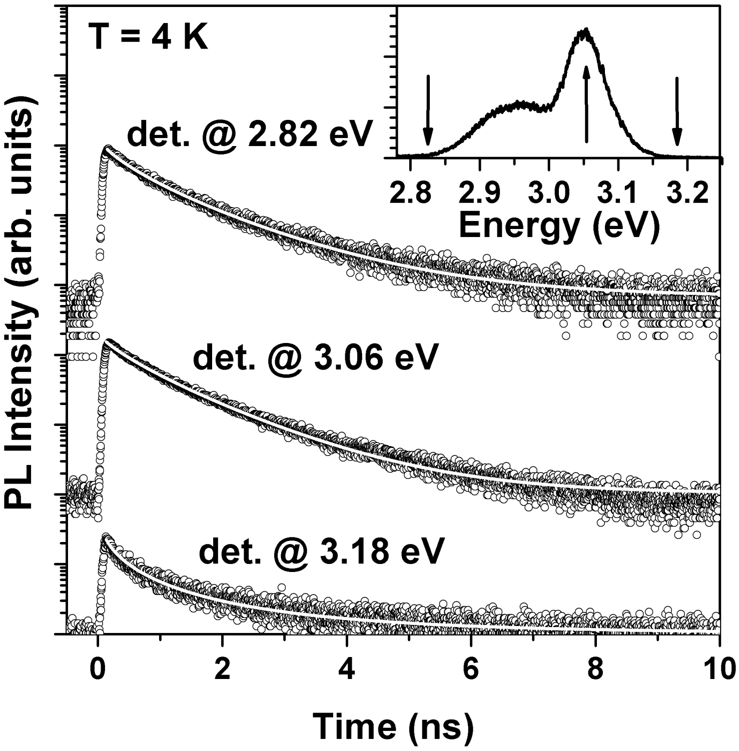

Figure 6.9: Time-resolved PL of an $In_xGa_{1-x}N$/GaN QD subensemble at different detection energies. The PL decays have been fitted (white lines) using the Kohlrausch function (Eq. 6.1). The inset shows the time-integrated PL of the sample. Black arrows indicate the detection energies for the three TRPL decays shown. The shape of the PL peak is attributed to Fabry-Pérot oscillations.

rate of 80 MHz. The measurements were performed in a helium-flow microscope cryostat at a temperature of 4 K. The luminescence was collected through a microscope objective. The detection system consisted of two 0.35 m McPherson monochromators in subtractive mode and an ultrafast photo detector (micro-channel plate) providing a spectral resolution of about 0.6 meV and a temporal resolution better than 30 ps. Further experimental details and the results of single dot TRPL are given elsewhere.[25]

Figure 6.9 shows the temporal evolution of the PL of the $In_xGa_{1-x}N$/GaN-QD ensemble at different detection energies. The PL decay is non-exponential for all transition energies, which is typical for such InGaN layers.[137–140] Two different mechanisms, responsible for the non-exponential decay, have been proposed in the literature: (a) Temporally varying lifetimes due to dynamical screening effects[141;142] and (b) a broad lifetime distribution within the QD ensemble.[25] The first mechanism proposes the screening of the QCSE by photo-generated charge carriers. At low excitation densities electrons and holes are spatially separated by the piezo- and pyroelectric fields inside the QDs. Their wave-function overlap is reduced, and thus, the excitonic lifetimes are long. At high excitation densities enough carriers are generated to significantly screen the electric fields and, hence, the excitonic lifetimes decrease. Thus, in TRPL measurements the luminescence decays quickly at first and then slows down as the excitons recombine. Consequently, the shape of the transients would have to depend on the excitation power. The

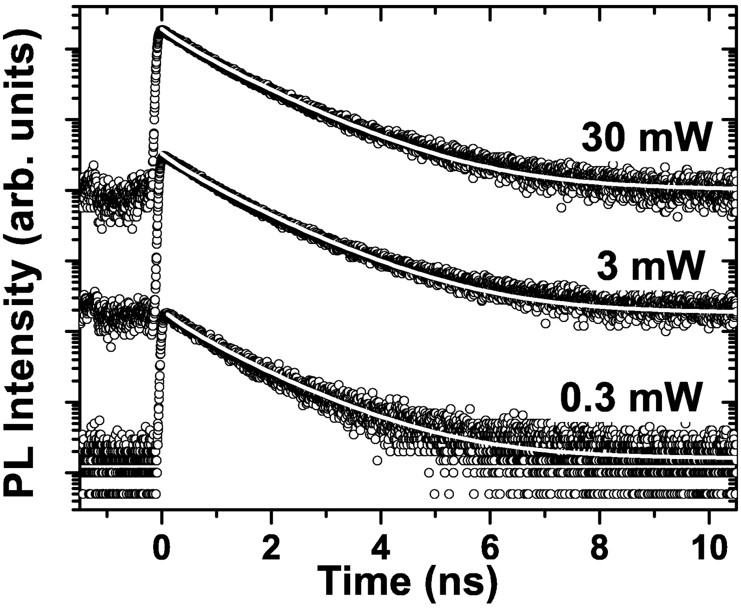

Figure 6.10: Excitation-density dependence of the TRPL signal at fixed detection energy (3.02 eV). The decay can be approximated with the Kohlrausch function (gray lines) for all excitation densities using the same β and τ^* ($\beta = 0.84$, $\tau^* = 0.81$).

PL decay of the investigated sample, however, does not show an excitation density dependence (Fig. 6.10). Also, the mono-exponential decays observed in single-QD TRPL experiments performed on the same sample[25] contradict the screening hypothesis. A similar behaviour—multi-exponential decay of the macro PL and mono-exponential decay in single-QD measurements—has also been reported by Robinson *et al.*[138]. Rice *et al.*[27] have even convincingly demonstrated that they observe the decay of single excitons and biexcitons in their experiments on single $In_xGa_{1-x}N$ QDs. It will be shown in the following sections that the multi-exponential decay of the ensemble PL can be fully understood in terms of a broad lifetime distribution within the QD ensemble and without any dynamical screening effects.

6.4.2 Distribution of Excitonic Lifetimes

All QDs with the same excitonic transition energy E can be considered a subensemble within the entire QD ensemble. The distribution of decay times τ within each subensemble shall be described by the distribution function $f_E(\tau)$. This distribution function can be approximated from TRPL measurements of the subensembles: To eliminate the noise of the experimental data, the multi-exponential subensemble PL decays are approximated by the Kohlrausch (or stretched-exponential) function[143] (solid white lines in Fig. 6.9):

$$I_E(t) = I_{E,0} \exp[-(t/\tau_E^*)^{\beta_E}] \quad . \tag{6.1}$$

Here, τ_E^* and β_E are the time and stretching parameters for the given energy E. τ_E^* is identical

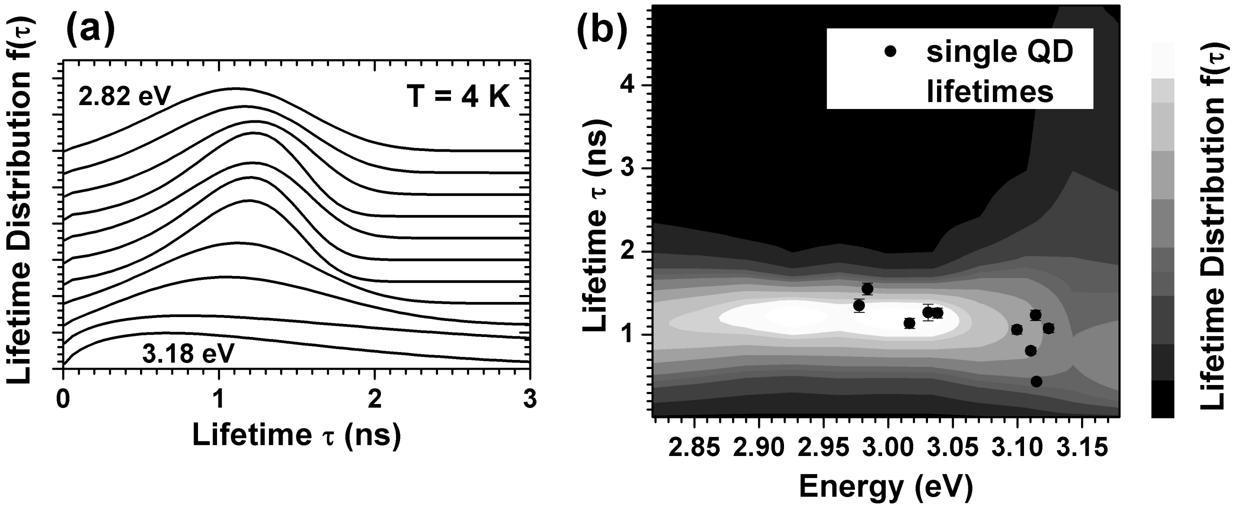

Figure 6.11: (a) Lifetime distribution functions $f_{\mathrm{E}}(\tau)$, obtained by inverse Laplace transformation of the multi-exponential PL decay of different $\mathrm{In_xGa_{1\text{-}x}N}$/GaN-QD subensembles (different detection energies E). The integral of each $f_E(\tau)$ is normalized to 1. (b) $f(E,\tau)$ as gray-scale plot together with the decay times of single $\mathrm{In_xGa_{1\text{-}x}N}$/GaN QDs reported in Ref. 25. The single-dot lifetimes agree well with the obtained distribution function.

to the decay time of the system τ_{E} only if $\beta_{\mathrm{E}} = 1$. It has no direct physical meaning for $\beta_{\mathrm{E}} \neq 1$. The decay of the PL signal at eleven different equidistant detection energies between 2.82 eV and 3.18 eV has been analyzed. The shapes of the transients depend on the detection energy, resulting in varying fit parameters for different QD subensembles ($0.35\,\mathrm{ns} \leq \tau_E^* \leq 0.85\,\mathrm{ns}$; $0.55 \leq \beta_E \leq 0.84$).

The PL decay of each QD subensemble can also be expressed as an integral over the (exponential) single-QD PL decays of all QDs that form the subensemble. Thus, using the Kohlrausch function to describe the decay, Eq. 6.1 can be expanded to

$$I_{\mathrm{E}}(t) \propto \exp[-(t/\tau_{\mathrm{E}}^*)^{\beta_{\mathrm{E}}}] \propto \int_0^\infty f_{\mathrm{E}}(\tau)\exp(-t/\tau)d\tau \quad . \tag{6.2}$$

Mathematically, the subensemble decay $I_{\mathrm{E}}(t)$ is, hence, the Laplace transform of the lifetime distribution function $f_{\mathrm{E}}(\tau)$ within the subensemble, which can, in turn, be obtained by an inverse Laplace transformation of $I_{\mathrm{E}}(t)$.[144;145]

The results of the inverse Laplace transformation are shown in Fig. 6.11. A broad distribution of lifetimes is found for all transition energies, in good agreement with the single-QD TRPL results from Ref. 25 [black symbols in Fig. 6.11(b)], which also show an appreciable scatter for identical transition energies. All single-QD time constants fall in the range covered by the lifetime distribution function.

For GaN/AlN QDs a drastic increase (several orders of magnitude) of the excitonic lifetimes for lower transition energies is observed (cf Chap. 7), which is caused by the increasing QCSE for increasing QD height. Such an effect can not be observed in the lifetime distribution function in Fig. 6.11: The maximum of the distribution function is constant at $\approx 1.2\,\mathrm{ns}$ up to transition energies of $\approx 3.05\,\mathrm{eV}$; for higher transition energies it shifts slightly to shorter lifetimes, accompanied by a broadening of the distribution. The broadening of the distribution at higher transition energies can be explained with the delocalization of charge carriers that are only weakly bound to shallower localization centers.

6.4.3 Quantum Dot Structure and Radiative Lifetimes

The broad lifetime distribution of the $\mathrm{In_xGa_{1\text{-}x}N}$/GaN-QD ensemble can be understood in terms of varying electron-hole wave-function overlap in different QDs. It will be shown here that the variation of the overlap is caused by differences in the built-in piezo- and pyroelectric fields inside each localization center.

The radiative excitonic lifetimes for all $\mathrm{In_xGa_{1\text{-}x}N}$/GaN QDs described in Sec. 6.1 have been calculated (Fig. 6.12). Neglecting the built-in piezo- and pyroelectric fields [Fig. 6.12(a)] all QDs show similar excitonic lifetimes around 0.8-1.0 ns. The radiative lifetimes are insensitive to the exact QD shape and composition. The slight trend to shorter lifetimes at larger transition energies is caused by the small energy dependence of the transition probability (combining Eqs. 3.25 and 3.26 yields $\tau_{\mathrm{rad}} \sim 1/E_{\mathrm{ex}}$ for a given optical matrix element) and the wavelength dependence of the refractive index n. This lifetime distribution would lead to a mono-exponential decay of the ensemble PL for all transition energies. Indeed, such a behaviour has been observed by Sénès *et al.*[146] for $\mathrm{In_xGa_{1\text{-}x}N}$/GaN QDs grown by molecular beam epitaxy, were field effects are reported to be negligible.[146]

For the MOCVD-grown QDs investigated in this work a strong deviation from the mono-exponential decay has been observed for all transition energies. This deviation can be explained if the built-in electrostatic fields are included in the calculations [Fig. 6.12(b-d)]. The radiative excitonic lifetimes now scatter across a wide range between 1.0 and 5.5 ns. Pronounced dependencies on the different structural parameters height, lateral size, and chemical composition can be observed. Interestingly, the radiative lifetimes significantly decrease, when the indium concentration of the surrounding QW is decreased from 10 % to 5 %, or even to 0 %. Then, the matrix exerts an increasing compressive strain along the *z*-axis ([0001]-axis) inside the QDs which reduces the built-in field from $\approx 2.5-4.3\,\mathrm{MV/cm}$ if embedded in a 10 % QW down to

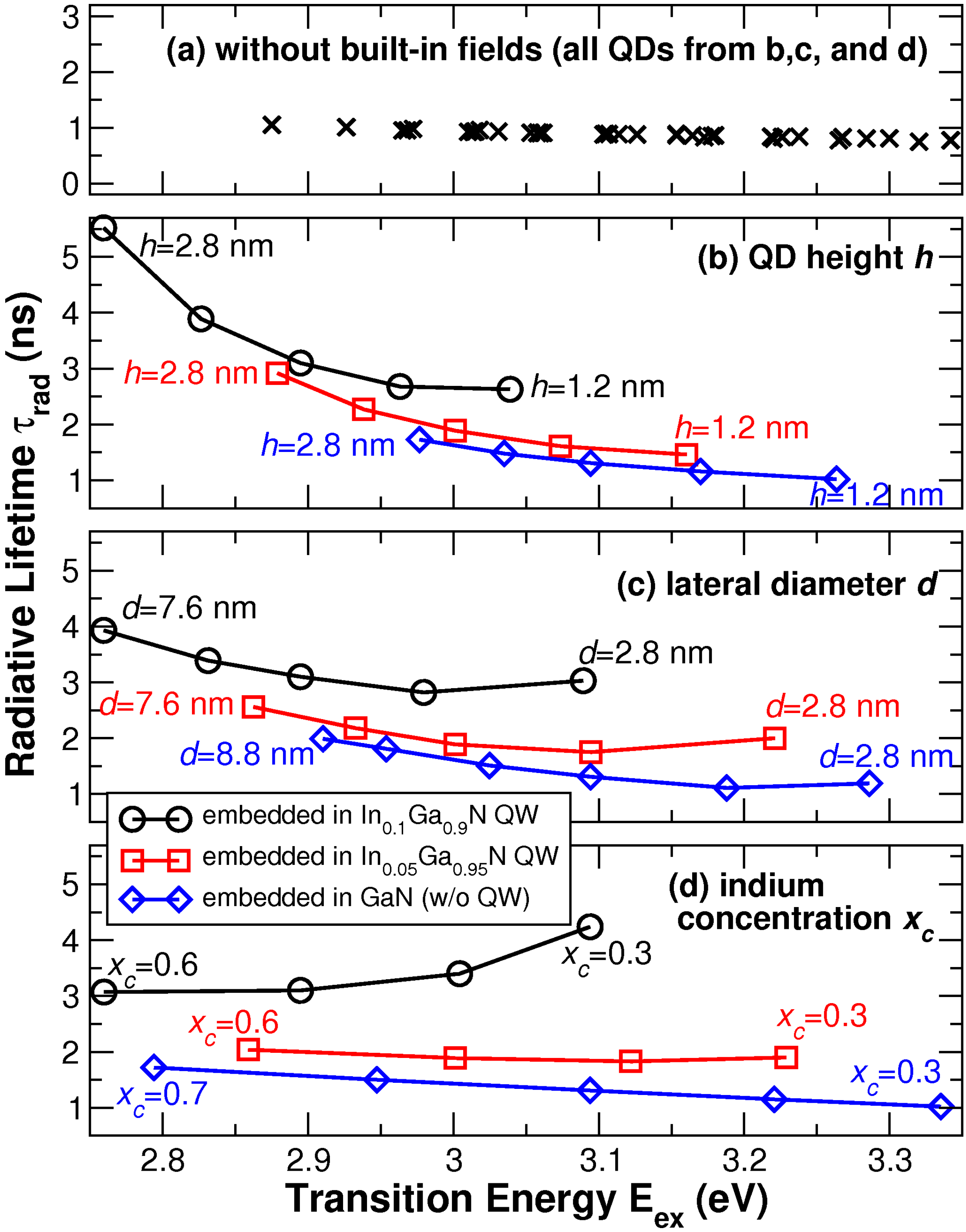

Figure 6.12: Radiative excitonic lifetimes as a function of the transition energy calculated with eight-band $\mathbf{k}\cdot\mathbf{p}$ theory: (a) All model $In_xGa_{1\text{-}x}N$/GaN QDs considered in this thesis (cf Sec. 6.1), neglecting the built-in piezo- and pyroelectric fields. (b-d) As a function of the QD height, diameter, and composition, including piezo- and pyroelectric effects.

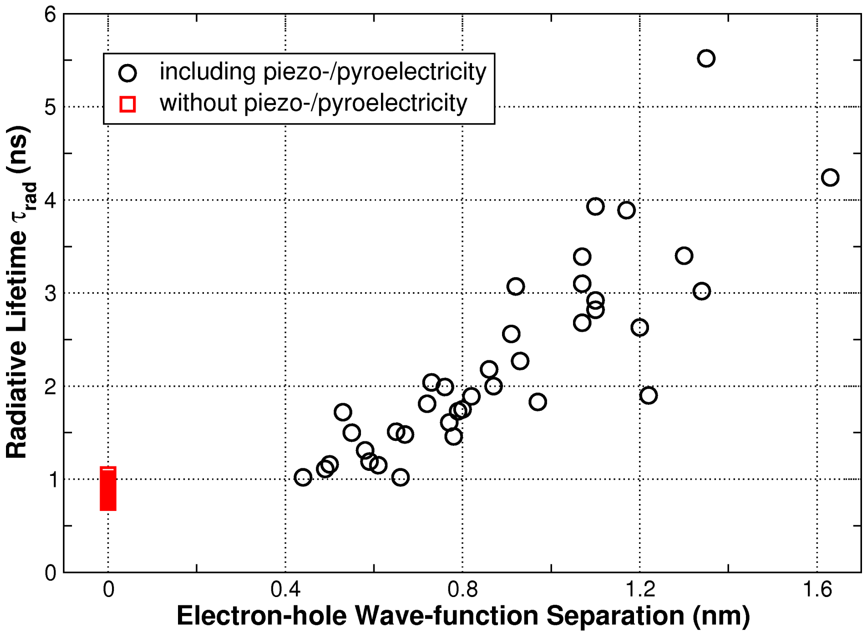

Figure 6.13: Calculated radiative decay times of all $In_xGa_{1-x}N/GaN$ QDs (including built-in electric fields) as a function of the charge-carrier separation inside the QDs.

$\approx 1.7 - 3.1$ MV/cm ($\approx 1.0 - 2.6$ MV/cm) in a 5 % (0 %) QW. The separation of the centers of mass of the electron and hole wave functions decreases from $\approx 0.9 - 1.6$ nm to $\approx 0.7 - 1.2$ nm ($\approx 0.4 - 0.8$ nm). Thus, not only the exact geometry and chemical composition of the QDs themselves, but also the properties of the direct surrounding area of the QDs are decisive for the radiative lifetimes.

The radiative lifetimes are closely related to the electron-hole wave-function overlap, i.e., the spatial separation of both charge-carrier types inside the QDs. Among all considered QD structures the separation (along [0001]) of the centers of masses of the electron and hole wave functions within the exciton complexes varies between 0.7 and 1.6 nm. (It is zero for all QDs in the field-free case.) Figure 6.13 reveals a general trend to longer radiative lifetimes for larger wave-function separations, but also an appreciable scatter of the radiative lifetimes for identical wave-function separations is observed. This scatter is caused not only by the $\tau_{\text{rad}} \sim 1/E_{\text{ex}}$ dependence of the radiative lifetimes on the transition energy, but also by the fact that the effect of the charge carrier separation varies in strength depending on the exact shapes and extensions of the electron and hole wave functions.

A large variety of different time constants is found even for identical transition energies. For instance, among all considered model QDs, six different QDs emit at ≈ 3.1 eV (Fig. 6.12). Although all six QDs have nearly the same transition energy, their radiative lifetimes scatter ap-

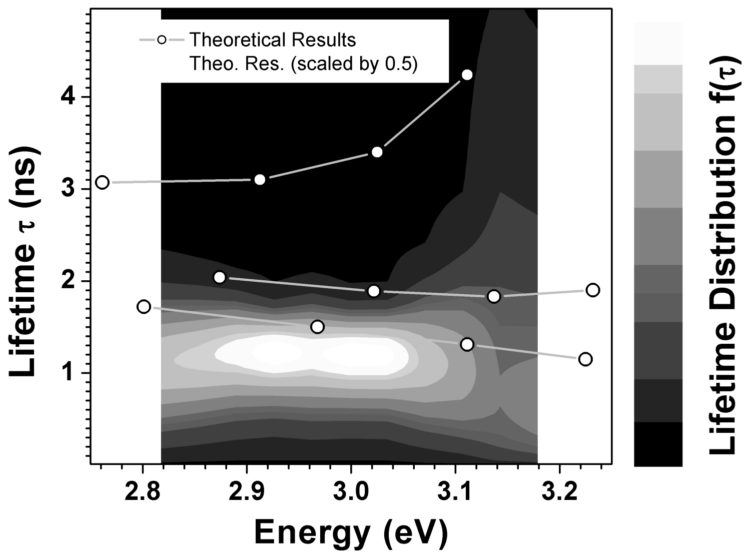

Figure 6.14: Comparison of the lifetime distribution function determined from the experimental PL decays (gray-scale, cf Fig. 6.11) and calculated excitonic lifetimes: White circles and gray lines show the theoretical values from Fig. 6.12(d): $In_xGa_{1-x}N$/GaN QDs with different indium concentrations embedded in a 10, 5, or 0 % InGaN QW.

preciably between 1.3 ns and 4.2 ns. Therefore, no unambiguous relation between the transition energy and the radiative lifetimes of the QDs exists. Luminescence at a certain detection energy originates from a subensemble of QDs, all of which have the same transition energy, but significantly different excitonic lifetimes.

It is clearly not possible to isolate one single structural parameter that is responsible for the broad distribution of transition energies within the QD ensemble. However, an eligible concept should at least reproduce the key features of the lifetime distribution function shown in Fig. 6.11. Theoretically, shifts of the transition energy can be achieved by changing the QD height [Fig. 6.12(b)], lateral diameter [Fig. 6.12(c)], indium concentration in the QD [Fig. 6.12(d)], and, of course, various combinations of these factors. Varying either height or diameter of the QDs yields increasing time constants for lower transition energies [Fig. 6.12(b,c)], which is not supported by the experimental findings (cf Fig. 6.11). Varying the indium concentration inside the QDs, in contrast, does not lead to a significant increase of the time constants on the low-energy side of the spectrum [cf Fig. 6.12(d)]. The calculated lifetimes of the QDs with varying indium concentration are plotted in Fig. 6.14 (white circles and solid lines) together with the lifetimes distribution function obtained from the experimental subensemble PL decays (gray-scale plot). The theoretical lifetimes of this ensemble also reproduce the broadening of the lifetime distribution on the high energy side, which is caused by the delocalization (leaking of the wave function into the matrix and/or into the QW) of the confined electron states in QDs with shallow confinement potential (those embedded in QWs with high indium concentration). The concept of varying indium concentration in QDs embedded in different surrounding QWs describes the experimental results well qualitatively, but quantitatively the calculated lifetimes are generally larger than the measured ones. On the one hand the uncertainties of the material parameters of $\mathrm{In_xGa_{1\text{-}x}N}$ provide a reasonable explanation for this systematic deviation. On the other hand, Narvaez *et al.*[147] have shown for InGaAs/GaAs QDs that the lifetimes of charged excitons (positive or negative trion) are shorter than that of the exciton by a factor of ≈ 0.5. Another possible explanation is, hence, that the PL originates from the decay of charged excitons rather than neutral ones. But also a misconception of the QD structure or an oversimplification in the calculation of the radiative lifetimes are possible. Thus, the reason for the deviation has to remain unclear for the time being.

Still, it can be concluded from the qualitative agreement that a broad distribution of excitonic lifetimes and, consequently, a multi-exponential decay of the ensemble PL is generally expected in this material system in the case of unscreened fields. A mono-exponential decay of the ensemble luminescence, on the other hand, indicates vanishing field effects.

6.5 Polarized Emission Lines: *A*- and *B*-type transitions

In the present section another experimental peculiarity of $\mathrm{In_xGa_{1\text{-}x}N}$/GaN QDs will be investigated: In single-QD cathodoluminescence up to five spectrally narrow lines from one and the same QD can be found. The lines show a pronounced linear polarization in orthogonal directions (Sec. 6.5.1), which could be exploited for the implementation of quantum key distribution protocols[148] using QD-based single-photon sources. It will be shown that the polarization of the lines is owed to the VB structure of wurtzite group-III nitrides and the specific strain distribution in QDs grown on (0001). The calculations reveal that an electron in the ground state (e_0) has a substantial probability to recombine with a hole in either the ground state, which is formed by the A VB ($h_0 \equiv h_A$), or the first excited state, which is formed by the B VB ($h_1 \equiv h_B$). The different characters of the A and B VBs lead to orthogonal polarization directions of both transitions if a slight structural anisotropy of the QD is present (Sec. 6.5.2). The observed polarizations can thus be explained by recombinations of confined excitonic complexes involving holes in the A or B hole states. Examples for such complexes are the A exciton (X_A, with the hole occupying h_A), B excitons (X_B, with the hole occupying h_B), or higher excitonic complexes involving h_A or h_B. Biexcitons with a mixed configuration (XX_{AB}), i.e., with one hole occupying h_A and one

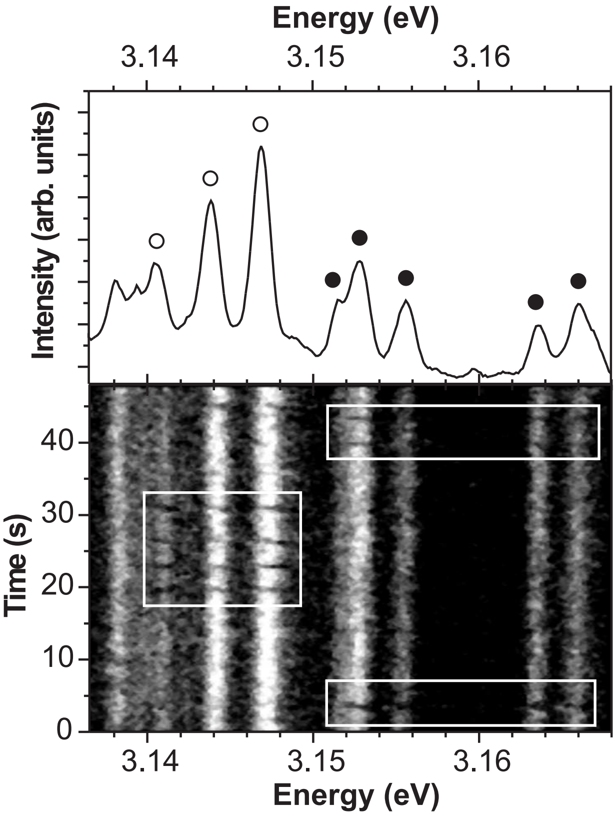

Figure 6.15: Temporal evolution of a typical In$_x$Ga$_{1\text{-}x}$N/GaN QD spectrum. The intensity is coded in gray scale. The series consists of 160 spectra, each being integrated for 300 ms. Two groups of lines that show the same jitter are marked by the full and empty dots. The white rectangles highlight characteristic kinks in the jitter traces.

occupying h_B, have already been observed in bulk GaN.[149]

6.5.1 Experimental Results

The sample was investigated using a JEOL JSM 840 scanning electron microscope equipped with a CL setup.[150] It was mounted onto a He-flow cryostat providing temperatures as low as 6 K. The luminescence light was dispersed by a 0.3 m monochromator with a 2400 lines/mm grating and detected with a liquid-nitrogen cooled Si-charge-coupled-device camera, giving a spectral resolution of 310 μeV at 3 eV. In order to increase the spatial resolution Pt shadow masks have been applied onto the sample surface with aperture diameters of 200 nm.[151] The light emission perpendicular to the sample surface ($\mathbf{k} \parallel c$-axis) is detected. For the determination of each line's polarization direction a polarization filter in the detection path was rotated and the corresponding spectra were recorded. The angle of maximum light emission was determined by fitting a $\cos^2$ formula to the intensities of the single lines as a function of the angle of the polarizer. The angles were mapped to crystal directions based on the substrate orientation as given by the supplier of the silicon substrates.

When measured through one of the apertures the peak from the In$_x$Ga$_{1\text{-}x}$N layer decomposes into sharp lines. The lines show a FWHM of less than 1 meV, the narrowest of 0.48 meV. These lines can be found over a wide energy range from 2.8 to 3.2 eV. Since the line density is very high the high energy side of the ensemble peak has been investigated where the single lines are well resolved. The individual lines are not stable, but vary over a timescale of some 100 ms in their energetic positions and intensities.

This jitter is caused by variations of the local electric field at the position of each QD. Hence, all lines originating from the same QD show the same jitter pattern.[24;31;151;152] An example is shown in Fig. 6.15. Groups of lines originating from one and the same QD have been successfully identified in other material systems (InAs/GaAs,[152] CdSe/ZnSe,[151] GaN/AlN[31]) using these characteristic jitter patterns. Groups of up to five lines displaying the same jitter are found, indicating the existence of a number of different excitonic complexes in the same QD (Fig. 6.16). The typical energetic spread of the five lines was found to be $\lesssim 20$ meV. All lines show a pronounced linear polarization in orthogonal directions. The polarization directions scatter around the $[11\bar{2}0]$ and $[\bar{1}100]$ direction. Both directions were found in each investigated line group. (Fig. 6.17) Such behavior has not been observed before and deserves closer investigation. In III-V arsenides, phosphides and II-VI materials polarized emission lines from QDs have been assigned to the fine structure of the exciton[20;153–156] or charged biexciton emission.[157;158] The source for both effects is the anisotropic exchange interaction between confined electrons and holes, which leads to a systematic pattern of the polarized lines (polarized doublets, similar order or similar energetic distance of co-polarized lines for different QDs). No such scheme can be deduced from the recorded spectra here (Fig. 6.16). Hence, a different mechanism responsible for the polarization of the lines is suggested.

6.5.2 *A*- and *B*-band Hole States

It has been demonstrated in Sec. 6.2 that *A*- and *B*-type hole states can be found in $\mathrm{In_xGa_{1\text{-}x}N}$/GaN QDs. The confined hole ground state (h_A) is predominantly of *A*-type, while the first excited hole state (h_B) is predominantly of *B*-type. Both have an *s*-type envelope function and are energetically separated by ≈ 7 meV. It will be shown in the following that the transitions between the electron ground state (e_0) and both of these hole states have substantial oscillator strengths and that even a small structural anisotropy of the QDs leads to pronounced polarization of these transitions in orthogonal directions. The structural anisotropy leads to an anisotropic strain field inside the QD. Following the line of Sec. 5.2, this strain anisotropy changes the character of the uppermost VBs. This effect can be observed in the character of the confined hole states and shall be calculated here. For the calculations, an ellipsoidal model QD as described in Sec. 6.1

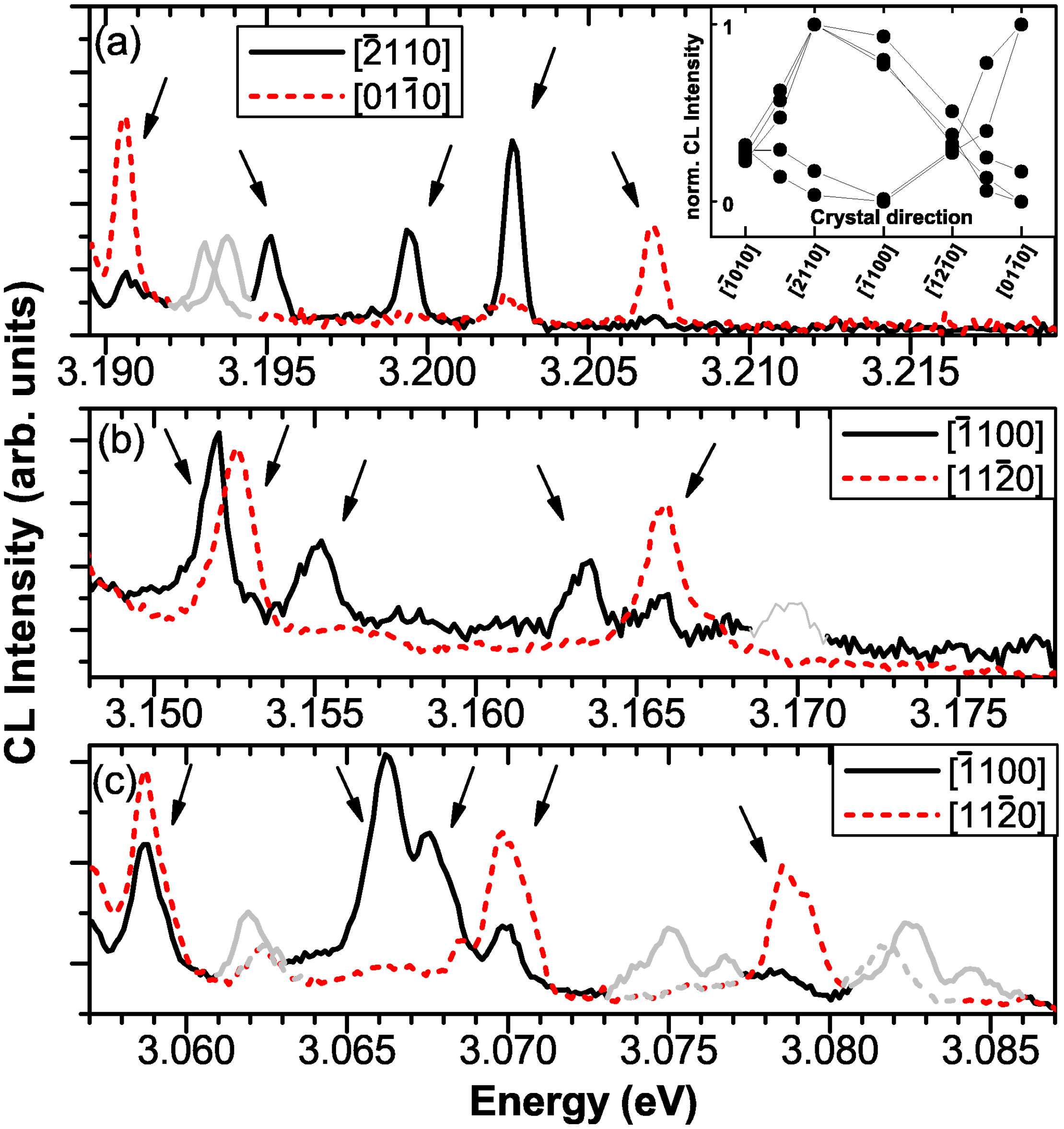

Figure 6.16: Polarized spectra of three different $In_xGa_{1-x}N$/GaN QDs. Arrows indicate lines displaying the same jitter, hence originating from the same QD. Gray lines originate from other QDs. The inset shows the evolution of the peak intensities as a function of the polarization angle. Closer analysis yields deviations from the $[11\bar{2}0]$ and $[\bar{1}100]$ crystal directions of $13^\circ \pm 16^\circ$ for QD (a), $-4^\circ \pm 4^\circ$ for QD (b), and $-13^\circ \pm 2^\circ$ for QD (c).

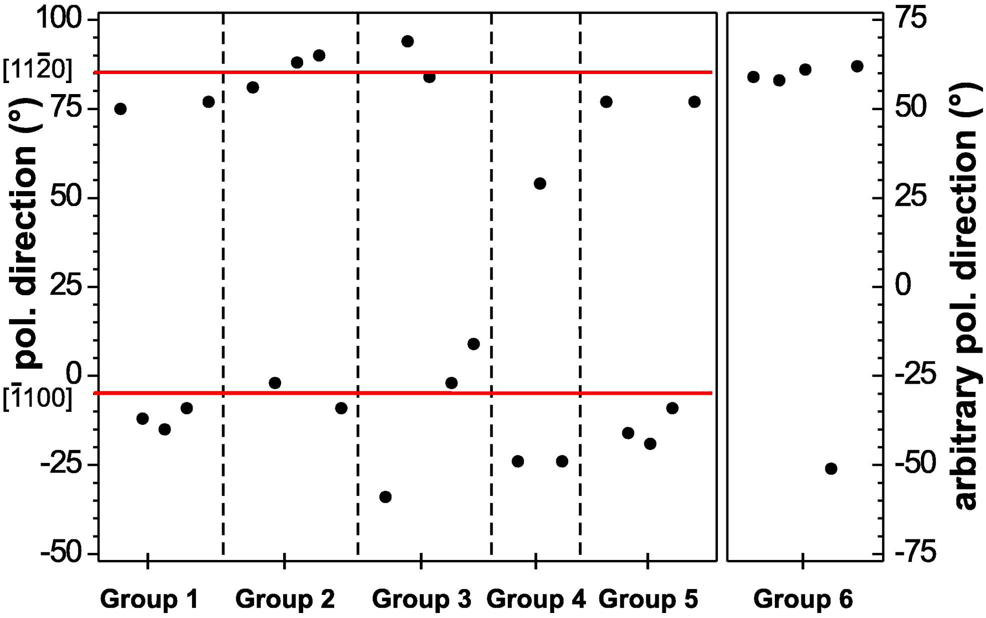

Figure 6.17: Polarization directions of six different line groups. They scatter around [11$\bar{2}$0] and [$\bar{1}$100]. Both directions can be found in each line group. For line group No. 6, the alignment of the polarization directions to the crystal axes is unknown. Groups 1-3 correspond to the spectra (a)-(c) in Fig. 6.16.

has been used with the following structural parameters: The indium concentration is $x_\mathrm{c} = 50\,\%$ at the QD's center and $x_\mathrm{e} = 5\,\%$ at its edges. The QD has a height of $d_\mathrm{z} = 2.0\,\mathrm{nm}$ (parallel to the *c*-axis), a lateral diameter of $d_\mathrm{x} = d_\mathrm{y} = 5.2\,\mathrm{nm}$ (in the basal plane), and is embedded in an $\mathrm{In_xGa_{1\text{-}x}N}$ QW with a height of 2.0 nm and In concentration of $x_\mathrm{w} = x_\mathrm{e} = 5\,\%$.

The oscillator strengths between the single-particle electron and hole states for QDs with different degrees of elongation in the basal plane are shown in Fig. 6.18. The in-plane aspect ratio of the QD, d_x:d_y, has been altered between 1:1 and 1.25:1, while the total amount of indium has been kept constant. Three bound electron levels and a much larger number of bound hole levels (>6) are found. The spectra in Fig. 6.18 include all single-particle (electron-hole-pair) transitions involving one of the three bound electron levels and one of the first six bound hole levels. Non-vanishing oscillator strengths were found for the transition between the electron ground state and the hole ground state (e_0,h_A), the transition between the electron ground state and the first excited hole state (e_0,h_B), and transitions involving higher excited hole states and excited electron states. However, the latter have much higher transition energies and weaker oscillator strengths (Fig. 6.18). The (e_0,h_A) and (e_0,h_B) transitions are energetically separated by only $7-10\,\mathrm{meV}$. Both transition lines are unpolarized for round QDs (d_x:d_y = 1:1). For

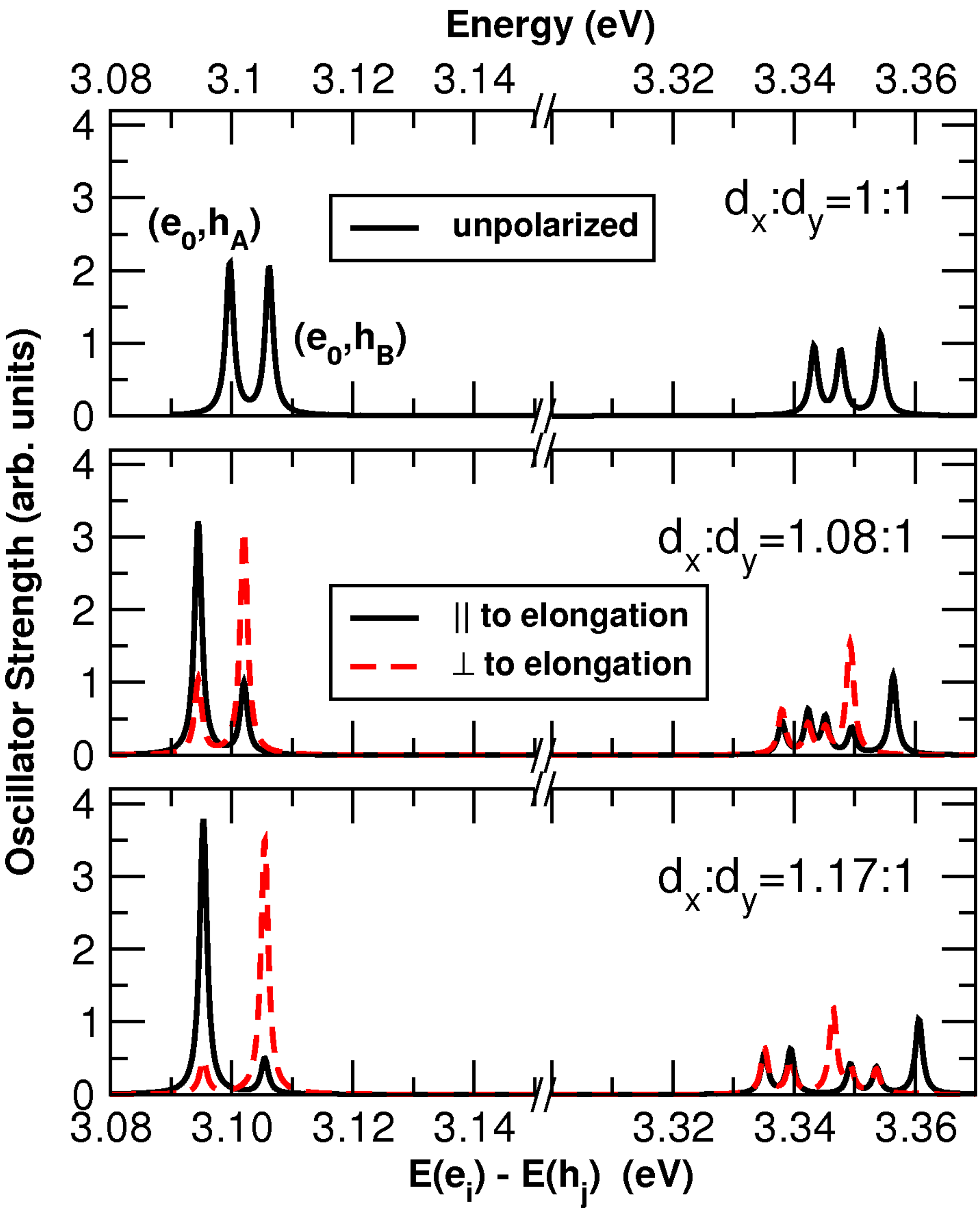

Figure 6.18: Oscillator strengths between electron and hole states in $In_xGa_{1-x}N/GaN$ QDs with different degrees of elongation. The solid (dashed) lines show the oscillator strength parallel (perpendicular) to the QD elongation. The *x* axis shows the energy difference between the involved electron and hole states.

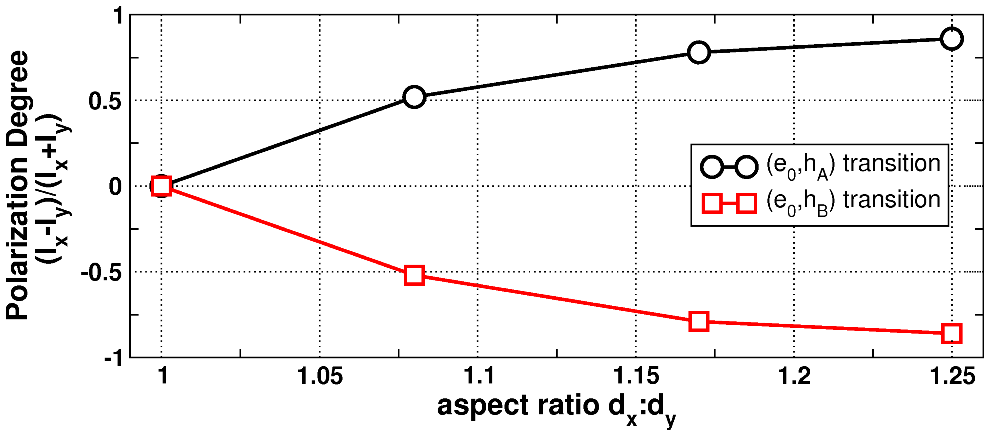

Figure 6.19: Degree of linear polarization of the e_0-h_A (black line and circles) and e_0-h_B (red line and squares) transitions as a function of the in-plane elongation of $In_xGa_{1-x}N$/GaN QDs.

asymmetric QDs the *A*-band transition is linearly polarized parallel to the QDs' long axis and the *B*-band transition perpendicular to it. Even for a very slight asymmetry of 1.08:1, the degree of polarization of both lines is already $\approx$ 3:1. An elongation of 1.25:1 results in an almost complete linear polarization (Fig. 6.19).

The single-particle electron and hole orbitals are depicted in Fig. 6.20 for a circular QD (left) and a slightly elongated QD (d_x:d_y = 1:1.17) (right). The electron ground-state (e_0) envelope functions have *s*-like symmetry; the ones of the first two excited electron states ($e_{1/2}$) are *p*-like. The first two hole states, h_A and h_B, in contrast, both have *s*-like envelope functions. Both states have sizable oscillator strengths with the electron ground state, but behave differently if the QD is elongated: h_A aligns parallel to the QD's long axis, h_B perpendicular to it. An analysis of the projections of both hole states on the $\mathbf{k}\cdot\mathbf{p}$ basis states P_x and P_y (cf Sec. 5.2) yields that the P_x (P_y) projection of h_A (h_B) increases with increasing QD elongation, while the P_x (P_y) projection decreases (see Tab. 6.2). Consequently, the optical transition between h_A (h_B) and e_0 is linearly polarized parallel (perpendicular) to the QD's long axis (here, the *x* axis).

6.5.3 *A*- and *B*-type Transitions of Excitonic Complexes

The two electron-hole-pair configurations (e_0,h_A) and (e_0,h_B) are part of many different confined few-particle complexes, such as excitons (X), biexcitons (XX), or charged excitonic complexes [e.g., positive (X^+) and negative (X^-) trions]. Thus, the emission spectra of these complexes show the same polarization behavior—linear, in orthogonal directions—as found for the single particle transitions (Fig. 6.21). Considering the irregular shapes of the fluctuation-induced QDs,

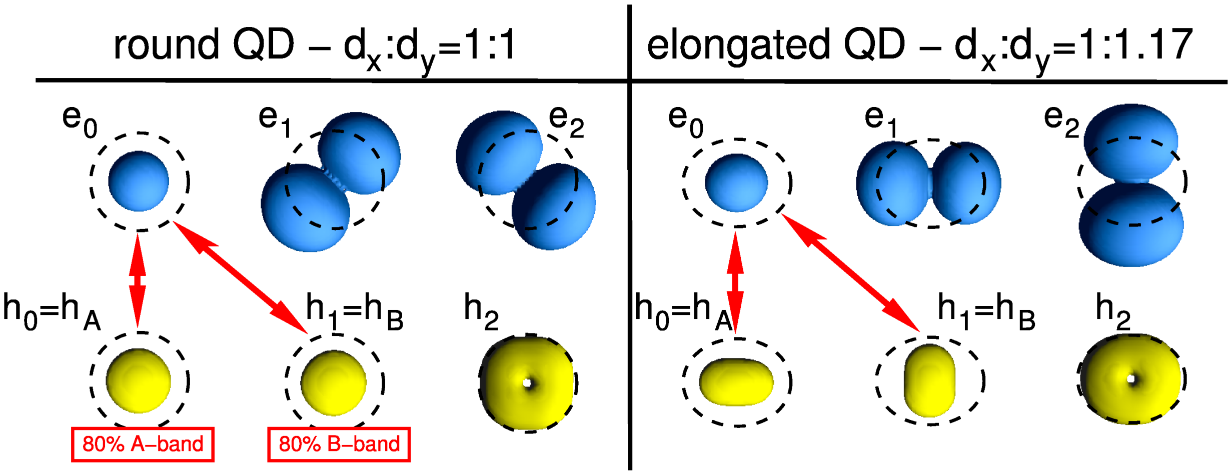

Figure 6.20: Single-particle states in a round (left) and an elongated (right) $In_xGa_{1-x}N$/GaN QD. The electron ground state has a finite oscillator strength with the hole ground state *and* with the first excited hole state.

an arbitrary elongation in the basal plane is very likely. It can, therefore be concluded that *A*- and *B*-type transitions of different few-particle states are the reason for the observed linear polarization of the emission lines. The cause for the regular orientation of the QDs along the $[11\bar{2}0]$ and/or $[\bar{1}100]$ directions, however, remains unclear.

As an example of a possible few-particle spectrum, Fig. 6.21 shows the calculated oscillator strengths for the confined X, XX, and negative trion, X^-, including both, the *A*- and *B*-like states. All transition lines are linearly polarized. The polarization direction of each transition depends on whether an *A* or *B* hole state is involved in the recombination process. The resulting spectrum is qualitatively similar to the measured spectra. Note that the exact transition energy of each line heavily depends on a number of parameters which are yet unknown with sufficient precision, most important the crystal-field and spin-orbit splitting energies of $In_xGa_{1-x}N$, the strength of the

Table 6.2: Projections of the hole states h_A and h_B on the bulk A and B VBs and on the $\mathbf{k}\cdot\mathbf{p}$ basis states P_x and P_y.

	$h_0 \equiv h_A$				$h_1 \equiv h_B$			
d_y/d_x	A	B	P_x	P_y	A	B	P_x	P_y
1	0.81	0.13	0.47	0.47	0.16	0.78	0.47	0.47
1.08	0.76	0.18	0.26	0.68	0.21	0.73	0.67	0.26
1.17	0.69	0.25	0.16	0.78	0.28	0.66	0.77	0.17
1.25	0.66	0.29	0.12	0.83	0.32	0.62	0.81	0.13

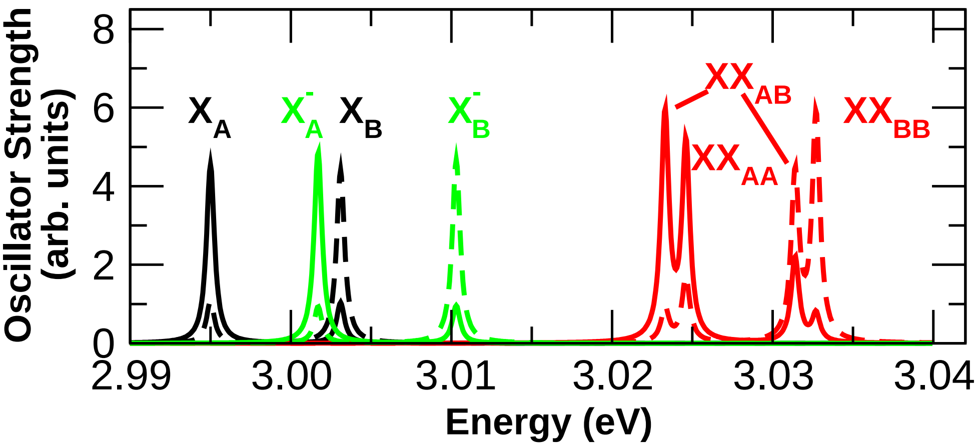

Figure 6.21: Calculated few-particle transitions for an $In_xGa_{1-x}N/GaN$ QD with an in-plane elongation of d_x:$d_y = 1.08$:1; X (black lines), XX (red lines), and X^- (green lines) lines. The solid (dashed) lines show the oscillator strength parallel (perpendicular) to the QD elongation.

built-in electric fields, and the exact shape and size of the QDs. Also, the occupation probabilities of the different states are unknown. Therefore, the emission lines in Fig. 6.16 can not be assigned to specific excitonic complexes yet.

6.6 Summary

In this chapter the electronic and optical properties of $In_xGa_{1-x}N/GaN$ QDs have been investigated within the framework of eight-band $\mathbf{k}\cdot\mathbf{p}$ theory. A large impact of the built-in piezoelectric and pyroelectric fields on the electronic states has been observed. The fields cause a spatial separation of electron and hole wave functions and a redshift of the transition energies of hundreds of meV. The QDs show a rich-featured spectrum of hole states, resulting from the VB structure of wurtzite group-III nitrides and the specific strain situation in QDs. The confined hole states are formed predominantly by the two highest VBs. The hole ground state is formed by the *A* band, and the first excited hole state by the *B* band.

Experimental observations on $In_xGa_{1-x}N/GaN$ QDs has been investigated and explained theoretically. The modelling results revealed a pronounced dependence of the excitonic transition energies and radiative lifetimes on the structural properties of the $In_xGa_{1-x}N/GaN$ QDs, i.e., their chemical composition, height, and lateral extension, which has been used to explains the experimentally observed broad ensemble PL peak of the QD ensemble. The multi-exponential decay of the ensemble PL could be consistently explained with with a large scatter of the radiative excitonic lifetimes even for identical transition energies. It has been shown that the scatter of the radiative lifetimes is induced by variations of the built-in electrostatic fields. Single-QD emission spectra from $In_xGa_{1-x}N/GaN$ QDs with up to five lines per QD have been discussed. The emission lines are linearly polarized in orthogonal directions. The large number of emission lines has been explained with the existence of higher excitonic complexes; their polarization with a slight anisotropy of the QDs in the basal plane and recombinations involving hole states which are either formed by the *A* or *B* VB.

It will be shown in the following chapter (7) that a number of insights gain in the present chapter are not restricted to $In_xGa_{1-x}N/GaN$ QDs, but apply also to GaN/AlN QDs, because they are general features of *c*-plane group-III nitride QDs. These are, in particular, the modification of the electronic structure by the built-in electrostatic fields, the occurrence of *A*- and *B*-type hole states, and the polarization effect resulting from strain anisotropy in the basal plane.

7 GaN/AlN Quantum Dots

Despite tremendous advances in single quantum-dot (QD) spectroscopy on GaN/AlN QDs,[21;31;32;34;159;160] many of their basic properties are still not or only poorly understood. In this chapter the spectroscopic properties of *c*-plane GaN/AlN QDs are studied theoretically within the framework of eight-band $\mathbf{k}\cdot\mathbf{p}$ theory. Structural properties of the QDs (Sec. 7.1) are quantitatively correlated to spectroscopic properties, such as excitonic ground-state transition energies, radiative excitonic lifetimes (Sec. 7.2), and few-particle (biexciton and charged excitons) binding energies (Sec. 7.3). The allowed recombination channels between the confined electron and hole states are analyzed. It is shown that an anisotropy of the QD confinement potential in the basal plane (e.g. elongation of the QDs or strain anisotropy) leads to a pronounced linear polarization of the interband transitions (Sec. 7.4). It will be shown that an asymmetric strain field in the basal plane inside the QDs leads to a linear polarization of the confined *A*- and *B*-type excitonic states in orthogonal directions. The in-plane strain anisotropy can originate from different sources, such as QD elongation, inhomogeneous composition profiles, etc. As examples a slight elongation of the QDs (Sec. 7.4.1) and, as an ex-situ approach, the application of external uniaxial stress (Sec. 7.4.2) are considered in detail.

7.1 Model Structure

Experimental reports on the structural properties of *c*-plane GaN QDs[21;30;33;35;161–170] agree on the shape of the QDs, which is a truncated hexagonal pyramid. The reported heights (h) of the QDs scatter between 1.3 nm and 5 nm. The aspect ratio (h:d, where d denotes the lateral diameter) in most reports is in the range of 1:5 to 1:10. The model structure derived from these reports is depicted in Fig. 7.2. The model QDs have an aspect ratio of either $h{:}d = 1{:}10$ or 1:5 (Fig. 7.1). The height of the QDs has been varied between 1.5 nm and 3.5 nm in steps of 0.5 nm. The thickness of the wetting layer is assumed to be $w = 0.25$ nm. This set of model

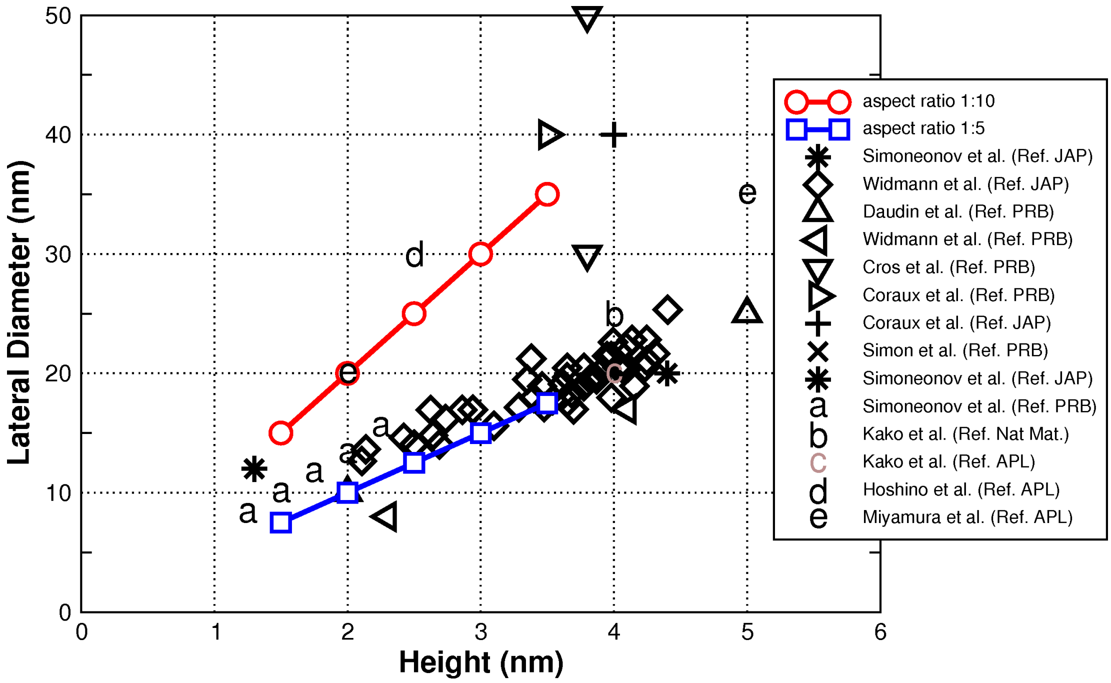

Figure 7.1: Experimentally observed heights and diameters of *c*-plane GaN/AlN QDs.[21;30;33;35;161–169] *Red lines and circles* and *blue lines and squares* indicate the structural parameters of the model QDs used in this work.

QDs covers the major part of reported QD structures. It will be shown in the following section that the chosen model structures yield excitonic emission energies and radiative lifetimes in good agreement with experimentally observed values.

7.2 Exciton Transition Energies and Radiative Lifetimes

The huge built-in piezo- and pyroelectric fields inside GaN/AlN QDs strongly affect the emission energies and radiative lifetimes of localized excitons in the QDs via the quantum-confined Stark effect.[47;48;163;171] In the center of the QD these fields are as large as 9.5 MV/cm for QDs with an aspect ratio of 1:10 and 8.0 MV/cm for QDs with an aspect ratio of 1:5. Depending on the size of the QDs the radiative lifetimes range from a few nanoseconds for small QDs up to as long as 100 μs for large QDs (Fig. 7.3). Only for small QDs the emission energy is larger than the fundamental band gap of GaN, larger QDs emit at energies well below the band gap of GaN.

The calculated radiative excitonic lifetimes for the model QDs with aspect ratio 1:10 (red lines and squares) and 1:5 (blue lines and circles) are plotted in Fig. 7.3 as a function of the transition energy. The experimental values by Bretagnon *et al.*[48] (black crosses) and Kako *et*

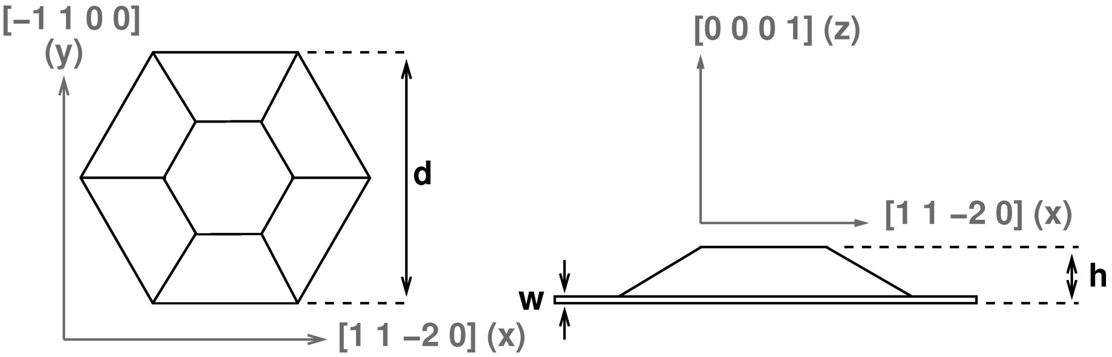

Figure 7.2: Model structure of c-plane GaN/AlN QDs: Truncated hexagonal pyramid with height h between 1.5 nm and 3.5 nm. The lateral diameter d is determined by the dot's aspect ratio h:$d = 1$:10 (1:5). The wetting layer is $w = 0.25$ nm thick.

al.[21] (black plus) are also shown in the same figure. The exciton transition energy depends crucially on the QD height. An increase of the QD height by 0.5 nm leads to a red shift of the transition energy by 400-500 meV. Increasing the aspect ratio from 1:5 to 1:10 decreases the transition energy by 200-400 meV depending on the QD height. Keeping in mind that the base area increases by a factor of four upon this change of the aspect ratio, it can be concluded that the transition energy is predominantly determined by the QD height and the lateral extensions can be regarded as a secondary factor.

Both series yield comparable relations between excitonic transition energy and radiative lifetime with lifetimes of 8.6 ns (4.9 ns) for high transition energies of ≈ 3.63 eV (≈ 3.84 eV) and values as high as 210 μs (55 μs) for the lowest transition energy of ≈ 1.77 eV (≈ 2.18 eV). The calculated lifetimes agree very well with the experimentally observed decay times for both series. The QDs with h:$d = 1$:5 show slightly longer radiative lifetimes at comparable transition energies, but the general relation between excitonic transition energy and radiative lifetime is similar for both aspect ratios.

Radiative lifetimes in the range of 100 μs would limit cut-off frequencies of devices to a maximum of a few kHz. Thus, with the fields present, only small c-plane QDs, i.e. those with high transition energies, are good candidates for fast single-photon emitters.

7.3 Binding Energies of Few-particle Complexes

As a result of the strong built-in electric fields inside the QDs, the biexciton (XX) is anti-binding in most c-plane GaN/AlN QDs.[21;30;33] Only for QDs with very high transition energies (≈ 4 eV) binding biexcitons have been observed by Simeonov *et al.*[33] Due to the spatial separation of

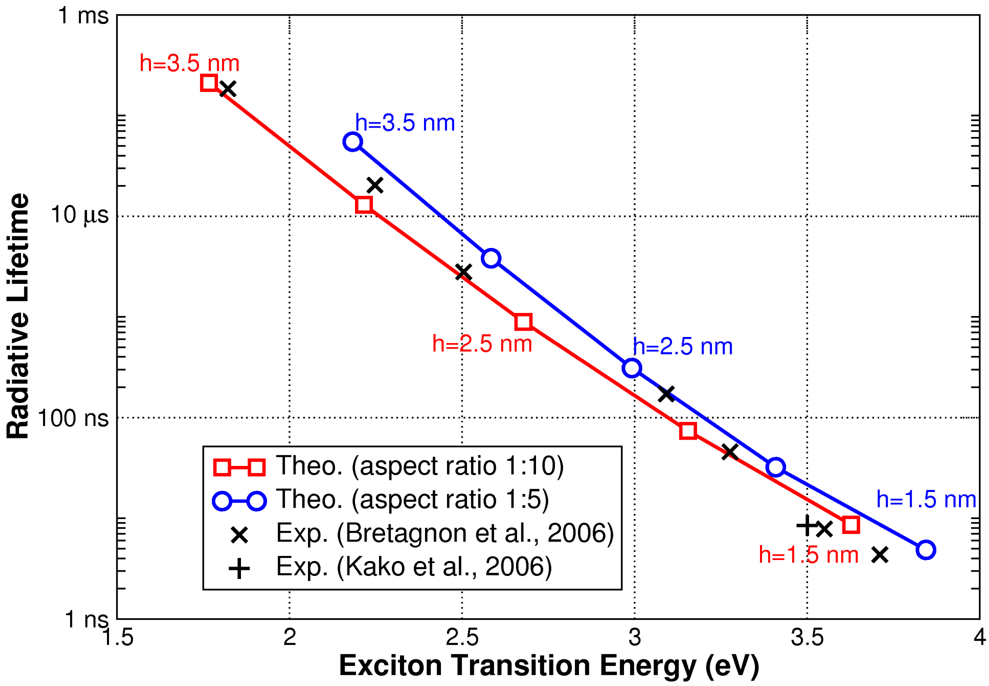

Figure 7.3: Radiative lifetimes of confined excitons in c-plane GaN/AlN QDs: *Red lines and squares:* Calculated, QDs with an aspect ratio of $h{:}d = 1{:}10$. *Blue lines and circles:* Calculated, QDs with an aspect ratio of $h{:}d = 1{:}5$. *Black crosses:* Experimental values from Bretagnon *et al.*[48]. *Black plus:* Experimental value from Kako *et al.*[21].

electrons and holes, the repulsive Coulomb terms between two electrons or between two holes always outweigh attractive terms between electrons and holes. This is also true for positive and negative trions (X^+ and X^-), which are also anti-binding. The calculated binding energies of X^+, X^-, and XX for all considered model QDs are shown in Fig. 7.4. Positive values correspond to anti-binding complexes, i.e. to a spectroscopic blue shift with respect to the exciton. The spectroscopic blue-shift of the X^+ is always larger than that of the X^-, because the hole orbitals are smaller in extent (due to their larger effective masses) than the electron orbitals. Therefore, the repulsive Coulomb terms between two holes are larger than those between two electrons. In QDs with small aspect ratio and high transition energy the binding energy of the X^- is only a few meV. Keeping in mind that the theory used here neglects exchange and correlation effects, which are both expected to lead to more binding biexcitons, it is thus possible that the X^- is in fact binding (red-shifted with respect to the X) in these QDs. The XX is always the most anti-binding complex. Its binding energy, however, is not necessarily identical to the sum of the binding energies of X^+ and X^-, due to the different wave-function renormalizations in the different complexes.

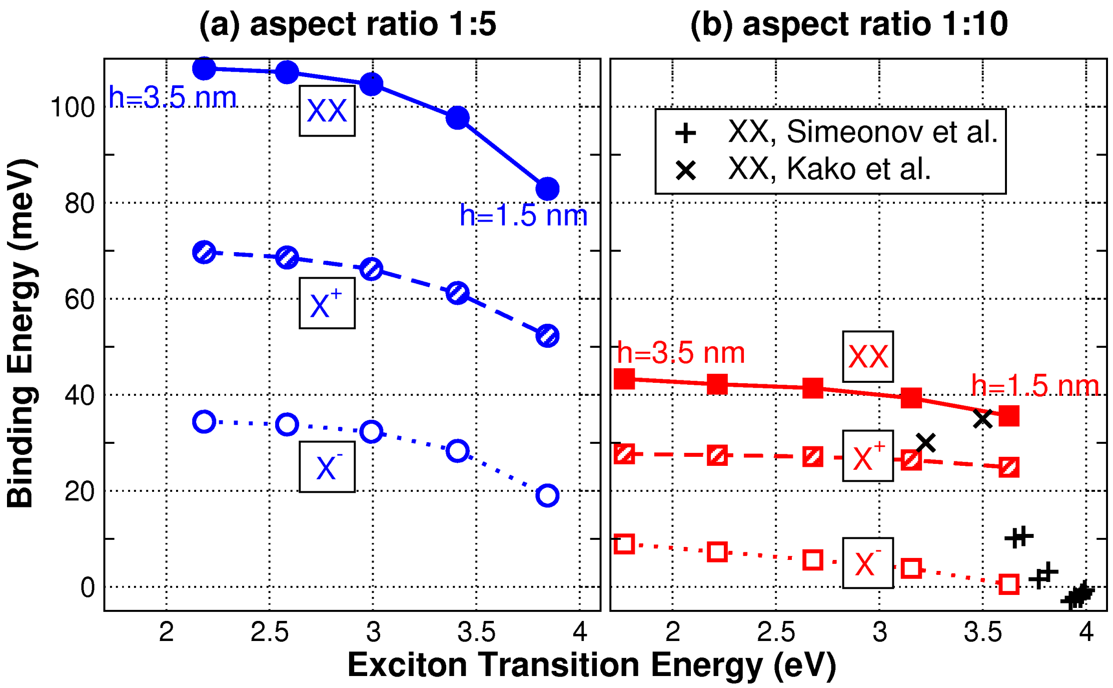

Figure 7.4: Calculated binding energies of the few-particle complexes biexciton (XX), positive trion (X^+), and negative trion (X^-) with respect to the exciton (X) in GaN/AlN QDs. Positive values correspond to anti-binding complexes. *left:* QDs with an aspect ratio of $h{:}d = 1{:}10$. *right:* QDs with an aspect ratio of $h{:}d = 1{:}5$. The black crosses (pluses) denote to the experimental value of the biexciton binding energies determined by Kako *et al.*[21;30] (Simeonov *et al.*[33]).

The binding energies of the few-particle complexes are very sensitive to the aspect ratio of the QDs. All binding energies are significantly larger in QDs with an aspect ratio of 1:5 [Fig. 7.4(a)] than in QDs with an aspect ratio of 1:10 [Fig. 7.4(b)]. The XX binding energy in QDs with $h{:}d$=1:5, for instance, is more than twice as large than in QDs with $h{:}d$=1:10 for all transition energies. This makes the XX binding energy, or equivalently the X^+/X^- binding energy, an excellent fingerprint for the QDs aspect ratio. The QDs investigated by Kako *et al.*[21;30] [black crosses in Fig. 7.4(b)], for instance, seem to have an aspect ratio around 1:10 rather than 1:5, although the average height and diameter of the QD ensemble is 4 nm and 20 – 25 nm, respectively.[21;30] The values determined by Simeonov *et al.*[33] [black pluses in Fig. 7.4(b)] are much smaller than the XX binding energies calculated here, which is consistent with their assumption of weaker built-in electrostatic fields ($\approx$ 5.5 MV/cm).

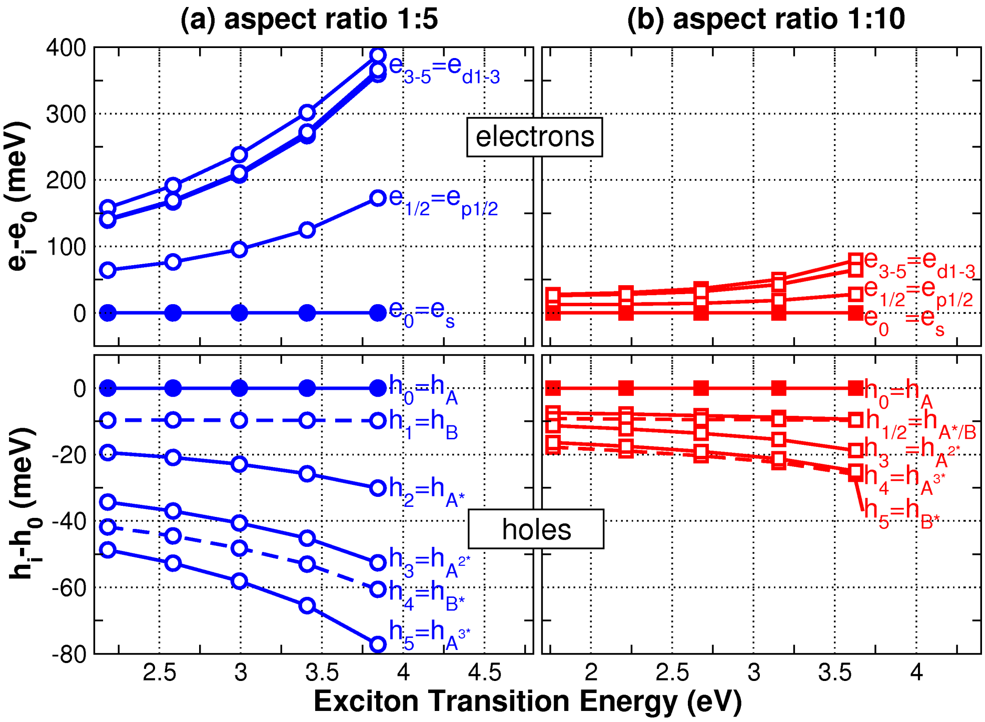

Figure 7.5: Energies of the single-particle electron and hole states in *c*-plane GaN/AlN QDs. The electron states are labeled according to the symmetry of their envelope functions. Hole-state labels are given according to the valence band that the states are predominantly formed of.

7.4 Single-particle Energy Levels

The bound hole states in GaN/AlN QDs are—as in the case of In$_x$Ga$_{1\text{-}x}$N/GaN QDs (cf Chap. 6)—formed predominantly by the *A* and *B* band. *C*-band contributions are small because the biaxial strain in the QDs shifts this band to much lower energies.[29;60] As a first-order approximation, for each band a ground state with an *s*-shaped envelope function, which is only spin degenerate, can be expected. The *p* shell consists of two states and the *d* shell of three. Due to the different parities of the bulk conduction and valence bands, the electron and hole states have a finite optical matrix element if their envelope functions have *the same* parity, i.e. the allowed transition channels are *s*-*s*, *p*-*p*, *s*-*d*, etc. Each transition channel exists twice, once for the *A*-type holes and once for the *B*-type holes. Figure 7.5 shows the calculated single-particle electron and hole energy levels of all QDs considered in this chapter including the six energetically lowest (highest) electron (hole) states. The electron states are all formed predominantly by the conduction band (≈ 95 %). Therefore, the *s*, *p*, and *d* shells can be clearly distinguished. The hole spectra, however, are more complex, because holes states are not exclusively formed by either the *A or*

B band, but by a mixture of both bands and even a small C-band contribution. Still, each hole state can be characterized by the band that contributes the most to it (see labels in Fig. 7.5). For QDs with an aspect ratio of 1:5 [Fig. 7.5(a)] the A-band s-state ($h_0 \equiv h_A$; $\approx 95\,\%$ A-band projection) and the B-band s-state ($h_1 \equiv h_B$; $\approx 90\,\%$ B-band projection) are energetically well separated from the excited hole states. Both have an unambiguously s-shaped envelope function (not shown here). The splitting between both states ($\approx 9-10\,\mathrm{meV}$) does not increase for smaller QDs, but is constant. It corresponds to the energy separation between A and B band in strained GaN. The higher excited hole states can not be unambiguously assigned to p- or d-like orbitals. Please note, that although they have been labeled according to the major band contributions, this contribution sometimes does not exceed 50 %. The QDs with aspect ratio 1:10 [Fig. 7.5(b)] exhibit a significantly smaller excited-states splitting for electrons and holes due to the weaker lateral confinement. An exception is the splitting between h_A and h_B, which is largely independent from the QD dimensions as discussed before. For both aspect ratios the hole spectrum is much denser than the electron spectrum (mind the different scales used in Fig. 7.5).

7.4.1 Optical Transitions

In bulk GaN an anisotropy of the strain field in the basal plane changes the character of the band-edge states from A (B) type to P_x (P_y), if the stress is larger along y (cf Sec. 5.2). The optical matrix elements involving the confined A- or B-band hole states in the QDs respond differently to an asymmetry of the confinement potential in the basal plane: They become linearly polarized in orthogonal directions. Figure 7.6(a) shows the oscillator strengths between the six lowest electron levels e_i and the twelve highest hole levels h_j (up to an energy difference $e_i - h_j$ of 3.75 eV) for the QD with $h{:}d = 1{:}5$ and $h = 2.0\,\mathrm{nm}$. Figure 7.6(b) shows the respective spectrum for a similar QD with an in-plane elongation of 10 % along $[11\bar{2}0]$. Almost all transitions of the elongated dot show a pronounced linear polarization either parallel to the elongation or perpendicular to it. The transition between the electron ground state e_0 and h_A (h_B) is linearly polarized along (perpendicular to) the long axis of the QD. Both transitions together can be regarded as s-channel. The wave functions of the higher excited hole states are build of sizeable contributions from more than one valence band. Therefore, these states cannot be unambiguously assigned to p- or d-like symmetry. The p- and d-shell labels in Fig. 7.6 are given according to the main contribution. Figure 7.7 shows the corresponding spectrum for a 10 %-elongated QD with aspect ratio $h{:}d = 1{:}10$. The QDs with aspect ratio $h{:}d = 1{:}10$ show the same polarization as those with 1:5 albeit less pronounced. The strain anisotropy that is induced by the elongation affects the confined states less in QDs with larger diameter, because the main parts of the wave functions

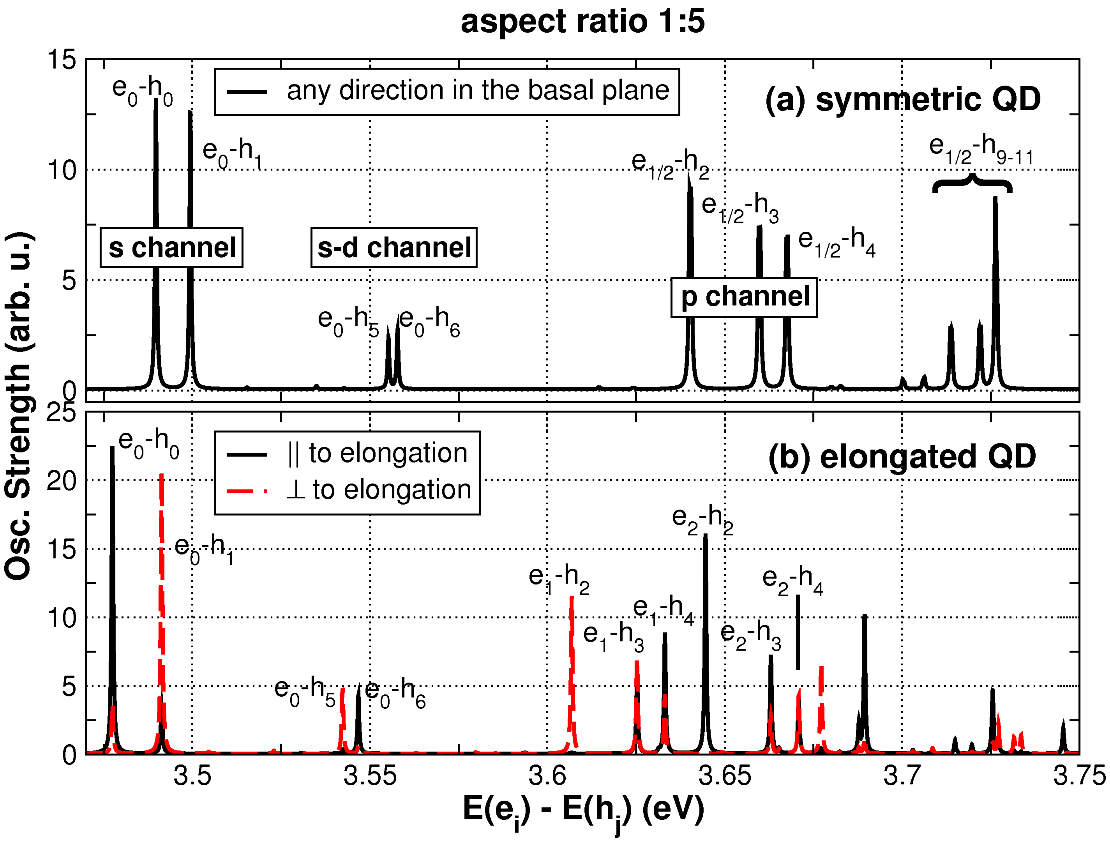

Figure 7.6: Oscillator strength between the single-particle electron and hole state for a GaN/AlN QD with an aspect ratio of $h{:}d = 1:5$ and a height of $h = 2.0\,\mathrm{nm}$. Shown are all transitions involving one of the first six electron levels (e_i) and one of the first twelve hole levels (h_j), but only up to an energy difference $e_i - h_j$ of 3.75 eV. (a) For a symmetric QD. (b) For a QD with a 10 % in-plane elongation along [11$\bar{2}$0].

are located in the center of the dot.

The spectral density increases significantly due to weaker quantization effects in dots with aspect ratio 110. The smaller level spacing of the single-particle electron and hole spectrum translates into a very dense optical excitation spectrum. The energetic separation between the orthogonally polarized (e_0,h_A) and (e_0,h_B) transitions in the *s*-channel, however, is independent of the size of the QDs or their vertical aspect ratio. For (in-plane) symmetric QDs it is about 10 meV and increases for anisotropic QDs. This large separation between the orthogonally polarized lines should enable a spectral separation of both lines even at elevated temperatures. Thus, the well-defined polarization of the ground-state transition can be exploited for polarization control in future single-photon sources.

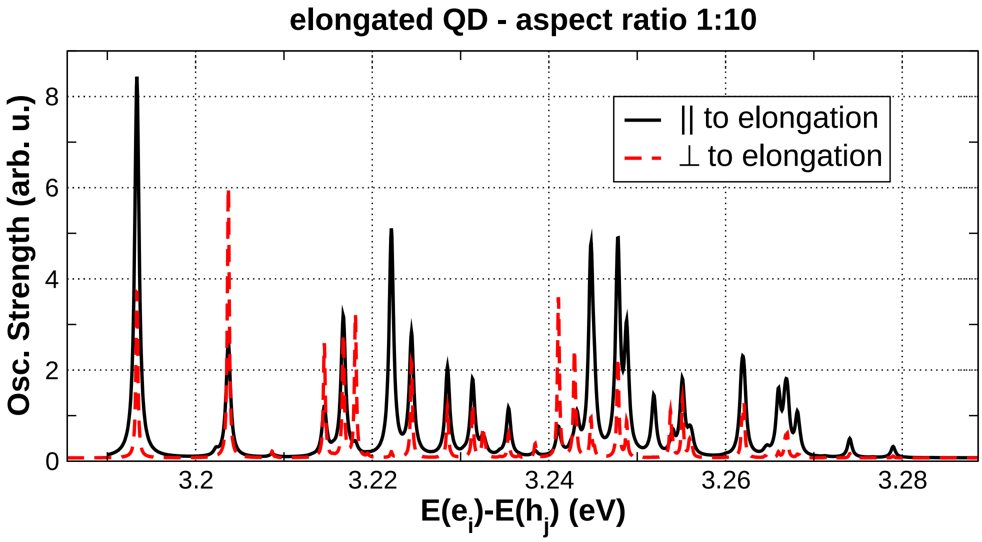

Figure 7.7: Oscillator strength between the single-particle electron and hole state for a GaN/AlN QD with an aspect ratio of $h{:}d = 1{:}10$, a height of $h = 2.0\,\mathrm{nm}$, and a 10 % in-plane elongation of the QD. Shown are all transitions involving one of the first six electron levels (e_i) and one of the first twelve hole levels (h_j).

7.4.2 Control of the Polarization by Uniaxial Stress

The linear polarization of the transitions is a result of the strain anisotropy. Therefore, it can be induced directly by uniaxial stress, without any structural anisotropy of the dot. The effect of uniaxial stress on the polarization of the ground-state transition of the QD with aspect ratio 1:10 and height 2 nm is shown in Fig. 7.8 (black line and circles). A pronounced polarization is found at stress levels that can easily be induced by anisotropic strain relaxation in epitaxial heterostructures (due to the formation of cracks or defects)[39] or by externally applied stress. The study of samples with cracks or or defects has, of course, only academic value, because no opto-electronic devices could be based on such structures. The application of external uniaxial stress, on the other hand, could be exploited to study the polarization mechanism presented here in detail experimentally, because the strain anisotropy inside the QDs could be varied in-situ. For future device application the effect could also be exploited to control or, at least, fine-tune the polarization of the emitted photons. Figure 7.8 also shows calculations where uniaxial stress has been applied to elongated QDs (blue lines and diamonds; red lines and squares). The polarization induced by the structure can be easily enhanced or even inverted by the external stress. Thus, to achieve polarized emission, the structural elongation of the QDs within the sample may varied as long as the strain field is controlled. On the other hand it is also possible to compensate the anisotropy in elongated QDs, if unpolarized emission is desired.

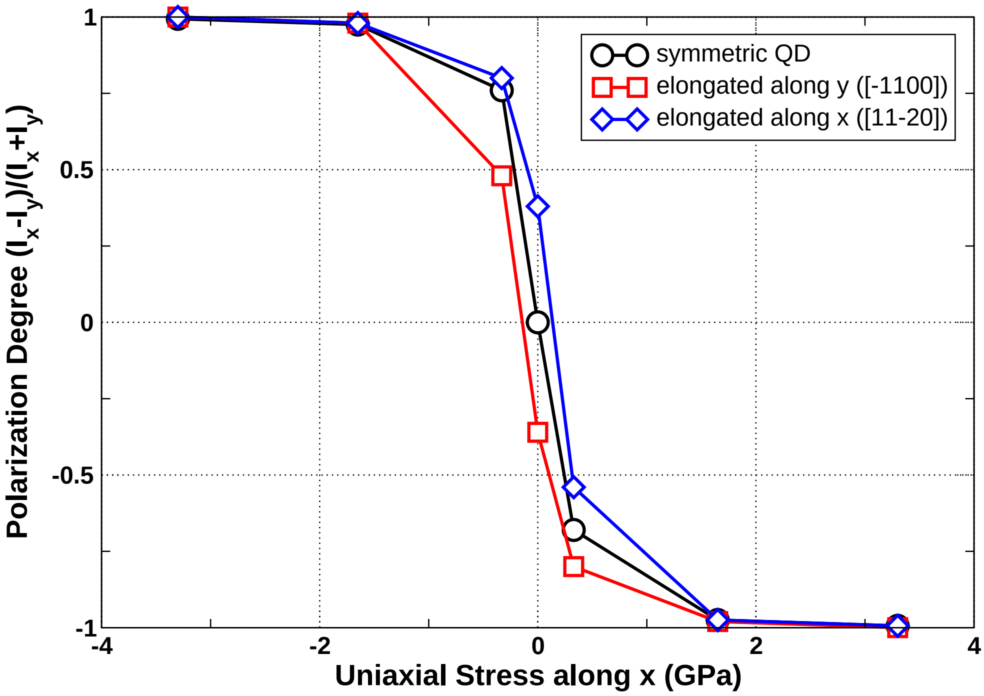

Figure 7.8: Polarization degree of the excitonic ground-state transition as a function of uniaxial stress along x ($[11\bar{2}0]$), relaxation of the sample in y and z direction according to the laws of continuum mechanics has been included. The calculations have been performed for three different QDs with an aspect ratio of $h{:}d = 1{:}10$ and a height of $h = 2.0\,\mathrm{nm}$. *Black lines and circles:* Symmetrical GaN/AlN QD. *Blue lines and diamonds:* GaN/AlN QDs with 10 % elongation along x. *Red line and squares:* GaN/AlN QDs with 10 % elongation along y.

7.5 Summary

In this chapter the spectroscopic properties of c-plane GaN/AlN QDs have been investigated. The excitonic transition energies and radiative lifetimes are largely determined by the height of the QDs. The calculated relation between transition energy and radiative lifetime agrees well with recent experimental observations. Biexciton (XX) and both trions (X^+ and X^-) are anti-binding (blue-shifted with respect to the exciton) for all model QDs considered here. In contrast to the absolute transition energies, the few-particle binding energies depend heavily on the QDs' aspect ratio.

Similar to $\mathrm{In_xGa_{1\text{-}x}N}$/GaN QDs, a linear polarization of the interband transitions in c-plane GaN/AlN QDs can be induced by an asymmetric strain field within in the basal plane. Transitions involving either A- or B-type hole states are polarized in orthogonal directions. The separation of the A-type ground state and the orthogonally polarized B-type first excited state is $\approx 10\,\mathrm{meV}$ and largely independent from the QD size and shape. A sufficient strain anisotropy can be induced by, e.g., structural elongation of the QDs or by externally applied uniaxial stress. Moreover, a polarization resulting from structural elongation can be compensated by external stress.

8 Conclusion

In this work the electronic and optical properties of wurtzite $In_xGa_{1-x}N$/GaN and GaN/AlN quantum dots (QDs) have been investigated theoretically by means of eight-band $\mathbf{k}\cdot\mathbf{p}$ theory. Experimental observations obtained in (time-resolved) photoluminescence (PL) and cathodoluminescence spectroscopy on $In_xGa_{1-x}N$/GaN QDs could be understood based on the theoretical results. For the optical properties of GaN/AlN QDs predictions were made that can, in the future, be exploited for the fabrication of QD-based sources of single polarized photons. In detail:

(i) A consistent set of $\mathbf{k}\cdot\mathbf{p}$ parameters for the wurtzite and zinc-blende phases of GaN, AlN, and InN has been derived from accurate first-principle band-structure calculations within the G_0W_0 approximation. It has been demonstrated that the obtained band parameters are in very good agreement with available experimental data, proving the reliability of the method. Moreover, reliable values have been provided for parameters that have not yet been determined experimentally, such as, e.g., the band parameters of the zinc-blende phases of GaN, AlN, and InN or the E_p and valence-band parameters of wurtzite phases. These parameters are essential for understanding the physics of these materials.

(ii) The general features of the electronic structure of wurtzite group-III-nitride based QDs have been discussed using a typical $In_xGa_{1-x}N$/GaN QD as an example. A large impact of the built-in piezoelectric and pyroelectric fields on the electronic properties of the QDs has been observed: The electrostatic fields cause a spatial separation of electron and hole wave functions and a redshift of the transition energies of hundreds of meV by the quantum-confined Stark effect. Due to the valence-band structure of wurtzite group-III nitrides and the specific strain situation in QDs, the confined hole states are formed predominantly by the two highest valence bands (*A*- and *B* band),in contrast to typical InAs/GaAs QDs, where the hole ground state and the first few excited hole states are formed predominantly by the heavy-hole band alone. Particularly, the hole ground state is formed by the *A* band, and the first excited state by the *B* band.

(iii) A pronounced dependence of the excitonic transition energies and radiative lifetimes on the structural properties of the $In_xGa_{1-x}N$/GaN QDs, i.e., their chemical composition, height, and lateral extension has been observed. The experimentally observed broad ensemble photoluminescence peak could be explained by variations of the size, shape, and indium concentration of the QDs in the ensemble. The photon-energy-dependent decay-time distribution function has been extracted from the experimentally observed multi-exponential decay of the ensemble PL. The distribution function agrees well with recently publish single-QD decay times. The radiative lifetimes of localized excitons in $In_xGa_{1-x}N$/GaN QDs have been calculated and it has been shown that the built-in piezo- and pyroelectric fields within the QDs are the origin of the broad lifetime distribution: They cause a sensitive dependence of the radiative lifetimes on the QD geometry and composition. The lifetimes are also very sensitive to the chemical composition of the material in the surrounding of the QDs. Therefore, a broad distribution of excitonic lifetimes and, consequently, a multi-exponential decay of the ensemble PL is generally expected in this material system in the case of unscreened fields. The decay-time distribution extracted from the experimental PL decay is reproduced qualitatively by the calculated radiative lifetimes.

(iv) Emission spectra from single $In_xGa_{1-x}N$/GaN QDs with up to five lines per QD have been observed in CL spectroscopy. The lines are linearly polarized in orthogonal directions. These observations have been investigated theoretically. The large number of emission lines has been explained with emission from different excitonic complexes, such as, e.g., excitons, biexcitons, and charged excitonic complexes; their polarization could be traced back to an anisotropy of the confinement potential, e.g., a slight elongation of the QDs in the basal plane. The *A*- and *B*- type hole states change their character under asymmetric strain in the basal plane.The optical transitions involving these hole states become linearly polarized either parallel (for *A*-type hole states) or perpendicular (for *B*-type hole states) to the axis of weakest compression. Such a mechanism can potentially be exploited for the generation of polarization-based photonic qubits, because the orthogonally polarized lines are spectrally well separated even at elevated temperatures.

(v) The spectroscopic properties of *c*-plane GaN/AlN QDs have been investigated theoretically as a function of their structural properties. The excitonic transition energies and radiative lifetimes are largely determined by the height of the QDs. The calculated relation between transition energies and radiative lifetimes agrees well with recent experimental observations. Biexciton (XX) and both trions (X^+ and X^-) are anti-binding (blue-shifted with respect to the exciton) for all model QDs considered here. Their binding energies depend heavily on the QDs' aspect ratio. For all transition energies, the binding energy of the biexciton, for instance, is more than twice as large for QDs with an aspect ratio of 1:5 than in QDs with an aspect ratio of 1:10. This makes the few-particle binding energies an excellent fingerprint of the QDs' aspect ratio.

(vi) The polarization properties of interband transitions in *c*-plane GaN/AlN QDs have been studied. Similar to $In_xGa_{1-x}N$/GaN QDs, a linear polarization of the transitions can be induced by an asymmetric strain field within the QDs. Transitions involving either *A*- or *B*-type hole states are polarized in orthogonal directions. The separation of the *A*-type ground state and the orthogonally polarized *B*-type first excited state is $\approx 10\,\text{meV}$ and largely independent from the QD size and shape. The strain anisotropy can be induced either by a structural elongation of the QDs or by an externally applied uniaxial stress. An in-plane elongation of the QDs of only 10 % leads to a polarization degree of the excitonic ground-state transition of up to 6:1 depending on the other structural parameters of the QDs. An externally applied uniaxial stress of about 300 MPa leads to a polarization degree of more than 5:1 for non-elongated QDs; larger stress results in a complete polarization of the emission. Moreover, a polarization resulting from structural elongation of the QDs can be compensated by external stress. This effect could be exploited for future devices, in particular to achieve a well-defined polarization in QD-based single-photon emitters.

8.1 Outlook

The experimental research in the field of group-III nitride QDs is developing rapidly and poses numerous open questions that require complementary theoretical investigations. At the same time, the employed theoretical models have to be constantly improved in order to describe new experimental developments accurately. Possible improvements of the model used in this thesis include, for instance, the inclusion of nonlinear elastic effects,[172] nonlinear piezoelectric effects,[173;174] and the back-coupling of the built-in electric fields to mechanical distortions.[175] In the author's view a particularly important point is the improvement of the description of few-particle effects, i.e. the inclusion of the quantum-mechanical exchange and correlation effects. These effects are expected to be important for a correct description of the few-particle binding energies and the fine-structure splitting in spectra of single QDs. In particular for GaN/AlN QDs, both topics are the matter of active experimental investigation presently,[32;33;39] due to their relevance for device applications.

Acknowledgement

This work would not have been possible without the help of many people. The author feels particularly indebted to the following individuals and institutions:

- **Prof. Dr. Dieter Bimberg —** for giving me the opportunity to work in his research group and to prepare this thesis. Moreover, for his support and interest in my work.
- **Priv.-Doz. Dr. Axel Hoffmann —** for everything.
- **Prof. Dr. Peter Kratzer, Prof. Dr. Matthias Scheffler,** and **the Fritz-Haber-Institut Berlin —** for their continuous support and all the stuff I learned at FHI.
- **Dr. Andrei Schliwa —** for lots of help and discussions regarding $\mathbf{k}\cdot\mathbf{p}$ simulations and the physics of self-assembled quantum dots and for critical reading of this thesis.
- **Dr. Robert Seguin** and **Dr. Sven Rodt —** for the cathodoluminescence measurements, for critical reading of this thesis, and for numerous fruitful discussions.
- **Dr. Matthias Dworzak** and **Dr. Til P. Bartel —** for the (micro-) photoluminescence measurements.
- **Dr. Patrick Rinke** and **Prof. Dr. Abdallah Qteish —** for the G_0W_0 calculations.
- **Dr. Mahboubeh Hortamani** and **Dr. Thomas Hammerschmidt —** for a very nice and productive atmosphere in our office at FHI.
- **The members of AG Bimberg** and **AG Hoffmann —** for the good atmosphere, support, and everything else.

Appendix A:

Material Parameters for the K·p Calculations

All material parameters used in this work are listed in Tab. A.1. Most of them are based on the recommendations of Vurgaftman and Meyer.[61] $m_{\mathrm{e}}^{\mathrm{i}}$, A_{i}, and $E_{\mathrm{P}}^{\mathrm{i}}$ are derived from G_0W_0 calculations (Sec. 4.1). For InN the fundamental band gap from the G_0W_0 calculations has been used and for GaN and AlN the experimental band gaps recommended by Vurgaftman and Meyer. The crystal-field splittings are known to be sensitive to lattice deformations, such as changes in the c_0/a_0 ratio or the internal lattice parameter u.[180–182] These parameters are, however, uncertain input parameters for the G_0W_0 calculations. Therefore, the crystal-field splitting energies from Vurgaftman and Meyer are used rather than the G_0W_0 values. For the VB offsets between InN, GaN, and AlN the values calculated by Wei and Zunger[180] are used. The anisotropy of the static dielectric constants ε_{r} is neglected and the mean value is used instead for all directions. For the refractive indices of GaN and AlN the Sellmeier-formula derived by Antoine-Vincent *et al.*[183] is applied:

$$n = \sqrt{a + \frac{b\lambda^2}{\lambda^2 - c^2}} \quad ,$$

with $a = 5.15$, $b = 0.35$, and $c = 339.8\,\mathrm{nm}$ for GaN and $a = 1.00$, $b = 3.12$, and $c = 138.0\,\mathrm{nm}$ for AlN. λ is the wavelength of the emitted light, which is determined by the transition energy of the respective QD and transition.

For alloys linearly interpolated parameters have been used, except for the parameters listed in Tab. A.2 where the given bowing parameters have been used for parabolic interpolation. The

Table A.1: Material parameters for InN, GaN, and AlN. If not indicated differently parameters are taken from Ref. 61.

Parameter	GaN	InN	AlN
a_{lc} (nm)	0.3189	0.3545	0.3112
c_{lc} (nm)	0.5185	0.5703	0.4982
C_{11} (GPa)	390	223	396
C_{12} (GPa)	145	115	137
C_{13} (GPa)	106	92	108
C_{33} (GPa)	398	224	373
C_{44} (GPa)	105 48	116	
e_{15} (C/m^2)	0.326	0.264	0.418
e_{31} (C/m^2)	-0.527	-0.484	-0.536
e_{33} (C/m^2)	0.895	1.06	1.56
P_{SP} (C/m^2)	-0.034	-0.042	-0.090
ε_{r}	9.8[176]	13.8[177]	9.1[178]
E_{G} (eV)	3.510	0.69[179]	6.25
Δ_{CR} (eV)	0.010	0.040	-0.169
Δ_{SO} (eV)	0.017	0.005	0.019
$m_e^{\parallel}/m_0$[179]	0.065	0.186	0.322
$m_e^{\perp}/m_0$[179]	0.068	0.209	0.329
$E_{\mathrm{P}}^{\parallel}$ (eV)[179]	17.292	8.742	16.972
$E_{\mathrm{P}}^{\perp}$ (eV)[179]	16.265	8.809	18.165
A_1[179]	-5.947	-15.803	-3.991
A_2[179]	-0.528	-0.497	-0.311
A_3[179]	5.414	15.251	3.671
A_4[179]	-2.512	-7.151	-1.147
A_5[179]	-2.510	7.060	-1.329
A_6[179]	-3.202	-10.078	-1.952
E_{V} (eV)[180]	0.8	1.3	0.0
a_1 (eV)	-4.9	-3.5	-3.4
a_2 (eV)	-11.3	-3.5	-11.8
D_1 (eV)	-3.7	-3.7	-17.1
D_2 (eV)	4.5	4.5	7.9
D_3 (eV)	8.2	8.2	8.8
D_4 (eV)	-4.1	-4.1	-3.9
D_5 (eV)	-4.0	-4.0	-3.4
D_6 (eV)	-5.5	-5.5	-3.4

Table A.2: Non-zero bowing parameters for the group-III nitride alloys. Parameters are taken from Ref. 61.

Parameter	GaInN	AlGaN	AlInN
E_G (eV)	1.4	0.7	2.5
P_{SP} ($\frac{\mathrm{C}}{\mathrm{m}^2}$)	-0.037	-0.021	-0.070

bowing parameter *b* for a parameter *E* and alloy $\mathrm{A_xB_{1\text{-}x}N}$ is defined by the equation

$$E_{\mathrm{A_xB_{1\text{-}x}C}} = xE_{\mathrm{AC}} + (1-x)\,E_{\mathrm{BC}} - x\,(1-x)\,b \quad .$$

Appendix B:
K·p Method for Zinc-blende Crystals

In the following only the parts of the Hamiltonian that are needed for determining the zinc-blende parameters in Sec. 4.1, i.e., the pure **k**·**p** Hamiltonian without its strain-dependence or the calculation of piezoelectric potentials in zinc-blende crystals will be described. The respective equations can be found elsewhere.[71;184]

The **k**·**p**-Hamiltonian for zinc-blende crystals can be derived from the one for wurtzite crystals using the following modifications:

- the matrix G_1 simplifies through $P_1 = P_2$ $(E_{\mathrm{P1}} = E_{\mathrm{P2}})$ and $\Delta_{\mathrm{CR}} = 0$.
- The parameters A'_{i}, L'_{i}, M'_{i}, and N'_{i} in G_2 are given by

$$\begin{aligned}
\left(A'_1 = A'_2 =\right) A' &= \frac{\hbar^2}{2}\left(\frac{1}{m_{\mathrm{e}}} - \frac{1}{m_0}\right) - \frac{P^2}{E_{\mathrm{g}}} \quad , \\
\left(L'_1 = L'_2 =\right) L' &= -\frac{\hbar^2}{2m_0}\left(\gamma_1 + 4\gamma_2\right) + \frac{P^2}{E_{\mathrm{g}}} \quad , \\
\left(M_1 = M_2 = M_3 =\right) M &= -\frac{\hbar^2}{2m_0}\left(\gamma_1 - 2\gamma_2\right) \quad , \\
\left(N'_1 = N'_2 =\right) N' &= -\frac{\hbar^2}{2m_0} 6\gamma_3 + \frac{P^2}{E_{\mathrm{g}}} \quad , \\
N'_3 &= 0 \quad , \qquad \text{(B.1)}
\end{aligned}$$

where m_{e} denotes the electron effective mass and γ_{i} the Luttinger parameters.

Appendix C:
Effective Masses and Luttinger(-like) Parameters

The equations connecting the effective hole masses to the Luttinger(-like) parameters are in detail —for wurtzite crystals—:^{73}

$$\begin{aligned}
m_0/m_{\mathrm{A}}^{\parallel} &= -(A_1+A_3) \quad , \\
m_0/m_{\mathrm{A}}^{\perp} &= -(A_2+A_4) \quad , \\
m_0/m_{\mathrm{B}}^{\parallel} &= -\left[A_1+\left(\frac{E_{\mathrm{B}}}{E_{\mathrm{B}}-E_{\mathrm{C}}}\right)A_3\right] \quad , \\
m_0/m_{\mathrm{B}}^{\perp} &= -\left[A_2+\left(\frac{E_{\mathrm{B}}}{E_{\mathrm{B}}-E_{\mathrm{C}}}\right)A_4\right] \quad , \\
m_0/m_{\mathrm{C}}^{\parallel} &= -\left[A_1+\left(\frac{E_{\mathrm{C}}}{E_{\mathrm{C}}-E_{\mathrm{B}}}\right)A_3\right] \quad , \\
m_0/m_{\mathrm{C}}^{\perp} &= -\left[A_2+\left(\frac{E_{\mathrm{C}}}{E_{\mathrm{C}}-E_{\mathrm{B}}}\right)A_4\right] \quad ,
\end{aligned}$$

with

$$\begin{aligned}
E_{\mathrm{B}} &= \frac{\Delta_{\mathrm{CR}}-\Delta_{\mathrm{SO}}/3}{2} \\
&\quad +\sqrt{\left(\frac{\Delta_{\mathrm{CR}}-\Delta_{\mathrm{SO}}/3}{2}\right)^2+2\left(\frac{\Delta_{\mathrm{SO}}/3}{2}\right)^2} \quad , \\
E_{\mathrm{C}} &= \frac{\Delta_{\mathrm{CR}}-\Delta_{\mathrm{SO}}/3}{2}
\end{aligned}$$

$$-\sqrt{\left(\frac{\Delta_{\mathrm{CR}}-\Delta_{\mathrm{SO}}/3}{2}\right)^2+2\left(\frac{\Delta_{\mathrm{SO}}/3}{2}\right)^2} \quad .$$

For AlN the indices A, B, and C have to be interchanged: A → B, B → C, C → A.
—for zinc blende crystals—:[87]

$$\begin{aligned}
m_0/m_{\mathrm{hh}}^{[001]} &= \gamma_1-2\gamma_2 \quad ,\\
m_0/m_{\mathrm{hh}}^{[110]} &= \frac{1}{2}(2\gamma_1-\gamma_2-3\gamma_3) \quad ,\\
m_0/m_{\mathrm{hh}}^{[111]} &= \gamma_1-2\gamma_3 \quad ,\\
m_0/m_{\mathrm{lh}}^{[001]} &= \gamma_1+2\gamma_2 \quad ,\\
m_0/m_{\mathrm{lh}}^{[110]} &= \frac{1}{2}(2\gamma_1+\gamma_2+3\gamma_3) \quad ,\\
m_0/m_{\mathrm{lh}}^{[111]} &= \gamma_1+2\gamma_3 \quad ,\\
m_0/m_{\mathrm{so}} &= \gamma_1-\frac{E_{\mathrm{P}}\Delta_{\mathrm{SO}}}{3E_{\mathrm{g}}(E_{\mathrm{g}}+\Delta_{\mathrm{SO}})} \quad .
\end{aligned}$$

Abbreviations

CB	conduction band
CI	configuration interaction
CL	cathodoluminescence
DALI	digital analysis of lattice images
DFT	density-functional theory
FWHM	full width at half maximum
LD	laser diode
LDA	local-density approximation
LED	light-emitting diode
MOCVD	metal-organic chemical vapor deposition
OEPx	optimized effective potential
PL	photoluminescence
QCSE	quantum-confined Stark effect
QD	quantum dot
QW	quantum well
TRPL	time-resolved photoluminescence
VB	valence band
X-TEM	cross-sectional transmission electron microscopy
X	exciton
XX	biexciton
$X^{+/-}$	positive/negative trion

Bibliography

[1] S. Nakamura, T. Mukai, and M. Senoh, Jpn. J. Appl. Phys. **30**, L1998 (1991).

[2] S. Nakamura, Science **281**, 956 (1998).

[3] S. Nakamura, M. Senoh, S. Nagahama, N. Iwasa, T. Yamada, T. Matsushita, Y. Sugimoto, and H. Kiyoku, Appl. Phys. Lett. **69**, 4056 (1996).

[4] S. Nakamura, M. Senoh, S. Nagahama, N. Iwasa, T. Yamada, T. Matsushita, H. Kiyoku, and Y. Sugimoto, Jpn. J. Appl. Phys. **35**, L74 (1996).

[5] F. Hide, P. Kozodoy, S. P. DenBaars, and A. J. Heeger, Appl. Phys. Lett. **70**, 2664 (1997).

[6] C. Zhang and A. J. Heeger, J. Appl. Phys. **84**, 1579 (1998).

[7] Y. Sato, N. Takahashi, and S. Sato, Jpn. J. Appl. Phys. **35**, L838 (1996).

[8] Y. Taniyasu, M. Kasu, and T. Makimoto, Nature **441**, 325 (2006).

[9] V. Adivarahan, W. H. Sun, A. Chitnis, M. Shatalov, S. Wu, H. P. Maruska, and M. A. Khan, Appl. Phys. Lett. **85**, 2175 (2004).

[10] S. Chichibu, T. Azuhata, T. Sota, and S. Nakamura, Appl. Phys. Lett. **69**, 4188 (1996).

[11] S. Chichibu, T. Azuhata, T. Sota, and S. Nakamura, Appl. Phys. Lett. **70**, 2822 (1997).

[12] S. Chichibu, K. Wada, and S. Nakamura, Appl. Phys. Lett. **71**, 2346 (1997).

[13] K. P. O'Donnell, R. W. Martin, and P. G. Middleton, Phys. Rev. Lett. **82**, 237 (1999).

[14] Y. Arakawa and H. Sakaki, Appl. Phys. Lett. **40**, 939 (1982).

[15] M. Asada, Y. Miyamoto, and Y. Suematsu, IEEE J. Quant. Electron. **22**, 1915 (1986).

[16] N. Kirstaedter, N. N. Ledentsov, M. Grundmann, D. Bimberg, V. M. Ustinov, S. S. Ruvimov, M. V. Maximov, P. S. Kop’ev, Z. I. Alferov, U. Richter, P. Werner, U. Gosele, and J. Heydenreich, Electron. Lett. **30**, 1416 (1994).

[17] I. K. Park, M. K. Kwon, S. B. Seo, J. Y. Kim, J. H. Lim, and S. J. Park, Appl. Phys. Lett. **90**, 111116 (2007).

[18] A. Lochmann, E. Stock, O. Schulz, F. Hopfer, D. Bimberg, V. A. Haisler, A. I. Toropov, A. K. Bakarov, and A. K. Kalagin, Electron. Lett. **42**, 774 (2006).

[19] M. Scholz, S. Buettner, O. Benson, A. I. Toropov, A. K. Bakarov, A. K. Kalagin, A. Lochmann, E. Stock, O. Schulz, F. Hopfer, V. A. Haisler, and D. Bimberg, Optics Express **15**, 9107 (2007).

[20] R. Seguin, A. Schliwa, S. Rodt, K. Potschke, U. W. Pohl, and D. Bimberg, Phys. Rev. Lett. **95**, 257402 (2005).

[21] S. Kako, C. Santori, K. Hoshino, S. Götzinger, Y. Yamamoto, and Y. Arakawa, Nature Materials **5**, 887 (2006).

[22] O. Moriwaki, T. Someya, K. Tachibana, S. Ishida, and Y. Arakawa, Appl. Phys. Lett. **76**, 2361 (2000).

[23] R. A. Oliver, G. A. D. Briggs, M. J. Kappers, C. J. Humphreys, S. Yasin, J. H. Rice, J. D. Smith, and R. A. Taylor, Appl. Phys. Lett. **83**, 755 (2003).

[24] R. Seguin, S. Rodt, A. Strittmatter, L. Reißmann, T. Bartel, A. Hoffmann, D. Bimberg, E. Hahn, and D. Gerthsen, Appl. Phys. Lett. **84**, 4023 (2004).

[25] T. Bartel, M. Dworzak, M. Strassburg, A. Hoffmann, A. Strittmatter, and D. Bimberg, Appl. Phys. Lett. **85**, 1946 (2004).

[26] H. Schömig, S. Halm, A. Forchel, G. Bacher, J. Off, and F. Scholz, Phys. Rev. Lett. **92**, 106802 (2004).

[27] J. H. Rice, J. W. Robinson, J. H. Na, K. H. Lee, R. A. Taylor, D. P. Williams, E. P. O’Reilly, A. D. Andreev, Y. Arakawa, and S. Yasin, Nanotechnology **16**, 1477 (2005).

[28] K. Sebald, H. Lohmeyer, J. Gutowski, T. Yamaguchi, and D. Hommel, Phys. Stat. Sol. (b) **243**, 1661 (2006).

[29] M. Winkelnkemper, R. Seguin, S. Rodt, A. Schliwa, L. Reissmann, A. Strittmatter, A. Hoffmann, and D. Bimberg, J. Appl. Phys. **101**, 113708 (2007).

[30] S. Kako, K. Hoshino, S. Iwamoto, S. Ishida, and Y. Arakawa, Appl. Phys. Lett. **85**, 64 (2004).

[31] R. Bardoux, T. Guillet, P. Lefebvre, T. Taliercio, T. Bretagnon, S. Rousset, B. Gil, and F. Semond, Phys. Rev. B **74**, 195319 (2006).

[32] R. Bardoux, T. Guillet, B. Gil, P. Lefebvre, T. Bretagnon, T. Taliercio, S. Rousset, and F. Semond, Phys. Rev. B **77**, 235315 (2008).

[33] D. Simeonov, A. Dussaigne, R. Butte, and N. Grandjean, Phys. Rev. B **77**, 075306 (2008).

[34] F. Rol, S. Founta, H. Mariette, B. Daudin, L. S. Dang, J. Bleuse, D. Peyrade, J. M. Gerard, and B. Gayral, Phys. Rev. B **75**, 125306 (2007).

[35] J. Simon, N. T. Pelekanos, C. Adelmann, E. Martinez-Guerrero, R. Andre, B. . Daudin, L. S. Dang, and H. Mariette, Phys. Rev. B **68**, 035312 (2003).

[36] D. Lagarde, A. Balocchi, H. Carrère, P. Renucci, T. Amand, and X. Marie, Phys. Rev. B **77**, 041304R (2008).

[37] S. Ruffenach, O. Briot, M. Moret, and B. Gil, Appl. Phys. Lett. **90**, 153102 (2007).

[38] M. Winkelnkemper, R. Seguin, S. Rodt, A. Schliwa, L. Reissmann, A. Strittmatter, A. Hoffmann, and D. Bimberg, Physica E **40**, 2217 (2008).

[39] O. Moshe, D. H. Rich, B. Damilano, and J. Massies, Phys. Rev. B **77**, 155322 (2008).

[40] D. Bimberg, M. Grundmann, and N. N. Ledentsov, *Quantum Dot Heterostructures* (Wiley, Weinheim, 1999).

[41] D. Bimberg, ed., *Semiconductor Nanostructures* (Springer, Berlin, 2008).

[42] Also known as metal-organic vapor-phase epitaxy.

[43] V. A. Shchukin, N. N. Ledentsov, and D. Bimberg, *Epitaxy of Nanostructures* (Springer, Berlin, 2004).

[44] T. P. Bartel, P. Specht, J. C. Ho, and C. Kisielowski, Phil. Mag. **87**, 1983 (2007).

[45] Dilute nitrides have significantly different properties and will not be considered within this thesis.

[46] B. Damilano, N. Grandjean, S. Dalmasso, and J. Massies, Appl. Phys. Lett. **75**, 3751 (1999).

[47] T. Bretagnon, S. Kalliakos, P. Lefebvre, P. Valvin, B. Gil, N. Grandjean, A. Dussaigne, B. Damilano, and J. Massies, Phys. Rev. B **68**, 205301 (2003).

[48] T. Bretagnon, P. Lefebvre, P. Valvin, R. Bardoux, T. Guillet, T. Taliercio, B. Gil, N. Grandjean, F. Semond, B. Damilano, A. Dussaigne, and J. Massies, Phys. Rev. B **73**, 113304 (2006).

[49] In the sense that the two strain components in the plane perpendicular to the polar axis (in the notation of this work $\varepsilon_{\mathrm{xx}}$ and $\varepsilon_{\mathrm{yy}}$) in sum do not equal twice the strain component parallel to the polar axis ($\varepsilon_{\mathrm{zz}}$): $\varepsilon_{\mathrm{xx}}+\varepsilon_{\mathrm{yy}}-2\varepsilon_{\mathrm{zz}}\neq 0$.

[50] F. Bernardini, V. Fiorentini, and D. Vanderbilt, Phys. Rev. B **56**, 10024 (1997).

[51] $E=\frac{\rho}{\varepsilon_0\varepsilon_{\mathrm{r}}}$; $U=Ed$. Here, E is the strength of the electric fields, $\varepsilon_0\varepsilon_{\mathrm{r}}$ the dielectric constant of the medium in the capacitor, U the potential drop within the capacitor, and d the height of the capacitor, i.e. the distance between both charge planes.

[52] D. A. B. Miller, D. S. Chemla, T. C. Damen, A. C. Gossard, W. Wiegmann, T. H. Wood, and C. A. Burrus, Phys. Rev. Lett. **53**, 2173 (1984).

[53] S. Kalliakos, T. Bretagnon, P. Lefebvre, T. Taliercio, B. Gil, N. Grandjean, B. Damilano, A. Dussaigne, and J. Massies, J. Appl. Phys. **96**, 180 (2004).

[54] G. Bastard and J. A. Brum, IEEE J. Quant. Electron. **22**, 1625 (1986).

[55] O. Stier, M. Grundmann, and D. Bimberg, Phys. Rev. B **59**, 5688 (1999).

[56] A. Rastelli, S. Stufler, A. Schliwa, R. Songmuang, C. Manzano, G. Costantini, K. Kern, A. Zrenner, D. Bimberg, and O. G. Schmidt, Phys. Rev. Lett. **92**, 166104 (2004).

[57] M. Hayne, J. Maes, S. Bersier, V. V. Moshchalkov, A. Schliwa, L. Muller-Kirsch, C. Kapteyn, R. Heitz, and D. Bimberg, Appl. Phys. Lett. **82**, 4355 (2003).

[58] A. D. Andreev and E. P. O'Reilly, Phys. Rev. B **62**, 15851 (2000).

[59] V. A. Fonoberov and A. A. Balandin, J. Appl. Phys. **94**, 7178 (2003).

[60] M. Winkelnkemper, A. Schliwa, and D. Bimberg, Phys. Rev. B **74**, 155322 (2006).

[61] I. Vurgaftman and J. R. Meyer, Appl. Phys. Rev. **94**, 3675 (2003).

[62] Http://www.nextnano.de/.

[63] J. C. Slater and G. F. Koster, Phys. Rev. **94**, 1498 (1954).

[64] T. Saito and Y. Arakawa, Physica E **15**, 169 (2002).

[65] V. Ranjan, G. Allan, C. Priester, and C. Delerue, Phys. Rev. B **68**, 115305 (2003).

[66] N. Baer, S. Schulz, S. Schumacher, P. Gartner, G. Czycholl, and F. Jahnke, Appl. Phys. Lett. **87**, 231114 (2005).

[67] N. Baer, S. Schulz, P. Gartner, S. Schumacher, G. Czycholl, and F. Jahnke, Phys. Rev. B **76**, 075310 (2007).

[68] S. F. Borg, *Matrix-Tensor Methods in Continuum Mechanics* (Van Nostrand, Princeton, NJ, 1963).

[69] M. Suzuki and T. Uenoyama, in *Group-III-Nitride Semiconductor Compounds*, edited by B. Gil (Clarendon, Oxford, 1998), chap. 8, p. 307.

[70] F. Bernardini, V. Fiorentini, and D. Vanderbilt, Phys. Rev. Lett. **79**, 3958 (1997).

[71] D. Gershoni, C. H. Henry, and G. A. Baraff, IEEE J. Quant. Electron. **29**, 2433 (1993).

[72] G. L. Bir and G. E. Pikus, *Symmetry and Strain-Induced Effects in Semiconductors* (Halsted, New York, 1974).

[73] S. L. Chuang and C. S. Chang, Phys. Rev. B **54**, 2491 (1996).

[74] D. J. Dugdale, S. Brand, and R. A. Abram, Phys. Rev. B **61**, 12933 (2000).

[75] R. McWeeny, *Methods of Molecular Quantum Mechanics* (Academic, London, 1969).

[76] M. Brasken, M. Lindberg, D. Sundholm, and J. Olsen, Phys. Rev. B **61**, 7652 (2000).

[77] O. Stier, A. Schliwa, R. Heitz, M. Grundmann, and D. Bimberg, Phys. Stat. Sol. (b) **224**, 115 (2001).

[78] A. J. Williamson, A. Franceschetti, and A. Zunger, Europhys. Lett. **53**, 59 (2001).

[79] J. Shumway, A. Franceschetti, and A. Zunger, Phys. Rev. B **63**, 155316 (2001).

[80] A. Schliwa, M. Winkelnkemper, and D. Bimberg (2008), submitted to Phys. Rev. B.

[81] J. C. Slater, *Self-Consistent Field for Molecules and Solids: Quantum Theory of Molecules and Solids, Vol. 4, The* (McGraw-Hill, New York, 1974).

[82] D. L. Dexter, *Theory of the Optical Properties of Imperfections in Nonmetals* (Academic, New York, 1958), vol. 6 of *Solid State Physics*, chap. 0, p. 353.

[83] S. Schulz, S. Schumacher, and G. Czycholl, Phys. Rev. B **73**, 245327 (2006).

[84] L. W. Wang and A. Zunger, J. Chem. Phys. **100**, 2394 (1994).

[85] W. Walukiewicz, J. W. Ager, III, K. M. Yu, Z. Lilienthal-Weber, J. Wu, S. X. Li, R. E. Jones, and J. D. Denlinger, J. Phys. D: Appl. Phys. **39**, R83 (2006).

[86] See Ref. 61 and references therein.

[87] I. Vurgaftman and J. R. Meyer, Appl. Phys. Rev. **89**, 5815 (2001).

[88] V. Y. Davydov, A. A. Klochikhin, R. P. Seisyan, V. V. Emtsev, S. V. Ivanov, F. Bechstedt, J. Furthmüller, H. Harima, A. V. Mudryi, J. Aderhold, O. Semchinova, and J. Graul, Phys. Stat. Sol. (b) **229**, R1 (2002).

[89] J. Wu, W. Walukiewicz, K. M. Yu, J. W. Ager, III, E. E. Haller, H. Lu, W. Schaff, Y. Saiton, and Y. Nanishi, Appl. Phys. Lett. **80**, 3967 (2002).

[90] Y. Nanishi, Y. Saito, and T. Yamaguchi, Jpn. J. Appl. Phys. **42**, 2549 (2003).

[91] A. Sher, M. Van Schilfgaarde, M. A. Berding, S. Krishnamurthy, and A.-B. Chen, MRS Internet J. Nitride Semicond. Res. **4**, G5.1 (1999).

[92] F. Bechstedt and J. Furthmüller, J. Cryst. Growth **246**, 315 (2002).

[93] J. G. Lozano, F. M. Morales, R. Garcia, D. González, V. Lebedev, C. Y. Wang, V. Cimalla, and O. Ambacher, Appl. Phys. Lett. **90**, 091901 (2007).

[94] P. Rinke, A. Qteish, J. Neugebauer, C. Freysoldt, and M. Scheffler, New J. Phys. **7**, 126 (2005).

[95] P. Rinke, M. Scheffler, A. Qteish, M. Winkelnkemper, D. Bimberg, and J. Neugebauer, Appl. Phys. Lett. **89**, 161919 (2006).

[96] P. Rinke, M. Winkelnkemper, A. Qteish, D. Bimberg, J. Neugebauer, and M. Scheffler, Phys. Rev. B **77**, 075202 (2008).

[97] W. M. Yim, E. J. Stofko, P. J. Zanzucchi, J. I. Pankove, M. Ettenberg, and S. L. Gilbert, J. Appl. Phys. **44**, 292 (1972).

[98] L. Chen, B. J. Skromme, R. F. Dalmau, R. Schlesser, Z. Sitar, C. Chen, W. Sun, J. Yang, M. A. Khan, M. L. Nakarmi, J. Y. Lin, and H. X. Jiang, Appl. Phys. Lett. **85**, 4334 (2004).

[99] P. B. Perry and R. F. Rutz, Appl. Phys. Lett. **33**, 319 (1978).

[100] Q. Guo and A. Yoshida, Jpn. J. Appl. Phys. **33**, 2453 (1994).

[101] H. Akamaru, A. Onodera, T. Endo, and O. Mishima, J. Phys. Chem. Solids **63**, 887 (2002).

[102] J. Chen, W. Z. Shen, H. Ogawa, and Q. X. Guo, Appl. Phys. Lett. **84**, 4866 (2004).

[103] J. Li, K. B. Nam, M. L. Nakarmi, J. Y. Lin, H. X. Jiang, P. Carrier, and S. H. Wei, Appl. Phys. Lett. **83**, 5163 (2003).

[104] J. Bhattacharyya, S. Ghosh, M. R. Gokhale, B. M. Arora, H. Lu, and W. J. Schaff, Appl. Phys. Lett. **89**, 151910 (2006).

[105] M. Higashiwaki and T. Matsui, J. Cryst. Growth **251**, 494 (2003).

[106] M. Losurdo, G. Bruno, T. H. Kim, S. Choi, and A. Brown, Appl. Phys. Lett. **88**, 121928 (2006).

[107] R. Goldhahn, P. Schley, A. T. Winzer, M. Rakel, C. Cobet, N. Esser, H. Lu, and W. J. Schaff, J. Cryst. Growth **288**, 273 (2006).

[108] M. P. Thompson, G. W. Auner, T. S. Zheleva, K. A. Jones, S. J. Simko, and J. N. Hilfiker, J. Appl. Phys. **89**, 3331 (2001).

[109] Z. Sitar, M. J. Paisley, J. Ruan, J. W. Choyke, and R. F. Davis, J. Mater. Sci. Lett. **11**, 261 (1992).

[110] H. Okumura, S. Yoshida, and T. Okahisa, Appl. Phys. Lett. **64**, 2997 (1994).

[111] G. Ramirez-Flores, H. Navarro-Contreras, A. Lastras-Martínez, R. C. Powell, and J. E. Greene, Phys. Rev. B **50**, 8433 (1994).

[112] J. Schörmann, D. J. As, K. Lischka, P. Schley, R. Goldhahn, S. F. Li, W. Löffler, M. Hetterich, and H. Kalt, Appl. Phys. Lett. **89**, 261903 (2006).

[113] Throughout this work $\Delta_{\mathrm{CR}} > 0$ refers to the Γ_9-Γ_7-Γ_7 VB odering and $\Delta_{\mathrm{CR}} < 0$ to Γ_7-Γ_9-Γ_7.

[114] For the plots the effective electron masses and γ_{i} (A_{i}) parameters recommended in Ref. 61 and the band gaps (and crystal field splitting energies) from our OEPx(cLDA)+G_0W_0calculations have been used.

[115] E. Silveira, J. A. Freitas, Jr., M. Kneissl, D. W. Treat, N. M. Johnson, G. A. Slack, and L. J. Schowalter, Appl. Phys. Lett. **84**, 3501 (2004).

[116] A. V. Rodina and B. K. Meyer, Phys. Rev. B **64**, 245209 (2001).

[117] S. Shokhovets, G. Gobsch, and O. Ambacher, Appl. Phys. Lett. **86**, 161908 (2005).

[118] A. V. Rodina, M. Dietrich, A. Göldner, L. Eckey, A. Hoffmann, A. L. Efros, M. Rosen, and B. K. Meyer, Phys. Rev. B **64**, 115204 (2001).

[119] Calculated using $\Delta_{\mathrm{SO}} = 0.019\,\mathrm{eV}$ and $\Delta_{\mathrm{CR}} = 0.010\,\mathrm{eV}$ (Ref. 118).

[120] J. Wu, W. Walukiewicz, K. M. Yu, J. W. Ager, III, E. E. Haller, H. Lu, W. J. Schaff, Y. Saito, and Y. Nanishi, Appl. Phys. Lett. **80**, 3967 (2002).

[121] S. P. Fu and Y. F. Chen, Appl. Phys. Lett. **85**, 1523 (2004).

[122] A. T. Hofmann, T. Chavdarov, V. Darakchieva, H. Lu, W. J. Schaff, and M. Schubert, Phys. Stat. Sol. (c) **3**, 1854 (2006).

[123] T. Inushima, M. Higashiwaki, and T. Matsui, Phys. Rev. B **68**, 235204 (2003).

[124] M. Suzuki, T. Uenoyama, and A. Yanase, Phys. Rev. B **52**, 8132 (1995).

[125] D. Fritsch, H. Schmidt, and M. Grundmann, Phys. Rev. B **67**, 235205 (2003).

[126] G. B. Ren, Y. M. Liu, and P. Blood, Appl. Phys. Lett. **74**, 1117 (1999).

[127] S. K. Pugh, D. J. Dugdale, S. Brand, and R. A. Abram, Semicond. Sci. and Technol. **14**, 23 (1999).

[128] P. Perlin, E. Litwin-Staszewska, B. Suchanek, W. Knap, J. Camassel, T. Suski, R. Piotrzkowski, I. Grzegory, S. Porowski, E. Kaminska, and J. C. Chervin, Appl. Phys. Lett. **68**, 1114 (1996).

[129] A. Kasic, M. Schubert, S. Einfeldt, D. Hommel, and T. E. Tiwald, Phys. Rev. B **62**, 7365 (2000).

[130] B. K. Meyer, D. Volm, A. Graber, H. C. Alt, T. Detchprohm, A. Amano, and I. Akasaki, Solid State Comm. **95**, 597 (1995).

[131] K. Kim, W. R. L. Lambrecht, B. Segall, and M. Van Schilfgaarde, Phys. Rev. B **56**, 7363 (1997).

[132] A. Strittmatter, A. Krost, J. Bläsing, and D. Bimberg, Phys. Stat. Sol. (a) **176**, 611 (1999).

[133] A. Rosenauer and D. Gerthsen, Adv. Img. Elec. Phys. **107**, 121 (1999).

[134] D. Gerthsen, E. Hahn, B. Neubauer, V. Potin, A. Rosenauer, and M. Schowalter, Phys. Stat. Sol. (c) **0**, 1668 (2003).

[135] A. Strittmatter, L. Reißmann, R. Seguin, S. Rodt, A. Brostowski, U. W. Pohl, D. Bimberg, E. Hahn, and D. Gerthsen, J. Cryst. Growth **272**, 415 (2004).

[136] P. Lefebvre, T. Taliercio, A. Morel, J. Allegre, M. Gallart, B. Gil, H. Mathieu, B. Damilano, N. Grandjean, and J. Massies, Appl. Phys. Lett. **78**, 1538 (2001).

[137] I. L. Krestnikov, N. N. Ledentsov, A. Hoffmann, D. Bimberg, A. V. Sakharov, W. V. Lundin, A. F. Tsatsulnikov, A. S. Usikov, Z. I. Alferov, Y. G. Musikhin, and D. Gerthsen, Phys. Rev. B **66**, 155310 (2002).

[138] J. W. Robinson, J. H. Rice, A. Jarjour, J. D. Smith, R. A. Taylor, R. A. Oliver, G. A. D. Briggs, M. J. Kappers, C. J. Humphreys, and Y. Arakawa, Appl. Phys. Lett. **83**, 2674 (2003).

[139] A. Bell, J. Christen, F. Bertram, F. A. Ponce, H. Marui, and S. Tanaka, Appl. Phys. Lett. **84**, 58 (2004).

[140] A. Morel, P. Lefebvre, T. Taliercio, T. Bretagnon, B. Gil, N. Grandjean, B. Damilano, and J. Massies, Physica E **17**, 64 (2003).

[141] A. Reale, G. Massari, A. D. Carlo, P. Lugli, A. Vinattieri, D. Alderighi, M. Colocci, F. Semond, N. Grandjean, and J. Massies, J. Appl. Phys. **93**, 400 (2003).

[142] H. Gotoh, T. Tawara, Y. Kobayashi, N. Kobayashi, and T. Saitoh, Appl. Phys. Lett. **83**, 4791 (2003).

[143] R. Kohlrausch, Pogg. Ann Phys. Chem. **91**, 179 (1854).

[144] In the present work the numerical Laplace transformation package available at http://www.wolframresearch.com has been used.

[145] A similar approach has been applied by Van Driel *et al.* on the TRPL of CdSe QDs.[185].

[146] M. Senes, K. L. Smith, T. M. Smeeton, S. E. Hooper, and J. Heffernan, Phys. Rev. B **75**, 045314 (2007).

[147] G. A. Narvaez, G. Bester, and A. Zunger, Phys. Rev. B **72**, 245318 (2005).

[148] C. H. Bennet and G. Brassard, IEEE International Conference on Computers, Systems and Signal Proceessing Bangalore, India **1**, 175179 (1984).

[149] S. Adachi, S. Muto, K. Hazu, T. Sota, K. Suzuki, S. F. Chichibu, and T. Mukai, Phys. Rev. B **67**, 205212 (2003).

[150] D. Bimberg, H. Münzel, A. Steckenborn, and J. Christen, Phys. Rev. B **31**, 7788 (1985).

[151] V. Türck, S. Rodt, O. Stier, R. Heitz, R. Engelhardt, U. W. Pohl, D. Bimberg, and R. Steingrüber, Phys. Rev. B **61**, 9944 (2000).

[152] S. Rodt, A. Schliwa, K. Potschke, F. Guffarth, and D. Bimberg, Phys. Rev. B **71**, 155325 (2005).

[153] D. Gammon, E. S. Snow, B. V. Shanabrook, D. S. Katzer, and D. Park, Phys. Rev. Lett. **76**, 3005 (1996).

[154] M. Bayer, G. Ortner, O. Stern, A. Kuther, A. A. Gorbunov, A. Forchel, P. Hawrylak, S. Fafard, K. Hinzer, T. L. Reinecke, S. N. Walck, J. P. Reithmaier, F. Klopf, and F. Schäfer, Phys. Rev. B **65**, 195315 (2002).

[155] M. Sugisaki, H. Ren, S. V. Nair, K. Nishi, S. Sugou, T. Okuno, and Y. Masumoto, Phys. Rev. B **59**, R5300 (1999).

[156] V. D. Kulakovskii, G. Bacher, R. Weigand, T. Kümmell, A. Forchel, E. Borovitskaya, K. Leonardi, and D. Hommel, Phys. Rev. Lett. **82**, 1780 (1999).

[157] I. A. Akimov, K. V. Kavokin, A. Hundt, and F. Henneberger, Phys. Rev. B **71**, 075326 (2005).

[158] R. Seguin, S. Rodt, A. Schliwa, K. Pötschke, U. W. Pohl, and D. Bimberg, Phys. Stat. Sol. (b) **243**, 3937 (2006).

[159] C. Santori, S. Götzinger, Y. Yamamoto, S. Kako, K. Hoshino, and Y. Arakawa, Appl. Phys. Lett. **87**, 051916 (2005).

[160] T. Nakaoka, S. Kako, and Y. Arakawa, Phys. Rev. B **73**, 121305 (2006).

[161] B. Daudin, F. Widmann, G. Feuillet, Y. Samson, M. Arlery, and J. L. Rouviere, Phys. Rev. B **56**, R7069 (1997).

[162] F. Widmann, B. Daudin, G. Feuillet, Y. Samson, J. L. Rouviere, and N. Pelekanos, J. Appl. Phys. **83**, 7618 (1998).

[163] F. Widmann, J. Simon, B. Daudin, G. Feuillet, J. L. Rouviere, N. T. Pelekanos, and G. Fishman, Phys. Rev. B **58**, R15989 (1998).

[164] M. Miyamura, K. Tachibana, and Y. Arakawa, Appl. Phys. Lett. **80**, 3937 (2002).

[165] K. Hoshino, S. Kako, and Y. Arakawa, Appl. Phys. Lett. **85**, 1262 (2004).

[166] D. Simeonov, E. Feltin, J. F. Carlin, R. Butte, M. Ilegems, and N. Grandjean, J. Appl. Phys. **99**, 083509 (2006).

[167] A. Cros, N. Garro, J. M. Llorens, A. Garcia-Cristobal, A. Cantarero, N. Gogneau, E. Monroy, and B. Daudin, Phys. Rev. B **73**, 115313 (2006).

[168] J. Coraux, B. Amstatt, J. A. Budagoski, E. Bellet-Amalric, J. L. Rouviere, V. Favre-Nicolin, M. G. Proietti, H. Renevier, and B. Daudin, Phys. Rev. B **74**, 195302 (2006).

[169] J. Coraux, V. Favre-Nicolin, H. Renevier, M. G. Proietti, B. Amstatt, E. Bellet-Amalric, and B. Daudin, J. Appl. Phys. **101**, 056106 (2007).

[170] B. Daudin, G. Feuillet, H. Mariette, G. Mula, N. Pelekanos, E. Molva, J. L. Rouviere, C. Adelmann, E. Martinez-Guerrero, J. Barjon, F. Chabuel, B. Bataillou, and J. Simon, Jpn. J. Appl. Phys. **40**, 1892 (2001).

[171] A. D. Andreev and E. P. O'Reilly, Appl. Phys. Lett. **79**, 521 (2001).

[172] S. P. Lepkowski, J. A. Majewski, and G. Jurczak, Phys. Rev. B **72**, 245201 (2005).

[173] F. Bernardini and V. Fiorentini, Phys. Rev. B **64**, 85207 (2001).

[174] V. Fiorentini, F. Bernardini, and O. Ambacher, Appl. Phys. Lett. **80**, 1204 (2002).

[175] S. P. Lepkowski and J. A. Majewski, Phys. Rev. B **74**, 035336 (2006).

[176] Average over references 70;186–189.

[177] Average over references 70;190.

[178] Average over references 70;186.

[179] Derived in Sec. 4.1.

[180] S. H. Wei and A. Zunger, Appl. Phys. Lett. **69**, 2719 (1996).

[181] B. Gil, O. Briot, and R. L. Aulombard, Phys. Rev. B **52**, R17028 (1995).

[182] B. Gil, F. Hamdani, and H. Morkoç, Phys. Rev. B **54**, 7678 (1996).

[183] N. Antoine-Vincent, F. Natali, M. Mihailovic, A. Vasson, J. Leymarie, P. Disseix, D. Byrne, F. Semond, and J. Massies, J. Appl. Phys. **93**, 5222 (2003).

[184] A. Schliwa, M. Winkelnkemper, and D. Bimberg, Phys. Rev. B **76**, 205324 (2007).

[185] A. F. van Driel, I. S. Nikolaev, P. Vergeer, P. Lodahl, D. Vanmaekelbergh, and W. L. Vos, Phys. Rev. B **75**, 035329 (2007).

[186] S. M. Komirenko, K. W. Kim, M. A. Stroscio, and M. Dutta, Phys. Rev. B **59**, 5013 (1999).

[187] A. S. Barker, Jr. and M. Ilegems, Phys. Rev. B **7**, 743 (1973).

[188] T. Azuhata, T. Sota, K. Suzuki, and S. Nakamura, J. Phys.: Cond. Matt. **7**, 1949 (1995).

[189] T. Deguchi, D. Ichiryu, K. Toshikawa, K. Sekiguchi, T. Sota, R. Matsuo, T. Azuhata, M. Yamaguchi, T. Yagi, S. Chichibu, and S. Nakamura, J. Appl. Phys. **86**, 1860 (1999).

[190] V. Y. Davydov, V. V. Emtsev, I. N. Goncharuk, A. N. Smirnov, and V. D. Petrikov, Appl. Phys. Lett. **75**, 3297 (1999).